FÍSICA
REVISTA CUBANA DE FÍSICA
Sociedad Cubana de Física
y Facultad de Física,
Universidad de La Habana
VOL. 42 No. 1
JULIO 15, 2025

CELEBRANDO EL AÑO INTERNACIONAL DE LA CIENCIA Y LA TECNOLOGÍA CUÁNTICAS

Revista Cubana de Física
ISSN 0253-9268
Online ISSN 2224-7939

REVISTA CUBANA DE FÍSICA
Vol. 42, No. 1 (15 de julio de 2025)
ISSN 0253 9268 Online 2224 7939

Portada: Collage que involucra instituciones cubanas conectadas al Año Internacional de la Ciencia y la Tecnología Cuánticas.

TODOS LOS ARTÍCULOS EN FORMATO-e:
www.revistacubanadefisica.org

LA REVISTA CUBANA DE FÍSICA ES UNA PUBLICACIÓN SEMESTRAL DE LA SOCIEDAD CUBANA DE FÍSICA

COORDENADAS

ARTÍCULOS ORIGINALES

COMUNICACIONES ORIGINALES

OUR DUTY IS TO FOSTER QUANTUM PHYSICS IN CUBA

NUESTRO DEBER ES IMPULSAR LA FÍSICA CUÁNTICA EN CUBA

R. Mulet-Genicio

The proclamation of 2025 as the **International Year of Quantum Science and Technology (IYQST)** by the United Nations commemorates a century since the moment in which quantum mechanics revolutionized our understanding of the physical world. This designation recognizes the scientific triumphs of the past from Heisenberg's uncertainty principle to Schrödinger's wave equation, and the technologies quantum science has enabled, such as semiconductors, computers, lasers, MRI imaging, and nuclear energy. Today, we are on the brink of a second quantum revolution with fast progress in quantum computing, sensing, and encryption that may soon transform our societies. This global celebration reminds all of us of the urgent need to harness physics in general and quantum physics in particular for the sustainable development of our country and of humanity. Cuba's journey in quantum physics is a testament to the resilience and ingenuity of our community. Indeed, Cuban physicists have mastered quantum mechanics: It has been one of our most fertile research areas for several decades. With a lot of effort, our community has continued working in the field despite the very limited resources available over the past 30 years. Quantum physics is part of our undergraduate programs and is revisited in several postgraduate courses at the Cuban universities where physics is taught. Theoretical and experimental work in the field, together with the help of international collaborations, is an important part of our doctoral programs. I recommend to the readers the editorial *Año Internacional de la Ciencia y la Tecnologa Cuántica* by C. Rodríguez-Castellanos [1]. The work highlights pivotal periods from the initial introduction of quantum theory to contemporary developments showcasing how Cuba has engaged in this cutting-edge field. As we commemorate the International Year of Quantum Science and Technology, let me reaffirm in the name of the Cuban Physical Society our commitment to continue to foster physics and quantum physics in Cuba. This year serves as a call to action: to strengthen collaborations, invest in young talent, and bridge the gap between fundamental science and applications. Quantum technologies promise solutions to pressing challenges, from energy to healthcare. If Cuba is expected to be *a country of men and women of science*, our science must contribute to these solutions.

[1] C. Rodríguez-Castellanos, *An. Acad. Cienc. Cuba*, **15**, e2911 (2025)

MATHEMATICAL TREATMENT OF THE CANONICAL FINITE STATE MACHINE FOR THE ISING MODEL

TRATAMIENTO MATEMÁTICO DE LA MÁQUINA CANÓNICA DE ESTADO FINITO PARA EL MODELO DE ISING

E. Estevez-Rams[a,b†], E. Rodríguez-Horta[a], R. Lora-Serrano[c]

a) Facultad de Física, Universidad de la Habana, San Lázaro y L. CP 10400. La Habana. Cuba
b) Instituto de Ciencias y Tecnología de Materiales, University of Havana (IMRE); estevez@fisica.uh.cu†
c) Universidade Federal de Uberlandia, AV. Joao Naves de Avila, 2121- Campus Santa Monica, Uberlandia, CEP 38408-144,Brazil
† corresponding author

Recibido 3/10/2024; Aceptado 26/5/2025

The complete framework for the minimal deterministic automata construction of the one-dimensional Ising model is presented. The approach follows the known treatment of the Ising model as a Markov random field, where the local characteristic is usually obtained from the stochastic matrix. The problem is the inverse relation or how to get the stochastic matrix from the local characteristics given via the transfer matrix treatment. The obtained expressions allow for performing complexity-entropy analysis of particular instances of the Ising model. Two examples are discussed: the 1/2-spin nearest neighbour and next nearest neighbours Ising model.

El marco teórico para la máquina mínima determinística del model de Ising en una dimensión es presentado. El tratamiento sigue el conocido modelo de Ising tratado como un campo aleatorio de Markov, donde las características locales son obtenidas de la matriz estocástica. El problema abordado necesita la relación inversa, o como obtener la matriz estocástica de las características locales, dadas a través del tratamiento de la matriz de transferencia. Las expresiones obtenidas permiten realizar el análisis de complejidad-entropía para instancias particulares del modelo de Ising. Dos ejemplos son discutidos: el spín-1/2 de vecinos más cercanos y el modelo de segundos vecinos más cercanos.

Keywords: complexity (complejidad); entropy (entropía); Ising model (Modelo de Ising).

I. INTRODUCTION

Minimal deterministic automata, introduced by Grassberger [1] and further developed by Crutchfield et al. [2, 3], is an approach to discovering and characterizing patterns in an information processing system. Building from information theory concepts, it has found applications in several fields and proved its value in several contexts [4–8]. For a stochastic process considered to be stationary, the minimal deterministic automaton is its optimal minimal description, understood as having the best (most accurate) predictive power while using the least possible resources (minimal forecasting complexity) [1,9]. Causality is taken in a general temporal sense: in a given context, cause-to-effect relations are established between past to future events [10].

The Ising model in one-dimension is the best known in Statistical Physics and has become a common topic in most Statistical Mechanics books (see, for example, [11]). Despite its intensive scrutiny in different settings, under different Hamiltonian and interaction ranges, its analysis, in terms of information theory, as a symbol production system is more or less recent. In fact, until 1998, this approach was not attempted when Feldman et al. undertook the task of casting the Ising model under such language [12–14]. Their work allowed the deduction of closed expressions for the entropy density, forecasting complexity, and effective measure complexity. However, these previous treatments did not consider the Ising model in the general framework of a Markov (Gibbs) random field. While the previous approaches are sufficient when nearest-neighbour interaction is considered, the more general framework is necessary, beyond nearest-neighbour interaction, to determine the general probability measure of the associated Markov process [15]. This is what it aims at in this contribution.

Despite being a well-studied system, working through all the mathematical details involved to solve the inverse problem, obtain the stochastic matrix from the Markov Field, and build the minimal deterministic automata in the most general setting in one dimension is worthwhile. Entropic magnitudes follow, which are usually not treated in the Ising model. In this light, we show the use of the developed framework via two examples.

II. THE TRANSFER MATRIX FORMALISM

The Ising (-Lenz) model is probably the most studied lattice-type model in statistical mechanics and is well covered in several statistical physics books for nearest 1/2 spin neighbour interactions [11]. Let us briefly recap, for completeness and notation purposes, the basic ideas of the transfer matrix formalism (we closely follow Dobson [16]) but in a general setting of a local type interaction Hamiltonian, which is usually not found in texts.

Consider a one-dimensional chain of discrete values of length L:

$$s^L = s_0 s_1 s_2 \dots s_{L-1},$$

where s_i can take values from a finite alphabet Θ of cardinality $\theta(=|\Theta|)$ (there will be θ^L possible sequences s^L). Each s_i is called a spin. The interaction between spins of the sequence has a finite range n such that it can be written as

$$E(s_i, s_{i\pm k}) = \begin{cases} \Lambda(s_i, s_{i\pm k}) & 0 < k \leq n \\ 0 & k > n \end{cases}. \tag{1}$$

The s^L sequence can be partitioned into blocks of length n

$$s^L = [s_0 s_1 \dots s_{n-1}] \dots [s_{(N-1)n} s_{(N-1)n+1} \dots s_{Nn-1}],$$

where it has been taken $L = Nn$. The expression can be relabeled as

$$\begin{aligned} s^L &= [s_0^{(0)} \dots s_{n-1}^{(0)}][s_0^{(1)} \dots s_{n-1}^{(1)}] \dots [s_0^{(N-1)} \dots s_{n-1}^{(N-1)}]. \\ &= \eta_0 \eta_1 \dots \eta_{N-1}, \end{aligned}$$

with

$$\eta_i = s_0^{(i)} s_1^{(i)} \dots s_{n-1}^{(i)}. \tag{2}$$

The set of all possible blocks η_i will be denoted by Υ with cardinality $\upsilon = \theta^n$. Υ will be taken as an ordered set (e.g., lexicographic order) where each η_i a natural number, between 0 and $\upsilon - 1$, will be assigned. In what follows, η_i should be understood not only as the configuration (2) but also as its corresponding order in the set Υ; context will eliminate any ambiguity.

As the interaction has range n, one spin corresponding to the η_i block can only interact with all the spins within η_i (type I interaction), and at least one spin from the adjacent blocks $\eta_{i\pm1}$ (type II interaction).

Assuming the symmetry $\Lambda(s_i, s_j) = \Lambda(s_j, s_i)$, the interaction energy of type I for the η_p block, in the presence of an external field B, will be

$$x_{\eta_p} = -B \sum_{i=0}^{n-1} s_i^{(p)} + \sum_{i=0}^{n-2} \sum_{k=i+1}^{n-1} \Lambda(s_i^{(p)}, s_k^{(p)}), \tag{3}$$

which defines a vector $\langle X|$ of length υ. The contribution of type II will be denoted by $y_{\eta_p \eta_{p+1}}$, and will be given by

$$y_{\eta_p \eta_{p+1}} = \sum_{i=0}^{n-1} \sum_{k=0}^{i} \Lambda(s_i^{(p)}, s_k^{(p+1)}), \tag{4}$$

which defines a $\upsilon \times \upsilon$ matrix. In general $y_{\eta_i \eta_j} \neq y_{\eta_j \eta_i}$ which makes Y non-symmetric. The energy of the whole configuration S^L can then be written as

$$\Lambda(s^L) = x_{\eta_0} + y_{\eta_0 \eta_1} + x_{\eta_1} + y_{\eta_1 \eta_2} + \dots + y_{\eta_{N-2} \eta_{N-1}} + x_{\eta_{N-1}}. \tag{5}$$

The vector $\langle U|$ and the matrix V are then introduced as

$$u_{\eta_i} = \exp(-\frac{1}{2} \beta x_{\eta_i}) \tag{6}$$

$$v_{\eta_i \eta_j} = \exp[-\beta(\frac{1}{2} x_{\eta_i} + y_{\eta_i \eta_j} + \frac{1}{2} x_{\eta_j})]. \tag{7}$$

where $\beta \equiv (k_B T)^{-1}$ is the Boltzmann product. V is known as the transfer matrix.

The partition function follows

$$\begin{aligned} Z_{Nn} &= \sum_{\eta_0=0}^{\upsilon-1} \sum_{\eta_1=0}^{\upsilon-1} \dots \sum_{\eta_{N-1}=0}^{\upsilon-1} \exp[-\beta \Lambda(s^L)] \\ &= \langle U | V^{N-1} | U \rangle, \end{aligned} \tag{8}$$

for free boundary conditions. For periodic boundary conditions

$$Z_{Nn} = Tr(V^N). \tag{9}$$

$Tr(M)$ denotes the trace of the matrix M.

As the trace of a matrix is invariant to similarity transformations, from equation (9), for close boundary conditions,

$$Z_{Nn} = \sum \lambda_i^N. \tag{10}$$

λ_i are the eigenvalues of the matrix V. If λ_i is degenerate, then the term is added as many times as its multiplicity. If the eigenvalues are labeled in non increasing order ($|\lambda_i| \geq |\lambda_j| \rightarrow j \geq i$), then for $N \gg 1$

$$Z_{Nn} = \lambda_0^N \tag{11}$$

where λ_0 is the dominant eigenvalue; according to the Perron-Frobenius theorem, it is real, positive, and non-degenerate [15].

For open boundary conditions, again using the Perron-Frobenius theorem for a square positive defined matrix V, the following holds

$$\lim_{N \longrightarrow \infty} \frac{V^N}{\lambda_0^N} = |_r a_0\rangle\langle_l a_0|, \tag{12}$$

where $\langle {}_l a_0|$ and $|{}_r a_0\rangle$ are, respectively, the left and right eigenvectors corresponding to the dominant eigenvalue. The eigenvectors are normalized in the sense of $\langle {}_l a_0 | {}_r a_0 \rangle = 1$. The matrix $|{}_r a_0\rangle\langle {}_l a_0|$ is known as the Perron projection matrix. Using (12) and (8) we arrive at

$$Z_{Nn} = \langle U | {}_r a_0 \rangle \langle {}_l a_0 | U \rangle \lambda_0^{N-1} \tag{13}$$

which, in the particular case of a diagonalizable matrix, reduces to

$$Z_{Nn} = u_0^2 \langle a_0 | a_0 \rangle \lambda_0^{N-1} \tag{14}$$

and u_i are the components of the vector $\langle U|$ in the orthogonal base, defined by the eigenvectors $\langle a_i|$. It is well documented how the thermodynamic magnitudes can be obtained from the partition function [11].

The probability of a given spin chain will be given by

$$\begin{aligned} Pr(s^L) &= \tfrac{1}{Z_{Nn}} e^{-\beta \Lambda(s^L)} \\ &= \tfrac{1}{Z_{Nn}} \left(U_{\eta_0} V_{\eta_0 \eta_1} V_{\eta_1 \eta_2} \dots V_{\eta_{N-2} \eta_{N-1}} U_{\eta_{N-1}} \right) \\ &= \tfrac{U_{\eta_0} U_{\eta_{N-1}}}{M \lambda_0^{N-1}} \prod_{i=0}^{N-2} V_{\eta_i \eta_{i+1}} \end{aligned} \tag{15}$$

valid for free boundary conditions, and $M \equiv \langle U|_r a_0\rangle\langle {}_l a_0|U\rangle$. For periodic boundary conditions

$$Pr(s^L) = \frac{1}{\lambda_0^N}\prod_{i=0}^{N-2} V_{\eta_i\eta_{i+1}} \tag{16}$$

where in both cases, $N \gg 1$.

III. ISING MODEL AS A MARKOV (GIBBS) RANDOM FIELD

The Ising model is a particular case of a Gibbs random field [15], where a Markov random field can be defined

$$Pr(\eta_i = \eta|s^L - \eta_i) = Pr(\eta_i = \eta|\eta_t = b_t \,\text{for}\, t \in \mathcal{N}_i,\ b_t \in \Upsilon). \tag{17}$$

The η_i value is conditioned only in the neighbourhood and not on the entire spin configuration.The probabilities given by (17) are called the local characteristics associated with $\mathcal{P}$.

If $s^L - \eta_i$ is the configuration s^L without considering the block η_i, then the probability $Pr(\eta_i|s^L - \eta_i)$ that the i-block has value η_i when all the other spins (that is, excluding the η_i block) will have the configuration $s^L - \eta_i$ the product rule will given by,

$$Pr(\eta_i|s^L - \eta_i) = \frac{Pr(s^L)}{Pr(s^L - \eta_i)} = \frac{Pr(s^L)}{\sum\limits_{s^{L*}} Pr(s^{L*})} \tag{18}$$

where the sum s^{L*} is over all configurations identical to s^L except, possibly, for the block η_i.

Using equation (15), the probability of a configuration will be

$$\begin{aligned} Pr(s^L) = &\ \tfrac{1}{Z_{Nn}} e^{-\beta\Lambda(s^L)} \\ &= \frac{1}{Z_{Nn}} e^{-\beta x_{\eta_{N-1}}} \prod_{j=1}^{N-2} e^{-\beta x_{\eta_j}} e^{-\beta y_{\eta_j\eta_{j+1}}} \end{aligned} \tag{19}$$

and,

$$Pr(s^L - \eta_i) = \sum_{\eta_k} e^{-\beta y_{\eta_{i-1}\eta_k}} e^{-\beta x_{\eta_k}} e^{-\beta y_{\eta_k\eta_{i+1}}}. \tag{20}$$

The local characteristics equation (18) is then

$$Pr(\eta_i|s^L - \eta_i) = \frac{V_{\eta_{i-1}\eta_i} V_{\eta_i\eta_{i+1}}}{\sum\limits_{\eta_k} V_{\eta_{i-1}\eta_k} V_{\eta_k\eta_{i+1}}} \tag{21}$$

for blocks η_i not at the extremes.

For the first block

$$Pr_0(\eta_0|s^L - \eta_i) = \frac{U_{\eta_0} V_{\eta_0\eta_1}}{\sum\limits_{\eta_k} U_{\eta_k} V_{\eta_k\eta_1}} \tag{22}$$

A similar expression can be found for the last block. Expression (21) has the important consequence that

$$Pr(\eta_i|s^L - \eta_i) = Pr(\eta_i|\eta_{i-1}, \eta_{i+1}) \tag{23}$$

In the associated Markov process, the spin chain is considered a sequential process where blocks η are "emitted" sequentially. In this sense, the probability that, at a given moment, a block η_i is the output of the Markov process is conditioned only on the previously emitted block. In this sense, we can describe a transition probability from one emitted block to the next and associate a probability with it.

Consider the η_i blocks as describing the possible states of an arbitrary block of spins, then Υ is the set of all states. A stochastic matrix P can be defined as

$$P_{ij} = Pr(\eta_j|\eta_i). \tag{24}$$

which describes the transition probability from state η_i to state η_j. By definition $\sum_j P_{ij} = 1$. If $\langle p^\infty|$ is the vector of probabilities over the blocks η_i (the probability that a given block of spins is in a given state), then it is well known that the stationary distribution [15] is given by

$$\langle p^\infty| = \langle w_0| \tag{25}$$

where $\langle w_0|$ is the left dominant eigenvector of the matrix P. The vector $\langle p^\infty|$ allows to calculate $Pr(\eta_i)$ when the Markov process has been running for a sufficiently long time.

The local characteristics can be written in terms of the stochastic matrix P using Bayes theorem

$$\begin{aligned} Pr(\eta_i|\eta_{i-1}, \eta_{i+1}) &= \tfrac{Pr(\eta_i|\eta_{i-1})Pr(\eta_{i+1}|\eta_i\eta_{i-1})}{Pr(\eta_{i+1}|\eta_{i-1})} \\ &= \tfrac{Pr(\eta_i|\eta_{i-1})Pr(\eta_{i+1}|\eta_i)}{\sum\limits_l Pr(\eta_l|\eta_{i-1})Pr(\eta_{i+1}|\eta_l)} \end{aligned} \tag{26}$$

where the Markov character of the field has been used, and the total probability theorem justifies the last step.

Equation (26) can be rewritten as

$$\begin{aligned} &Pr(\eta_i|\eta_{i-1}, \eta_{i+1}) \sum_l Pr(\eta_l|\eta_{i-1}) Pr(\eta_{i+1}|\eta_l) = \\ &Pr(\eta_i|\eta_{i-1}) Pr(\eta_{i+1}|\eta_i) \end{aligned} \tag{27}$$

which forms, when written for each η_i, an homogeneous system of quadratic forms. Such a system can have a non-trivial solution if it is undetermined, which happens if the square of the number of unknowns is larger than the number of equations.

There are $\nu = \theta^n$ possible different blocks η. $Pr(\eta_i|\eta_{i-1}, \eta_{i+1})$ is known from (21). As each local characteristic is determined by three η's, there will be ν^3 equations. $Pr(\eta_i|\eta_k)$ only depends on the actual values of η_i and η_k and not on their position, therefore there will be ν^2 unknowns. The relations

$$\sum_i^\nu Pr(\eta_i|\eta_j) = 1 \qquad \forall j$$

must be added that eliminates ν unknowns. The total number of unknowns is $\nu(\nu-1)$, and the total number of equations ν^3.

$$\nu^3 < \nu^2(\nu-1)^2 \Longrightarrow \nu > 3.6$$

As we seek solutions for integer values of ν, the effective solution will be $\nu \leq 4$. Additional symmetry of the transfer matrix (e.g. $\nu = 2$) can lead to further reduction of the equations, and the system could also have a non-trivial solution for such cases.

Returning to equation (27) and rewriting for any local characteristic

$$Pr(\eta_i|\eta_j,\eta_m)\sum_l Pr(\eta_l|\eta_j)Pr(\eta_m|\eta_l) = \quad (28)$$
$$Pr(\eta_i|\eta_j)Pr(\eta_m|\eta_i),$$

introducing

$$Y_l(j,m) = Pr(\eta_l|\eta_j)Pr(\eta_m|\eta_l) \quad (29)$$

equation (28) can be written as

$$Pr(\eta_i|\eta_j,\eta_m)\sum_l Y_l(j,m) = Y_i(j,m). \quad (30)$$

The normalization condition (which can be derived from equation (26)) over the local characteristics determines

$$\sum_k^v Pr(\eta_k|\eta_j,\eta_m) = 1, \quad (31)$$

Equation (30) is linear and homogeneous over the $Y_i(j,m)$ which, upon solving for the non-trivial-case, leads to a system of simple homogeneous quadratic equations (29) which can be readily solved.

IV. ISING MODEL AS A MINIMAL DETERMINISTIC AUTOMATA

The Markov character of the system means that for the associated Markov process, the generation process can forget all the past except the last block η_{-1} (the last n spins) to determine, as certain as possible, the future. In other words, if the local characteristics imply a stochastic matrix as equation (28) implies, then all past configurations $\overleftarrow{s}^L$ with the same last block η_{-1} condition (statistically) the same future, this fact allows considering the Ising chain as a canonical finite state machine or minimal deterministic automata.

If two blocks η_{-1} and η'_{-1} give the same $Pr(\overrightarrow{s}^L|\overleftarrow{s}^L)$, for all possible futures $\overrightarrow{s}^L$, then η_{-1} y η'_{-1} are said to belong to the same causal state (C_p) and we write

$$\eta_{-1} \sim \eta'_{-1},$$

where $\eta_{-1}, \eta'_{-1} \in C_p$ [10]. Two blocks of the same causal state C_p define identical rows in the stochastic matrix.

The partition of the set Υ in classes of causal states is an equivalence relation.The set of causal states, denoted by C, uniquely determines the future of a sequence.

The probability of a causal state is directly deducible from equation (25),

$$Pr(C_p) = \sum_{\eta_j\in C_p} Pr(\eta_j) = \sum_{\eta_j\in C_p} p^{\infty}_{\eta_j} \quad (32)$$

As each causal state represents the set of past that determines (probabilistically) the same future, the set of causal states represents the memory the system has to keep to predict the future.

The forecasting complexity [1], also known as statistical complexity, has been defined as the Shannon entropy H over the causal states [9][1]

$$\begin{aligned} C_\mu &\equiv -\sum_{C_p\in C} Pr(C_p)\log Pr(C_p) \\ &= H[C]. \end{aligned} \quad (33)$$

The logarithm is usually taken in base two, and the units are then bit. Forecasting complexity measures how much memory (resources) the system needs to predict the future optimally. If the system has $|C|$ causal states, then the forecasting complexity has the upper bound

$$C_\mu \leq \log|C|,$$

corresponding to a uniform distribution of probabilities. The upper bound of the forecasting complexity is also known as topological entropy.

The probability of occurrence of block η_i conditional on the causal state C will be given by

$$\begin{aligned} Pr(\eta_i|C) &= \sum_{\eta_k} Pr(\eta_i|\eta_k\cap C)Pr(\eta_k|C) \\ &= Pr(\eta_i|\eta_j;\eta_j\in C)\sum_{\eta_k\in C} Pr(\eta_k|C) \\ &= Pr(\eta_i|\eta_j;\eta_j\in C) \end{aligned} \quad (34)$$

in the first step, the total probability theorem was used. In the second step, use has been made of the fact that conditioning in $\eta_k\cap C$ is equal to conditioning in η_j if the block belongs to the causal state C and, finally $\sum_{\eta_k\in C} Pr(\eta_k|C) = 1$.

On the other hand

$$\begin{aligned} Pr(\eta_j) &= \sum_{\eta_k} Pr(\eta_j|\eta_k)Pr(\eta_k) \\ &= \sum_{C_k\in C}\sum_{\eta_k\in C_k} Pr(\eta_j|\eta_k)Pr(\eta_k) \\ &= \sum_{C_k\in C} Pr(\eta_j|\eta_{k'},\eta_{k'}\in C_k)Pr(C_k) \end{aligned}$$

making use of equation (34) to get

$$Pr(\eta_j) = \sum_{C_k\in C} Pr(\eta_j|C_k)Pr(C_k). \quad (35)$$

which allows us to compute the occurrence of a block from the probabilities over the causal states.

[1] We prefer to say that it is defined in such a way, rather than state that it follows from its original definition because as pointed out by Grassberger [17], there is no proof that the minimal graph corresponds to the minimal forecasting complexity. However, in the kind of model we are studying, this seems to be the case in general.

The probability of a transition from one causal state to another will be given by

$$Pr(C_k \to C_p) \equiv Pr(C_p|C_k) = \sum_{\eta_j \in C_p} Pr(\eta_j|C_k) \tag{36}$$

We define the transition matrix $T^{(\eta)}$, whose elements are the probability of going from state C_k to state C_p upon emitting a block η:

$$T^{(\eta)}_{rq} = Pr(C_r \overset{\eta}{\to} C_q). \tag{37}$$

By construction, the emission of a block η determines the causal state uniquely to where the transition occurs (this is called the unifiliar property [10]). In this sense, the generation process is deterministic. Correspondingly, the connectivity matrix T is defined as

$$T_{rq} = \sum_{\eta \in \Sigma} T^{(\eta)}_{rq} = Pr(C_r \to C_q) \tag{38}$$

which connects causal states without regard to the emitted block.

To account for the irreducible randomness, the entropy density is defined as [18]

$$\begin{aligned} h &= \lim_{L\to\infty} H[\eta_0|\eta_{-L}\eta_{-L+1}\dots\eta_{-1}] \\ &= \lim_{L\to\infty} H[\eta_0|\overleftarrow{s}^L] \end{aligned} \tag{39}$$

h is the uncertainty on the next emitted block η_0 conditional on having seen infinite previous blocks (spins). By definition, $h \geq 0$.

$$\begin{aligned} H[\eta_0|\overleftarrow{s}^L] &= -\sum_{\eta_0}\sum_{\eta_{-n}}\dots\sum_{\eta_{-1}} Pr(\overleftarrow{s}^L\eta_0)\log Pr(\eta_0|\overleftarrow{s}^L) \\ &= -\sum_{\eta_0}\sum_{\eta_{-N}}\dots\sum_{\eta_{-1}} Pr(\eta_0|\overleftarrow{s}^L)Pr(\overleftarrow{s}^L)\log Pr(\eta_0|\overleftarrow{s}^L) \end{aligned} \tag{40}$$

where $\overleftarrow{s}^L = \eta_{-N}\eta_{-N+1}\dots\eta_{-1}$, , on the other hand, using $\overleftarrow{s}^{L-n} = \eta_{-N}\dots\eta_{-2}$

$$Pr(s^L) = Pr(s^{L-n}|\eta_{-1})Pr(\eta_{-1}). \tag{41}$$

use has been made of Bayes theorem. Substituting equation (41) on equation (40) and reordering terms

$$\begin{aligned} H[\eta_0|\overleftarrow{s}^L] = -\sum_{\eta_0}\Bigg[\sum_{\eta_{-1}} Pr(\eta_0|\eta_{-1})Pr(\eta_{-1})\log Pr(\eta_0|\eta_{-1}) \\ \left\{\sum_{\eta_{-N}}\dots\sum_{\eta_{-2}} Pr(\overleftarrow{s}^{L-n}|\eta_{-1})\right\}\Bigg]. \end{aligned} \tag{42}$$

$$\sum_{\eta_{-N}}\dots\sum_{\eta_{-2}} Pr(\overleftarrow{s}^{L-n}|\eta_{-1})$$

is the probability that from η_{-1} any configuration is conditioned and this probability is 1. Equation (42) then reduces to

$$\begin{aligned} h &= \lim_{L\to\infty} H[\eta_0|\overleftarrow{s}^L] = H[\eta_0|\eta_{-1}] \\ &= -\sum_{C_\alpha \in \mathcal{C}} Pr(C_\alpha)\sum_{\eta_k\in\Sigma} Pr(\eta_k|C_\alpha)\log Pr(\eta_k|C_\alpha) \end{aligned} \tag{43}$$

The mutual information between past and future is called the effective measure complexity [1], also known as excess entropy [18]

$$E \equiv I[\overleftarrow{s} : \overrightarrow{s}], \tag{44}$$

where $I[X : Y]$ is the mutual information between X and Y. From the finite range character of the interaction in the Ising model

$$\begin{aligned} E = I[\overleftarrow{s} : \overrightarrow{s}] &= I[\eta_{-1} : \eta_0] \\ &= H[\eta_{-1}] - H[\eta_0|\eta_{-1}] \end{aligned} \tag{45}$$

where

$$H[\eta_i] = \sum_{\eta_i\in\Sigma} Pr(\eta_i)\log Pr(\eta_i), \tag{46}$$

and

$$H[\eta_0|\eta_{-1}] = H[\eta_0|\overleftarrow{s}^L] = h$$

given by equation (43).

From equation (33) and (43) we arrive to the expression

$$E = C_\mu - h. \tag{47}$$

The effective measure complexity measures the resources the system needs to optimally predict the future once the irreducible randomness has been subtracted [18]. As E is mutual information, it will always be a non-negative value, which implies

$$C_\mu \geq h$$

If the system is perfectly periodic, then $h = 0$ and

$$C_\mu = E.$$

V. EXAMPLES

V.1. 1/2 nearest neighbors spin chain

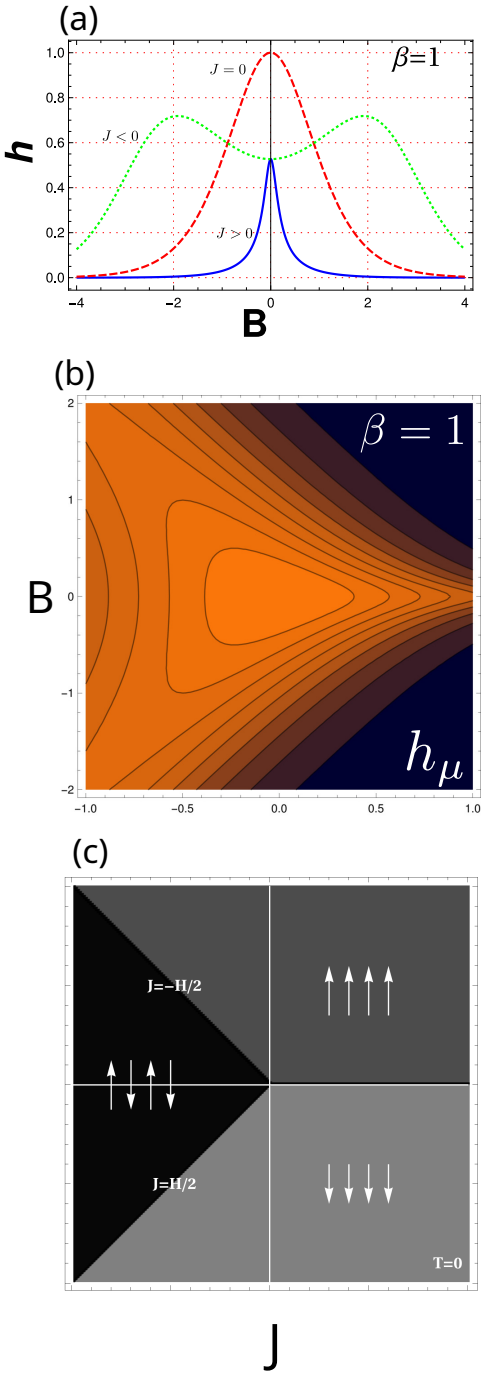

Figure 1. 1/2 nearest neighbors spin chain. (a) The entropy density as a function of the applied field B for ferromagnetic ($J > 0$), antiferromagnetic ($J < 0$), and paramagnetic ($J = 0$) interaction. The Boltzmann factor in all cases is taken as $\beta = 1$. (b) The entropy density h map as a function of the system control parameter J and the applied field B. Black corresponds to $h = 0$, and full orange to $h = 1$. Maximum disorder values happen along the line with no applied field $B = 0$, with the paramagnetic state's maximum at $J = 0$. Boltzmann factor as in (a). (c) The diagram shows the phase diagram for zero absolute temperature as a function of the parameters J and B. Two phases can be identified: ferro- and antiferromagnetic.

The 1/2 nearest neighbour spin chain is defined by the interaction Hamiltonian [20]

$$E = -B\sum_i s_i - J\sum_j s_j s_{j+1}, \tag{48}$$

where B is the external field, and J is the interaction parameter. The η blocks set will be

$$\eta = \downarrow, \uparrow.$$

The local characteristics derived from equation (21) reduce to

$$\begin{aligned}
Pr(\downarrow \mid \downarrow,\downarrow) &= \tfrac{e^{4\beta J}}{e^{2\beta B}+e^{4\beta J}}\\
Pr(\downarrow \mid \downarrow,\uparrow) &= \tfrac{1}{e^{2\beta B}+1}\\
Pr(\uparrow \mid \downarrow,\downarrow) &= \tfrac{1}{e^{4\beta J-2\beta B}+1}\\
Pr(\uparrow \mid \downarrow,\uparrow) &= \tfrac{e^{2\beta B}}{e^{2\beta B}+1}\\
Pr(\downarrow \mid \uparrow,\downarrow) &= \tfrac{1}{e^{2\beta B}+1}\\
Pr(\downarrow \mid \uparrow,\uparrow) &= \tfrac{1}{e^{2\beta(B+2J)}+1}\\
Pr(\uparrow \mid \uparrow,\downarrow) &= \tfrac{e^{2\beta B}}{e^{2\beta B}+1}\\
Pr(\uparrow \mid \uparrow,\uparrow) &= \tfrac{e^{2\beta(B+2J)}}{e^{2\beta(B+2J)}+1}.
\end{aligned} \tag{49}$$

Solving the linear system of equation (30), results in the system of quadratic equations

$$\begin{aligned}
Pr(\downarrow \mid \uparrow)Pr(\uparrow \mid \downarrow) &= e^{2\beta B-4\beta J}Pr(\downarrow \mid \downarrow)\\
Pr(\uparrow \mid \uparrow) &= e^{2B\beta}P(\downarrow \mid \downarrow),
\end{aligned} \tag{50}$$

together with the normalization conditions

$$\begin{aligned}
Pr(\downarrow \mid \uparrow) + Pr(\uparrow \mid \uparrow) &= 1\\
Pr(\downarrow \mid \downarrow) + Pr(\uparrow \mid \downarrow) &= 1
\end{aligned} \tag{51}$$

lead to the solution for[2]

$$Pr(\downarrow \mid \downarrow) = \frac{2e^{2\beta J}}{\sqrt{4e^{2\beta B}+e^{4\beta(B+J)}-2e^{2\beta(B+2J)}+e^{4\beta J}}+e^{2\beta(B+J)}+e^{2\beta J}}. \tag{52}$$

The other entries of the stochastic matrix follow.

[2]This result is equivalent to the one reported as equation (7.31) in [12], but, if one calculates all matrix entries from equation (7.15), the row normalization condition is violated. Therefore, the correctness of the entries in (7.31) in [12] is accidental due to forcing row normalization.

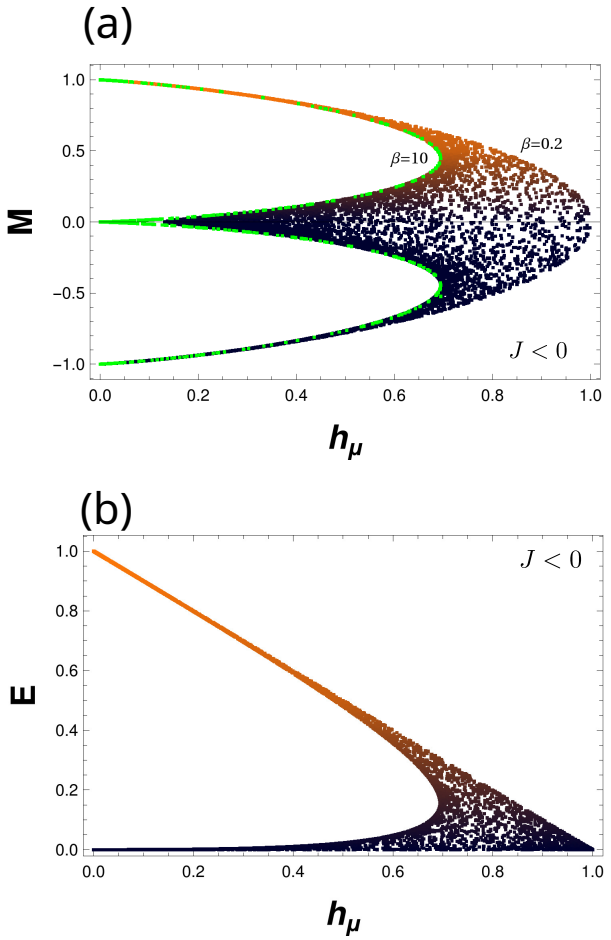

Figure 2. 1/2 nearest neighbors spin chain. (a) The dependence of the magnetization M with the disorder measured by the entropy density B. 10^5 points were used with random parameters in the range $\beta \in [10^{-4}, 10^2]$, $J \in [-1.5, 0]$ and $B \in [-3, 3]$. The green points correspond to $\beta = 10$, while the rust colors are for $\beta = 0.2$, as labeled in the figure. The rust color degradation grows lighter the larger the M value and is used as a visual aid. For all points, the spin coupling is antiferromagnetic. (b) The complexity-entropy diagram for the $1/2$-nearest neighbor Ising model. Simulation conditions follow the same parameter range as in (a). The rust color degradation grows lighter the larger the M value and is used as a visual aid.

The behavior of the entropy density h with the applied field for the three signs of the interaction term is shown in Figure 1a for $\beta = 1$. The results are consistent with the usual graphic of the Boltzmann entropy for this model. The applied field B generally lowers the system's entropy as it tends to align the spins along the field. In the case of the antiferromagnetic coupling, with an increasing value of B, first entropy increases due to random spins, initially contrary to the external field flips, leading to increasing disorder. For the larger field, B, the order starts prevailing as further production of aligned spins overcomes the initial disordering process. For $B = 0$, the system starts with an initial amount of randomness ($h > 0$) for all signs of J as temperature introduces disorder.

In Figure 1(b), the amount of disorder as a function of the applied field B and interaction parameter J. The maximum value of h, for a given value J, is attained at the line $B = 0$ and is the result of $\beta > 0$. The absolute maximum value of h is taken for $B = 0$ and $J = 0$. Increasing the applied field and interaction parameter decreases the spin system's disorder. Compare the entropy map with the phase diagram of the spin system at zero temperature (1(c)). The map of effective measure complexity for $\beta \to \infty$ reproduces the phase diagram (not shown). However, for $\beta < \infty$, the entropy density map merely indicates the mapping of randomness regardless of the underlying pattern, whether ferro- or antiferromagnetic.

The behavior of the magnetization with the disorder as measured through h can be seen in figure 2a. From the stochastic matrix, the two-state minimal deterministic automata were built. The plot was calculated for 10^5 points, randomly taking the parameters' value but keeping $J < 0$. First, we notice that three magnetization values are possible at zero disorder $h = 0$, two at the extremes, corresponding to the spin alignment forced by a sufficiently strong applied field B, and a zero magnetization at $B = 0$. At lower temperatures ($\beta = 10$), for a given disorder value of h, the amount of magnetization that can be accommodated around the vanishing magnetization has fewer values than for larger temperatures $\beta = 0.2$. Also, increasing temperature makes more disorder available for the system, which is seen for the larger possible values of h.

Finally, (h, E) was calculated using the same procedure for the magnetization plot and is shown as a complexity map in figure 2b. This type of complexity map has been discussed before [18]. Small values of the disorder can accommodate a large range of effective measure complexity values, which means varying probability between the two possible causal states. As disorder increases, the system loses structure, tending towards a single-state process that, although increasingly random, is also increasingly less complex.

V.2. 1/2 next nearest neighbors spin chain

If a second coordination is added, the 1/2 next nearest neighbors spin chain, the interaction Hamiltonian [20] now is given by

$$E = -B\sum_i s_i - J_1\sum_j s_j s_{j+1} - J_2\sum_k s_k s_{k+2}. \tag{53}$$

where B is the external field, and J_1, J_2 are spin coupling parameters. The η blocks set will be

$$\eta = \downarrow\downarrow, \downarrow\uparrow, \uparrow\downarrow, \uparrow\uparrow,$$

again, the value 1 corresponds to spin up, whereas -1 corresponds to spin down.

Figure 3 above shows the effective measure complexity as a function of J_1 and J_2 for the ground state ($\beta \to \infty$) at zero field ($B = 0$). While in the nearest neighbor case, only the ferromagnetic and antiferromagnetic case was found in the phase diagram, here, besides those two, a third ordered phase comes into existence, with a periodicity of 4, which can be regarded as a higher coordination anti-ferromagnetic phase. $\uparrow\uparrow\downarrow\downarrow$. This phase results from the larger range of interaction between the spins and competing interactions. For $J_2 \geq 0$, the second range interaction, governed by J_2, favors the ferromagnetic phase, and its balance with the strength and sign of J_1 determines the ferromagnetic or antiferromagnetic

ordering similar to the nearest neighbor coupling. When J_2 becomes negative, it strengthens an antiferromagnetic coupling between second range spin now depending on the sign of J_1, this ordering competes with the first range coupling in two different ways, which will always be at odds with J_2. For certain values of J_1 and J_2, the solution to this balance is the period 4 antiferromagnetic ordering.

When the applied field is different from zero, as shown in the Effective Complexity Measure plot 3 below, as a function of J_1/B and J_2/B, four orderings of periodicity 1, 2, 3, and 4, identified as the ordered sequences:

(1) $\uparrow\uparrow\uparrow\uparrow\uparrow\uparrow\uparrow\uparrow\cdots$

(2) $\uparrow\downarrow\uparrow\downarrow\uparrow\downarrow\uparrow\downarrow\cdots$

(3) $\uparrow\uparrow\downarrow\uparrow\uparrow\downarrow\uparrow\uparrow\cdots$

(4) $\uparrow\uparrow\downarrow\downarrow\uparrow\uparrow\downarrow\downarrow\cdots$

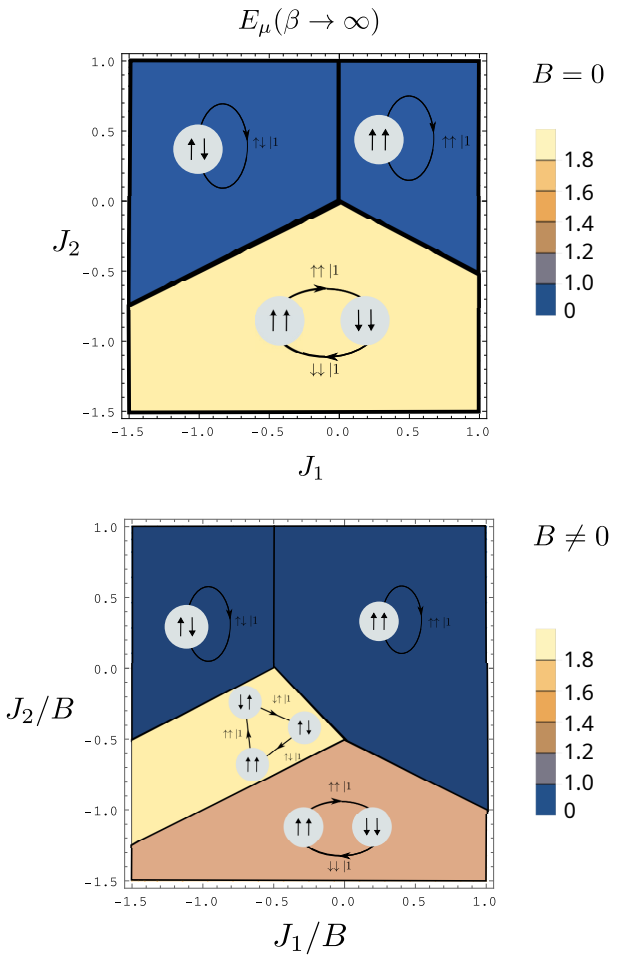

Figure 3. 1/2 next nearest neighbors spin chain. Effective measure complexity (E) at the ground state ($\beta \to \infty$) for zero field ($B = 0$) and non-zero field ($B \neq 0$). Four possible orderings are found $\uparrow\uparrow\uparrow\uparrow\uparrow\uparrow\uparrow\uparrow\cdots$, $\uparrow\downarrow\uparrow\downarrow\uparrow\downarrow\uparrow\downarrow\cdots$, $\uparrow\uparrow\downarrow\uparrow\uparrow\downarrow\uparrow\uparrow\cdots$ and $\uparrow\uparrow\downarrow\downarrow\uparrow\uparrow\downarrow\downarrow\cdots$. The third configuration is only possible at $B \neq 0$.

This has been reported before [20]. The new phase $\uparrow\uparrow\downarrow\uparrow\uparrow\downarrow\uparrow\uparrow\cdots$ appears as a wedge in the phase diagram when B is zero, and it is the result of the new competing factor when the applied field favors one sense in space. The applied field has an effect equivalent to a dipolar average field pointing, in this case, in the up direction, therefore implying a flip of a spin to the upper direction that would otherwise have an antiferromagnetic coupling. This phase, therefore, appears between the simple antiferromagnetic phase and the periodicity 4 antiferromagnetic phase.

VI. CONCLUSION

In this article, we aimed to develop the mathematical treatment of minimal deterministic automata to fully model one-dimensional Ising models, going beyond previous approaches. The deduced expressions can be used to model specific instances of the interaction Hamiltonian. Furthermore, the detailed deduction can be a route map to similar deductions for other common statistical mechanics models, such as Pott or Heisenberg.

VII. ACKNOWLEDGEMENT

FAPEMIG partially financed this work under project BPV-00047-13. EER to thank PVE/CAPES for financial support under grant 1149-14-8. Infrastructure support was given under project FAPEMIG APQ-02256-12.

We want to thank Prof. Crutchfield and coworkers for pointing out that Feldman's treatment still gives the correct quantitative results for the NN model and for further discussions on the subject as a whole.

REFERENCES

[1] P. Grassberger, *Int. J. Theor. Phys.* **25**, 907 (1986).
[2] J. P. Crutchfield, *Knowledge and meaning... chaos and complexity*, in *Modeling complex phenomena*, edited by L. Lam and V. Naroditsky, pp. 66-101, Springer, Berlin (1992).
[3] J. P. Crutchfield, *Nature Physics* **8**, 17 (2012).
[4] D. P. Varn, G. S. Canright, J. P. Crutchfield, *Acta Cryst. A* **A69**, 413 (2013).
[5] V. Ryabov, D. Neroth, *Chaos* **21**, 037113 (2011).
[6] R. Haslinger, K. L. Klinker, C. R. Shalizi, *Neural Computation* **22**, 121 (2010).
[7] E. Rodriguez-Horta, E. Estevez-Rams, R. Neder, R. Lora-Serrano, *Acta. Cryst. A* **A73**, 357 (2017).
[8] E. Rodriguez-Horta, E. Estevez-Rams, R. Lora-Serrano, R. Neder, *Acta. Cryst. A* **A73**, 377 (2017).
[9] J. P. Crutchfield, *Physica D* **75**, 11 (1994).
[10] C. R. Shalizi, J. P. Crutchfield, *J. Stat. Phys.* **104**, 817 (2001).
[11] D. A. Lavis, G. M. Bell, *Statistical Mechanics of Lattice Systems*, Springer, Berlin (1999).
[12] D. P. Feldman, *Computational mechanics of classical spin systems*, Ph.D. Dissertation, Physics Department, University of California, Davis, (September, 1998).
[13] J. P. Crutchfield, D. P. Feldman, *Phys. Rev. E* **55**, R1239(R) (1997).

[14] D. P. Feldman, J. P. Crutchfield, Santa Fe Institute Working Paper 98-04-026 (2008).
[15] E. Behrends, *Introduction to Markov chain*, Springer, Heidelberg (2000).
[16] J. F. Dobson, *J. Math. Phys.* **10**, 40 (1969).
[17] P. Grassberger, arXiv preprint arXiv:1708.03197v3 (2018).
[18] D. P. Feldman, C. S. McTeague, J. P. Crutchfield, *Chaos* **18**, 043106 (2008).
[19] J. Crutchfield, D. P. Feldman, *Chaos* **13**, 25 (2003).
[20] T. Morita, T. Horiguchi, *Phys. Lett.* **A41**, 043106 (1972).

DYNAMIC CAVITY METHOD IN FULLY-ASYMMETRIC MODELS

MÉTODO DE CAVIDAD DINÁMICO EN MODELOS COMPLETAMENTE ASIMÉTRICOS

J. González-García[a†], D. Machado[b, c, d†]

a) Centro de Sistemas Complejos, Facultad de Física, Universidad de La Habana, Cuba; jonathan.gonzalez@estudiantes.fisica.uh.cu†
b) Centro de Sistemas Complejos, Departamento de Física Teórica. Facultad de Física, Universidad de La Habana, Cuba; david.machado@fisica.uh.cu†
c) Dipartimento di Fisica, Sapienza Università di Roma, P.le Aldo Moro 5, 00185 Rome, Italy; david.machado@uniroma1.it†
d) CNR - Nanotec, Unità di Roma, P.le Aldo Moro 5, 00185 Rome, Italy
† corresponding author

Recibido 6/12/2024; Aceptado 30/5/2025

The physics of disordered systems is a broad and constantly evolving field. In this work we focus on the study of discrete variable models with asymmetric interactions, in particular the fully-asymmetric ferromagnet and the fully-asymmetric Sherrington-Kirkpatrick. We use the cavity master equation, a well-known technique for the out-of-equilibrium dynamics, to derive average equations describing the time evolution of the magnetization and the energy in these models. In this way, we recovered previous results for the magnetization known from the literature and obtained new equations for the energy. With this work, we contribute to establish the cavity master equation as one of the most relevant techniques in the study of out-of-equilibrium systems and clarify its relationship with previous methods.

La física de los sistemas desordenados es un campo amplio y en constante evolución. En este trabajo, nos centramos en el estudio de modelos de variables discretas con interacciones asimétricas, específicamente el modelo ferromagnético completamente asimétrico y el modelo Sherrington-Kirkpatrick completamente asimétrico. Utilizamos la ecuación maestra de cavidad, una técnica conocida para describir la dinámica fuera del equilibrio, para derivar ecuaciones promedio que describen la evolución temporal de la magnetización y la energía. De esta manera, recuperamos los resultados previos de la literatura sobre la magnetización y obtuvimos nuevas ecuaciones para la energía de estos modelos. Con este trabajo, contribuimos a asentar la ecuación maestra de cavidad como una de las técnicas más relevantes en el estudio de sistemas fuera de equilibrio y esclarecemos su relación con métodos previos.

Keywords: Cavity Master Equation (Ecuación maestra de cavidad), Discrete Variable Models (Modelos de variables discretas), Dynamic Cavity Method (Método de cavidad dinámico), Asymmetric Interactions (Interacciones asimétricas).

I. INTRODUCTION

The dynamic cavity method is a powerful tool in statistical physics and complex systems theory. It is used to derive both average equations and specific equations for individual graphs describing the macroscopic behavior of systems with many interactions. This method has proven to be particularly useful in the study of disordered systems [1–5]. Some methods that preced and influenced the dynamic cavity method are: the static-cavity method [6], the replica method [7], the dynamic mean-field theory (i.e. IBMF and PBMF) [8–10] and message-passing algorithms [11].

In this work we explore the application of the dynamic cavity method to obtain average equations in two specific models: fully-asymmetric ferromagnet [8] and the fully-asymmetric Sherrington-Kirkpatrick [12]. Specifically, in the dynamic cavity method, we use the cavity master equation (CME), first presented in [1]. These two models selected by us share two relevant qualities that make them more attractive. First, the asymmetry in the interactions allows us to propose suitable factorizations for the system's joint probability distribution, obtaining closed forms for the average equations. Second, we found previous analytic results in the literature in both cases [8, 9], which is a rare resource when studying the dynamics of disordered systems. Indeed, we insert this work in a field where few advances have been made over the years, and it is therefore important that we manage to connect a recently developed technique like the CME with known results.

We recover the equations obtained in [8] for the magnetization of the fully-asymmetric ferromagnet. In addition, we present here equations for the time evolution of the energy of the system not yet published and which were recently introduced in the Ph.D. thesis of [13]. On the other hand, from the same CME we re-derive the equations for the magnetization of the fully-asymmetric Sherrington-Kirkpatrick, already introduced in [9]. In the latter case, we obtain for the first time a set of equations for the time evolution of the system's energy.

The rest of this paper is organized as follows: first, we present the theoretical basis and how the cavity master equation is used in both models. Then, we analyze each model individually and show how to obtain averaged equations for the magnetization and energy from the cavity master equation. Finally, their prediction is compared with the results of numerical simulations.

II. THEORETICAL BASIS

In its first level of approximation, the cavity master equation is given as follows [1, 14]:

$$\frac{dp^t(\sigma_i \mid \sigma_j)}{dt} = -\sum_{\sigma_i'} \sigma_i \sigma_i' \, p^t(\sigma_i' \mid \sigma_j) \sum_{\sigma_{\partial i \setminus j}} r_i(\sigma_i', \sigma_j) \prod_{k \in \partial i \setminus j} p^t(\sigma_k \mid \sigma_i') \tag{1}$$

This equation is written for the continuous-time dynamics of a system with N discrete variables $\vec{\sigma} = \{\sigma_1, \ldots, \sigma_N\}$. The function r_i is the spin transition probability for σ_i, given the configuration of its neighbors. The dynamics is sequential or asynchronous, , *that is*,, we allow only one variable to change its value at each time t. In this case, we selected Glauber's dynamical rule [15]:

$$r_i(\sigma_i, \sigma_j, \sigma_{\partial i \setminus j}) = \frac{\alpha}{2}(1 - \sigma_i \tanh(\beta \sum_{k \in \partial i \setminus j} J_{ki}\sigma_k + \beta J_{ji}\sigma_j)) \tag{2}$$

where α provides a dynamical time scale, β is the inverse of the temperature, and the parameters J_{ij} are the couplings between interacting spins.

This was a special choice for running the simulations. However, they can be performed with any transition probability r_i that depends on the instantaneous values of the spins of the system. The pair probability equation is a particular case of the closure developed in Ref. [16]:

$$\begin{aligned}\frac{dP^t(\sigma_i, \sigma_j)}{dt} = &-\sum_{\sigma_i'} \sigma_i \sigma_i' \, P^t(\sigma_i', \sigma_j) \sum_{\sigma_{\partial i \setminus j}} r_i(\sigma_i', \sigma_j) \prod_{k \in \partial i \setminus j} p^t(\sigma_k \mid \sigma_i') \\ &-\sum_{\sigma_j'} \sigma_j \sigma_j' \, P^t(\sigma_i, \sigma_j') \sum_{\sigma_{\partial j \setminus i}} r_j(\sigma_j', \sigma_i) \prod_{k \in \partial j \setminus i} p^t(\sigma_k \mid \sigma_j')\end{aligned} \tag{3}$$

Taking a marginal of the Eq. (3) we obtain the individual probabilities $P(\sigma_j)$:

$$\begin{aligned}\frac{dP^t(\sigma_j)}{dt} = &-\sum_{\sigma_j'} \sigma_j \sigma_j' \sum_{\sigma_i} P^t(\sigma_i, \sigma_j') \times \\ &\times \sum_{\sigma_{\partial j \setminus i}} r_j(\sigma_j', \sigma_i) \prod_{k \in \partial j \setminus i} p^t(\sigma_k \mid \sigma_j')\end{aligned} \tag{4}$$

The Eq. (4) replaces the equation derived in [1]:

$$\begin{aligned}\frac{dP^t(\sigma_j)}{dt} = &-\sum_{\sigma_j'} \sigma_j \sigma_j' \sum_{\sigma_i} P^t(\sigma_j') \, p^t(\sigma_i \mid \sigma_j') \times \\ &\times \sum_{\sigma_{\partial j \setminus i}} r_j(\sigma_j', \sigma_i) \prod_{k \in \partial j \setminus i} p^t(\sigma_k \mid \sigma_j')\end{aligned} \tag{5}$$

As can be seen the Eq. (5) has a factor $P^t(\sigma_j') \, p^t(\sigma_i \mid \sigma_j')$ while the Eq. (4) has $P^t(\sigma_i, \sigma_j') = P^t(\sigma_j') \, P^t(\sigma_i \mid \sigma_j')$. This means that the Eq. (4) can be obtained from the Eq. (5) by replacing the conditional probability of the cavity $p^t(\sigma_i \mid \sigma_j')$ by the corresponding conditional probability $P^t(\sigma_i \mid \sigma_j')$.

III. FULLY-ASYMMETRIC FERROMAGNET

III.1. Magnetization

The key point of the following derivation is that, due to fully asymmetric interactions (unidirectional influence between variables), the probability distribution of the local field $h_i = \sum_{k \in \partial i} J_{ki}\sigma_i$ is independent of the corresponding spin σ_i. In models like this, where the sum $\sum_k J_{ki}J_{ik}$ vanishes in the thermodynamic limit, the Onsaguer reaction term [6] is not present and the spin σ_i has no effect on the field h_i.

The model couplings are obtained from the distribution:

$$Q(J_{ki}) = \frac{\lambda}{N-1} \, \delta(J_{ki} - 1) + (1 - \frac{\lambda}{N-1}) \, \delta(J_{ki}) \tag{6}$$

We use this distribution to build the graph of interactions. For every possible pair (ik) in the system, J_{ki} and J_{ik} are drawn independently. Therefore, for finite λ and in the thermodynamic limit, the probability of $J_{ki} = J_{ik} = 1$ vanishes. This means that in the Eq. (4), given $J_{ki} = 1$, we know that $J_{ik} = 0$. So, the variables $p(\sigma_k \mid \sigma_j')$ in Eq. (1) do not really depend on σ_j'.

Using this and applying the operator $\sum_{\sigma_i} \sigma_i[\cdot]$ to the Eq. (4) yields:

$$\begin{aligned}\frac{dm_j(t)}{dt} = &-\alpha \, m_j(t) + \alpha \sum_{\sigma_j'} \sum_{\sigma_i} P(\sigma_i, \sigma_j') \times \\ &\times \sum_{\sigma_{\partial j \setminus i}} \tanh(\beta \sum_{k \in \partial j} J_{kj}\sigma_k) \prod_{k \in \partial j \setminus i} \left(\frac{1 + \sigma_k \nu_k}{2}\right)\end{aligned} \tag{7}$$

where we have made $p(\sigma_k \mid \sigma_j') \equiv p(\sigma_k) = \frac{1+\sigma_k\nu_k}{2}$ and we have defined $m_i(t) \equiv \sum_{\sigma_i} \sigma_i P(\sigma_i)$ and $\nu_i(t) \equiv \sum_{\sigma_i} \sigma_i p(\sigma_i)$. Explicitly doing the summation by σ_j' in the Eq. (7) and using $P(\sigma_i) = \frac{1+\sigma_i m_i}{2}$ we get:

$$\begin{aligned}\frac{dm_j(t)}{dt} = &-\alpha \, m_j(t) + \alpha \sum_{\sigma_{\partial j}} \tanh(\beta \sum_{k \in \partial j} J_{kj}\sigma_k) \times \\ &\times \left(\frac{1 + \sigma_i m_i}{2}\right) \prod_{k \in \partial j \setminus i} \left(\frac{1 + \sigma_k \nu_k}{2}\right)\end{aligned} \tag{8}$$

With this, we find the distribution of the local fields h_j acting on site j:

$$D(h_j) = \left(\frac{1 + \sigma_i m_i}{2}\right) \prod_{k \in \partial j \setminus i} \left(\frac{1 + \sigma_k \nu_k}{2}\right) \tag{9}$$

In fact, we could perform the summation over σ_j' because the distribution $D(h_j)$ is independent of σ_j' as mentioned above.

Analogously, we can get an equation for $\frac{dv}{dt}$:

$$\frac{dv_j(t)}{dt} = -\alpha\, v_j(t) + \alpha \sum_{\sigma_{\partial j}} \tanh(\beta \sum_{k\in\partial j} J_{kj}\sigma_k) \times \\ \times\Big(\frac{1+\sigma_i v_i}{2}\Big) \prod_{k\in\partial j\setminus i} \Big(\frac{1+\sigma_k v_k}{2}\Big) \tag{10}$$

Therefore, if we choose an initial condition such that $m_i(0) = v_i(0)$ for all $i = 1, ..., N$, we have $m_i(t) = v_i(t)$ for all $t > 0$. This allows us to rewrite the Eq. (7) as:

$$\frac{dm_j(t)}{dt} = -\alpha\, m_j(t) + \alpha \sum_{\sigma_{\partial j}} \tanh(\beta \sum_{k\in\partial j} J_{kj}\sigma_k) \prod_{k\in\partial j} \Big(\frac{1+\sigma_k m_k}{2}\Big) \tag{11}$$

We can average this equation over the graph ensemble given by the Eq. (6). The result is a special case of a result of Derrida *et al.* in [8]:

$$\frac{d\hat{m}(t)}{dt} = -\alpha\, \hat{m}(t) + \alpha e^{-\lambda}\, S(\hat{m}, \beta, \lambda, 0) \tag{12}$$

where we define:

$$S(\hat{m}, \beta, q, \sigma) = \sum_{k=0}^{\infty} \frac{q^k}{k!} \sum_{n=0}^{k} \binom{k}{n} \Big(\frac{1+\hat{m}}{2}\Big)^n \times \\ \times\Big(\frac{1-\hat{m}}{2}\Big)^{k-n} \tanh(\beta(2n-k+\sigma)) \tag{13}$$

Now we will try to simplify this equation. Exchanging the sums and making the change of variables $l = k - n$, then $n' = n - l$ and substituting the modified Bessel function of first order:

$$S(\hat{m}, \beta, q, \sigma) = \sum_{n'=-\infty}^{\infty} \tanh(\beta(n'+\sigma)) \Big(\frac{1+\hat{m}}{1-\hat{m}}\Big)^{n'/2} \mathrm{I}_{n'}(q\ \sqrt{1-\hat{m}^2}) \tag{14}$$

This shows that the probability of having a local field $\hat{h} = n$, which does not account for the connectivity of the node is:

$$D(\hat{h}{=}n) = \Big(\frac{1+\hat{m}}{1-\hat{m}}\Big)^{n/2} \mathrm{I}_n(\lambda\ \sqrt{1-\hat{m}^2}) \tag{15}$$

III.2. Energy

In these out-of-equilibrium models, there is no Hamiltonian and, therefore, the word energy cannot have the traditional meaning. However, we used the concept of energy as a measure of the average intensity of the interactions between the spins.

If one wants to know how strongly two spins interact, it becomes necessary to extract information from the pair probabilities in Eq. (3). As with single-site probabilities, we can get the equation for average pair probabilities $\hat{P}_{J_{12},J_{21}}(\sigma_1, \sigma_2) \equiv \hat{P}_{J_1,J_2}(\sigma_1, \sigma_2)$:

$$\frac{d\hat{P}_{J_1,J_2}(\sigma_1,\sigma_2)}{dt} = -\frac{\alpha}{2} \sum_{\sigma} (\sigma\sigma_1 \hat{P}_{J_1,J_2}(\sigma,\sigma_2) + \sigma\sigma_2 \hat{P}_{J_1,J_2}(\sigma_1,\sigma)) \\ + \frac{\alpha\sigma_1}{2}\Big[\sum_{\sigma} \hat{P}_{J_1,J_2}(\sigma,\sigma_2)\Big] e^{-\lambda}\, S(\hat{m}, \beta, \lambda, J_2\sigma_2) \\ + \frac{\alpha\sigma_2}{2}\Big[\sum_{\sigma} \hat{P}_{J_1,J_2}(\sigma_1,\sigma)\Big] e^{-\lambda}\, S(\hat{m}, \beta, \lambda, J_1\sigma_1) \tag{16}$$

Defining the energy as:

$$\hat{e}(t) = -\lambda \int dJ_1 dJ_2 Q_c(J_1, J_2)(J_1 + J_2) \times \\ \times \sum_{\sigma_1,\sigma_2} \sigma_1\, \sigma_2\, \hat{P}_{J_1,J_2}(\sigma_1, \sigma_2) \tag{17}$$

For this definition of $\hat{e}(t)$ to make sense, we average over pairs (σ_1, σ_2) that are connected in the graph. In the large size limit, this means that $J_1 = 0$ and $J_2 = 1$ or $J_1 = 1$ and $J_2 = 0$. Therefore, we introduce the *connected* distribution $Q_c(J_1, J_2) = [\delta(J_1)\delta(J_2-1) + \delta(J_2)\delta(J_1-1)]/2$, which in practice is the joint probability distribution of (J_1, J_2) conditioned on one of them being nonzero. Therefore:

$$\hat{e}(t) = -\frac{\lambda}{2} \sum_{\sigma_1,\sigma_2} \sigma_1\, \sigma_2 \Big[\hat{P}_{J_1=1,J_2=0}(\sigma_1,\sigma_2) + \hat{P}_{J_1=0,J_2=1}(\sigma_1,\sigma_2)\Big] \tag{18}$$

and we can compute the average system's energy solving simultaneously the Eq. (16) and Eq. (12), and then applying them into Eq. (18). The reader should notice that, when $J_{ij} = \{0, 1\}$, the energy $\hat{e}$ is directly proportional to the correlation $\hat{c}$ (more explicitly, $\hat{e} = -\lambda\hat{c}$). However, this definition will be of use when the couplings J_{ij} are not binary, as will happen for the Sherrington-Kirkpatrick model in the next section.

In Fig. 1, we compare the results of the average equations for $\lambda = 3$ with Monte Carlo simulations in graphs consisting of $N = 1000$ nodes that were randomly generated using the distribution in Eq. (6). Our average equations are a good description for the system's magnetization and energy for all times and temperatures that were tested. Both simulations and average case predictions display the well-known transition between ferromagnetic and paramagnetic steady states. For $T < 1.8$, the magnetization decays to zero in a short time, while for $T > 1.8$ the system remains magnetized for all times. Since our equations for the magnetization recover the exact result in Ref. [8], we know that all possible discrepancies must come from the finite size effects in the statistics of Monte Carlo simulations.

Through the Eq. (12) we have connected the dynamic cavity method with a known result from a 1987 article [8]. However, in that article, it was assumed that the system's size N was big enough to satisfy $\lambda^m \ll N^{1/2}$, for a system that gets m sequential updates from its starting position.

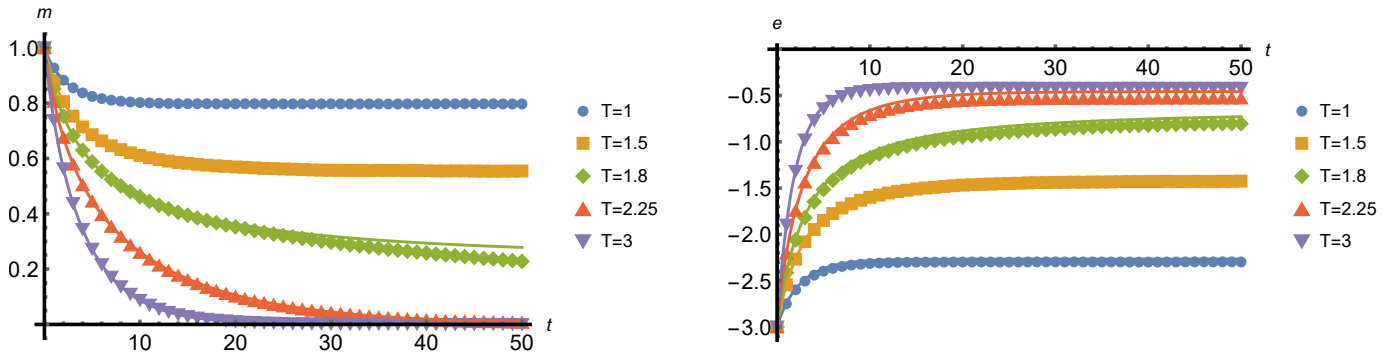

Figure 1. Comparison between the average equations (continuous lines) and Monte Carlo's results (dots) in the fully-asymmetric ferromagnet with $N = 1000$ and $\lambda = 3$. All the calculations were done for a system initially fully magnetized in contact with a heat bath at a given temperature T. Dots are the average for $s = 300$ different graphs. For each one, $n = 10000$ Monte Carlo's histories were averaged.

A common algorithm like Monte Carlo makes typically $O(10N)$ updates, which being $\lambda \geq 2$ implies that the system's size should be big to sustain the former hypothesis.

Our equations do not have such a problem. They have the advantage of being just the average of single-instance equations. This means that we could also reproduce the temporal evolution of a finite system's magnetization and energy. It should also be noted that the energy appearing in Eq. (18) is directly related to the average correlation between the connected variables.

IV. FULLY-ASYMMETRIC SHERRINGTON-KIRKPATRICK

The Sherrington-Kirkpatrick model is a theoretical framework used to describe spin glass systems, introduced in Ref. [12]. It is an Ising model with long-distance interactions where the couplings between spins can be ferromagnetic or antiferromagnetic and they are randomly distributed.

The couplings are drawn from this distribution:

$$Q(J_{ki}) = \sqrt{\frac{N}{2\pi J^2}}\, \exp\{-\frac{N}{2J^2}(J_{ki} - J_0/N)^2\} \tag{19}$$

Unlike the usual Sherrington-Kirkpatrick model, the choice of J_{kl} is independent of J_{lk}. This is the reason for calling it fully asymmetric Sherrington-Kirkpatrick. Notice that, in contrast with the fully asymmetric ferromagnet defined over sparse graphs, the fully-asymmetric Sherrington-Kirkpatrick is defined over fully connected graphs.

IV.1. Magnetization

The local cavity magnetizations $m_j(\sigma_i) = \sum_{\sigma_j} \sigma_j p(\sigma_j \mid \sigma_i)$ follow the following equation:

$$\frac{dm_j(\sigma_i)}{dt} = -\alpha\, m_j(\sigma_i) + \alpha \sum_{\sigma'_j} p(\sigma'_j|\sigma_i) \times \sum_{\sigma_{\partial j\setminus i}} \tanh(\beta \sum_{k\in\partial j} J_{kj}\sigma_k) \prod_{k\in\partial j\setminus i} p(\sigma_k|\sigma'_j) \tag{20}$$

where ∂j has all the nodes in the system, except for σ_j.

Due to the asymmetry of the couplings, the sum $\sum_l J_{lk}J_{kl}$ is of the order $O(1/N)$ and the Onsaguer reaction term is not present. We can then formally establish that the probabilities $p(\sigma_k \mid \sigma'_j)$ will not depend on the couplings J_{kl}, but on J_{lk} with $l \in \partial k$.

Averaging Eq. (20) over the disorder:

$$\frac{d\hat{m}(\sigma)}{dt} = -\alpha\, \hat{m}(\sigma) + \alpha \sum_{\sigma'} \int \Big[\prod_{k=1}^{N-2} dJ_k Q(J_k)\Big] \times \int dJ_i Q(J_i) p_{\{J_k\},J_i}(\sigma'|\sigma) \times \sum_{\{\sigma_k\}} \tanh(\beta \sum_k J_k\sigma_k + J_i\sigma) \prod_k \hat{p}(\sigma_k|\sigma') \tag{21}$$

where we have explicitly written the dependency of each $p(\sigma'_j \mid \sigma_i)$ on the system's couplings. we have defined $\hat{p}(\sigma_k \mid \sigma'_j)$ as the average over all J_{lk} from $p_{\{J_{lk}\}}(\sigma_k|\sigma'_j)$.

As can be seen from Eq. (19) and Eq. (21), the contribution related to J_{ij} within the hyperbolic tangent is of order $O(1/N)$. This means that in the thermodynamic limit we can ignore the term $J_i\sigma$. Also, we can set a starting condition such that $\hat{m}(1) = \hat{m}(-1)$, then we will have a unique equation for both and drop the dependency on σ. Then explicitly integrating over J_i and summing over σ':

$$\frac{d\hat{m}}{dt} = -\alpha\, \hat{m} + \alpha \int \Big[\prod_{k=1}^{N-2} dJ_k Q(J_k)\Big] \times \sum_{\langle\sigma_k\rangle} \tanh(\beta \sum_k J_k\sigma_k) \prod_k \hat{p}(\sigma_k) \tag{22}$$

On the other hand, we can similarly obtain an equation for magnetization defined as $M_j(t) = \sum_{\sigma_j} \sigma_j P_j(\sigma_j)$:

$$\frac{d\hat{M}}{dt} = -\alpha\,\hat{M} + \alpha \int \Big[\prod_{k=1}^{N-2} dJ_k Q(J_k)\Big] \times \times \sum_{\sigma_k} \tanh(\beta \sum_k J_k\sigma_k) \prod_k \hat{p}(\sigma_k) \tag{23}$$

If we set a starting condition such that $\hat{m}(0) = \hat{M}(0)$, we will have $\hat{m}(t) = \hat{M}(t)$ for all $t > 0$, and just one equation:

$$\frac{d\hat{m}}{dt} = -\alpha\,\hat{m} + \alpha \int \Big[\prod_{k=1}^{N-2} dJ_k Q(J_k)\Big] \times \times \sum_{\{\sigma_k\}} \tanh(\beta \sum_k J_k\sigma_k) \prod_k \hat{p}(\sigma_k) \tag{24}$$

Then, we need to compute the Gaussian integral in the second term on the right side:

$$I(\hat{m},\beta,J_0,J,\eta) = \int \Big[\prod_{k=1}^{N-2} dJ_k Q(J_k)\Big] \times \times \sum_{\{\sigma_k\}} \tanh\left[\beta(\sum_k J_k\sigma_k + \eta)\right] \prod_k \hat{p}(\sigma_k) \tag{25}$$

As all variables J_k follow a Gaussian distribution, the variable $\zeta = \sum_k J_k\sigma_k$ will also follow a Gaussian distribution. Then defining $Dy \equiv e^{-y^2/2}/\sqrt{2\pi}$ where $y = (\zeta - \langle\zeta\rangle)/J^2$ we get:

$$I(\hat{m},\beta,J_0,J,\eta) = \int Dy \sum_{\{\sigma_k\}} \Big[\prod_k \hat{p}(\sigma_k)\Big] \tanh\left[\beta(\frac{J_0}{N}\sum_k \sigma_k + J\,y + \eta)\right] \tag{26}$$

For $N \gg 1$, the variable $h = \frac{1}{N}\sum_k \sigma_k$ is a sum of a great number of independent and identically distributed variables, also distributed as a Gaussian. Therefore, at the thermodynamic limit we get $I(\hat{m},\beta,J_0,J,\eta)$:

$$I(\hat{m},\beta,J_0,J,\eta) = \int Dy \tanh\left[\beta(J_0\,\hat{m} + J\,y + \eta)\right] \tag{27}$$

The equation for system's magnetization is then:

$$\frac{d\hat{m}}{dt} = -\alpha\,\hat{m} + \alpha I(\hat{m},\beta,J_0,J,0) \tag{28}$$

which reproduces the analytical results presented in [9].

IV.2. Energy

We will also obtain an equation for the energy of the system as we did in Eq. (17):

$$\hat{e}(t) = -\frac{N}{2}\int dJ_1 dJ_2 Q(J_1,J_2)\frac{(J_1+J_2)}{2} \times \sum_{\sigma_1,\sigma_2} \sigma_1\,\sigma_2\,\hat{P}_{J_1,J_2}(\sigma_1,\sigma_2) \tag{29}$$

As last time, this is not the usual energy; it is more like a measure of the intensity of spin interactions. Starting from an analogous equation to Eq. (16):

$$\begin{aligned}\frac{d\hat{P}_{J_1,J_2}(\sigma_1,\sigma_2)}{dt} = &-\frac{\alpha}{2}\sum_\sigma (\sigma\sigma_1\hat{P}_{J_1,J_2}(\sigma,\sigma_2) + \sigma\sigma_2\hat{P}_{J_1,J_2}(\sigma_1,\sigma)) \\ &+ \frac{\alpha\sigma_1}{2}\Big[\sum_\sigma \hat{P}_{J_1,J_2}(\sigma,\sigma_2)\Big] I(\hat{m},\beta,J_0,J,J_2\sigma_2) \\ &+ \frac{\alpha\sigma_2}{2}\Big[\sum_\sigma \hat{P}_{J_1,J_2}(\sigma_1,\sigma)\Big] I(\hat{m},\beta,J_0,J,J_1\sigma_1)\end{aligned} \tag{30}$$

We can then apply the operator:
$-N/2\int dJ_1 dJ_2 Q(J_1,J_2)(J_1+J_2)/2\sum_{\sigma_1}\sum_{\sigma_2}\sigma_1\sigma_2[\cdot]$ and get:

$$\begin{aligned}\frac{d\hat{e}(t)}{dt} = &-2\alpha\hat{e}(t) - \frac{\alpha N}{2}\sum_\sigma \sigma\Big[\int dJ_1 Q(J_1)\,J_1\,\hat{P}_{J_1}(\sigma)\Big] \\ &\times \int dJ_2 Q(J_2) I(\hat{m},\beta,J_0,J,J_2\sigma) \\ &- \frac{\alpha N}{2}\sum_\sigma \sigma\Big[\int dJ_1 Q(J_1)\,\hat{P}_{J_1}(\sigma)\Big] \\ &\times \int dJ_2 Q(J_2)\,J_2\,I(\hat{m},\beta,J_0,J,J_2\sigma)\end{aligned} \tag{31}$$

We know that in the thermodynamic limit:

$$\int dJ_2 Q(J_2) I(\hat{m},\beta,J_0,J,J_2\sigma) = I(\hat{m},\beta,J_0,J,0) \tag{32}$$

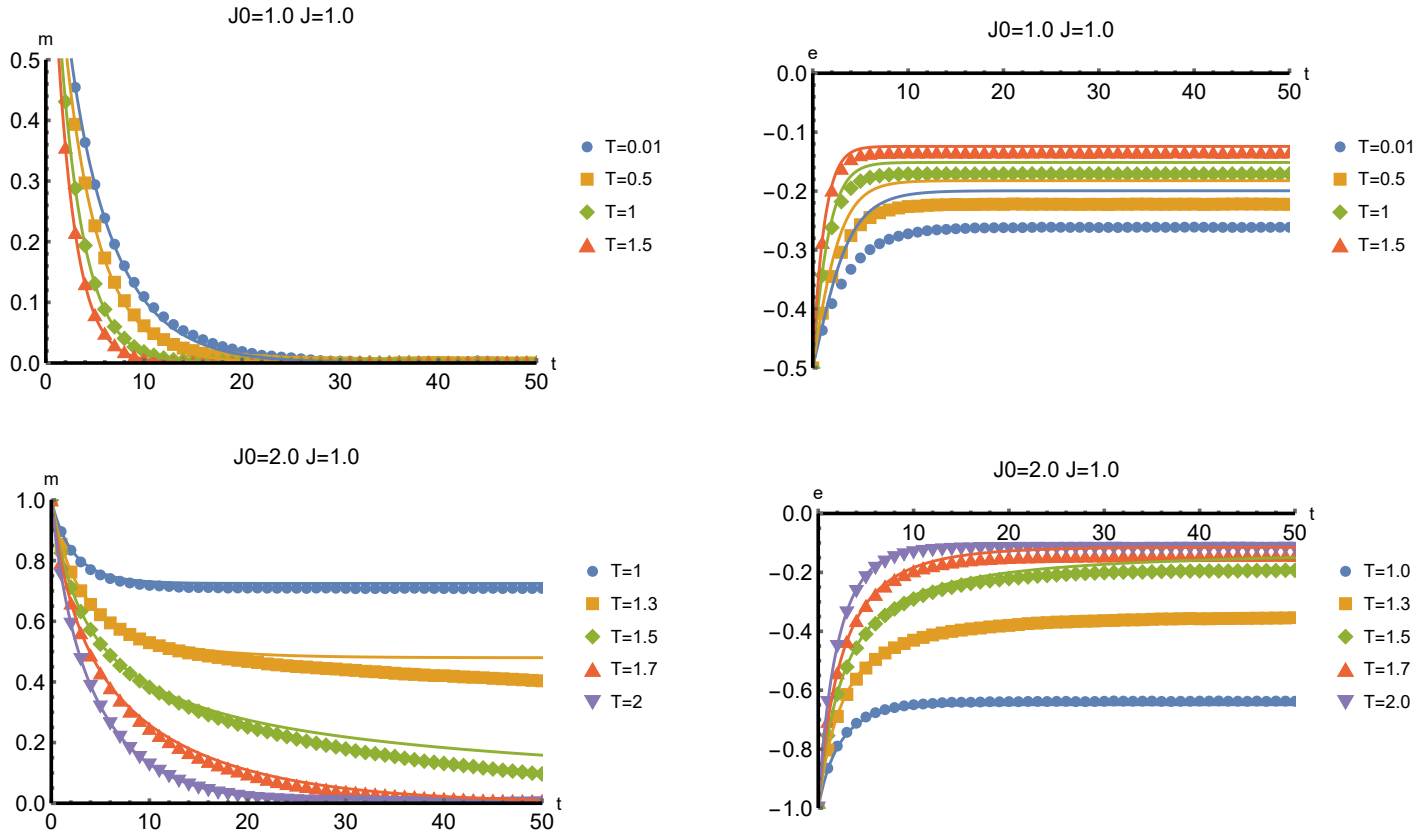

Figure 2. Comparison between average equations (continuous lines) and Monte Carlo's results (dots) in the fully-asymmetric Sherrington-Kirkpatrick. All calculations were done for an initially fully magnetized system in contact with a heat bath at a given temperature T. For each one graph, $n = 100$ Monte Carlo's histories were averaged. Panels (a) and (b): System size is $N = 500$. Points are averages taken over $s = 100$ graphs. Panels (c) and (d): System size is $N = 100$. Points are averages taken over $s = 1000$ graphs.

This leaves us with the task of solving the following integrals:

$$\begin{aligned} N\langle J_1 \hat{m}_{J_1}\rangle &\equiv N\int dJ_1 Q(J_1)\, J_1\, \hat{P}_{J_1}(\sigma) \\ N\langle J_2\, I(J_2\sigma)\rangle &\equiv N\int dJ_2 Q(J_2)\, J_2\, I(\hat{m},\beta,J_0,J,J_2\sigma) \end{aligned} \tag{33}$$

where $\hat{m}_{J_1} = \sum_\sigma \sigma \hat{P}_{J_1}(\sigma)$.

In all of the following derivations, we will use the fact that the integrals are uniformly convergent. Now let's integrate Eq. (33) by parts with:

$$u = \int Dy\, \tanh\left[\beta(J_0\hat{m} + Jy + J_2\sigma)\right] \tag{34}$$

$$dv = dJ_2 \sqrt{\frac{N}{2\pi J^2}} \exp\left\{-\frac{N}{2J^2}(J_2 - \frac{J_0}{N})^2\right\} J_2 \tag{35}$$

Then, we have:

$$N\langle J_2\, I(J_2\sigma)\rangle = N(uv\big|_{-\infty}^{\infty} - \int_{-\infty}^{\infty} vdu) \tag{36}$$

Using $\lim_{x\to\pm\infty} \mathrm{erf}(x) = \lim_{x\to\pm\infty} \tanh(x) = \pm 1$:

$$uv\big|_{-\infty}^{\infty} = \frac{J_0\sigma}{2N}\int Dy - \frac{J_0\sigma}{2N}\int Dy = 0 \tag{37}$$

In the other side:

$$\int_{-\infty}^{\infty} vdu = I_1 + I_2 \tag{38}$$

where we have:

$$\begin{aligned} I_1 = \beta\sigma \int_{-\infty}^{\infty} dJ_2 \left(-\frac{J^2}{N}\sqrt{\frac{N}{2\pi J^2}}\exp\left\{-\frac{N}{2J^2}(J_2 - \frac{J_0}{N})^2\right\}\right) \\ \times \int Dy\, \cosh^{-2}\left[\beta(J_0\hat{m} + Jy + J_2\sigma)\right] \end{aligned} \tag{39a}$$

$$\begin{aligned} I_2 = \beta\sigma \int_{-\infty}^{\infty} dJ_2 \frac{J_0}{2N}\mathrm{erf}\left[\sqrt{\frac{N}{2J^2}}(J_2 - \frac{J_0}{N})\right] \\ \times \int Dy\, \cosh^{-2}\left[\beta(J_0\hat{m} + Jy + J_2\sigma)\right] \end{aligned} \tag{39b}$$

At Eq. (39a) we have the factor $\exp\left\{-\frac{N}{2J^2}(J_2 - \frac{J_0}{N})^2\right\}$, which when N is big, the gaussian will be localized around $J_2 = \frac{J_0}{N}$. Therefore is safe to make the substitution $J_2 = \frac{J_0}{N}$ inside the hyperbolic cosine and then integrating over J_2:

$$I_1 \approx -\frac{\beta\sigma J^2}{N}\int Dy\,\cosh^{-2}\left[\beta(J_0\hat{m}+Jy+\frac{J_0}{N}\sigma)\right] \tag{40}$$

At Eq. (39b), we have the factor $\text{erf}\left[\sqrt{\frac{N}{2J^2}}(J_2-\frac{J_0}{N})\right]$. When N is big enough, $\text{erf}\left[\sqrt{\frac{N}{2J^2}}(J_2-\frac{J_0}{N})\right]\approx sgn(J_2-\frac{J_0}{N})$.

Then exchanging the integral signs and integrating:

$$I_2 \approx -\frac{J_0}{N}\int Dy\,\tanh\left[\beta(J_0\hat{m}+Jy+\frac{J_0}{N}\sigma)\right] \tag{41}$$

Putting it all together and ignoring the $\frac{J_0}{N}\sigma$ inside the hyperbolic functions because they vanish in the thermodynamic limit, we get finally:

$$\begin{aligned} N\langle J_2\, I(J_2\sigma)\rangle = J_0\int Dy\,\tanh\left[\beta(J_0\hat{m}+Jy)\right] \\ +\beta\sigma J^2\int Dy\,\cosh^{-2}\left[\beta(J_0\hat{m}+Jy)\right] \end{aligned} \tag{42}$$

To get an equation for $N\langle J_1\hat{m}_{J_1}\rangle$ we just multiply by J_1 the differential equation for the variable $\hat{m}_{J_1}$, and then integrating the result with weight $Q(J_1)$:

$$\begin{aligned} N\frac{d\langle J_1\hat{m}_{J_1}\rangle}{dt} = -\alpha N\langle J_1\hat{m}_{J_1}\rangle+\alpha J_0\int Dy\tanh\left[\beta(J_0\,\hat{m}\right. \\ \left.+J\,y)\right]+\alpha\hat{m}\beta J^2\int Dy\cosh^{-2}\left[\beta(J_0\,\hat{m}+J\,y)\right] \end{aligned} \tag{43}$$

where there was done an integration by parts to analogously get the second and third terms.

We can solve numerically the system of equations formed by Eq. (31), Eq. (32), Eq. (42) and Eq. (43) with starting conditions $\hat{m}(0)=m_0$, $\hat{e}(0)=-\frac{J_0m_0^2}{2}$ and $N\langle J_1\hat{m}_{J_1}\rangle(0)=J_0m_0$.

In Figs. 2a and 2b, the results from the average equations are compared with Monte Carlo simulations, for $J_0=1,J=1$ and $N=500$. The system's magnetization is well described by our theory, which is to be expected since we again recover known results from the literature that are exact. In the same system, our equations predict steady state energies a bit higher than the ones obtained in the simulations. When $J_0=J=1$, there is no ferromagnetic region and the dynamics always go to a non-magnetized steady state. This does not mean the dynamics is trivial, since correlations do emerge when the temperature is lowered. This mechanism, possibly associated with a glassy dynamics, is not captured in Fig. 2a, where the theory is close to the simulations for high temperatures but fails for low temperatures.

However, we can show that the equations work better in systems with stronger ferromagnetic interactions. In Figs. 2c and Figs. 2d, we can see that for $J_0=2,J=1$ and $N=100$, our theory describes adequately the system's magnetization and the energy as well. Here, we do have a ferromagnetic-paramagnetic transition and the emergence of correlations for low temperatures is due to ferromagnetic interactions. This is, instead, well captured by our equations.

V. CONCLUSIONS

We developed a method to get average case versions of the cavity master equation [1] in asymmetric models. The ideas and the methods can be easily extended to other models.

Our method recovers exact results already known in the literature for the magnetizations of the fully-asymmetric ferromagnet and Sherrington-Kirkpatrick models. Furthermore, we obtain new equations for the energy of both models that reproduce the simulations in most cases.

For specific parameters our equations predict steady-states energies a bit higher than those of the simulations in the fully-asymmetric Sherrington-Kirkpatrick. This is associated to the emergence of non-trivial correlations in the dynamics without magnetization, possibly due to the presence of a glassy dynamics. We plan to analyze the discrepancies observed in this particular case in the future.

REFERENCES

[1] E. Aurell, G. D. Ferraro, E. Domínguez, R. Mulet, *Phys. Rev. E* **95**, 052119 (2017).

[2] E. Aurell, E. Domínguez, D. Machado, R. Mulet, *Phys. Rev. E* **97**, 05103(R) (2018).

[3] E. Domínguez, D. Machado, R. Mulet, *J. Stat. Mech: Theory Exp.* **2020**, 073304 (2020).

[4] E. Aurell, G. Del Ferraro, E. Domínguez, R. Mulet, *Phys. Rev. E* **95**, 052119 (2017).

[5] E. Aurell, H. Mahmoudi, *Phys. Rev. E* **85**, 031119 (2012).

[6] M. Mézard, G. Parisi, *J. Stat. Phys.* **111**, 1 (2003).

[7] M. Mézard, G. Parisi, N. Sourlas, G. Toulouse, M. Virasoro, *J. Phys.* **45**, 843 (1984).

[8] B. Derrida, E. Gardner, A. Zippelius, *Europhys. Lett.* **4**, 167 (1987).

[9] A. Crisanti and H. Sompolinsky, *Phys. Rev. A* **37**, 4865 (1988).

[10] F. Zamponi, arXiv preprint arXiv:1008.4844 (2010).

[11] A. Lage-Castellanos, R. Mulet, F. Ricci-Tersenghi, *Europhys. Lett.* **107**, 57011 (2014).

[12] D. Sherrington, S. Kirkpatrick, *Phys. Rev. Lett.* **35**, 1792 (1975).

[13] D. Machado, *Dinámica de variables discretas en grafos aleatorios*, Phd thesis, Universidad de La Habana (2024).

[14] D. Machado, R. Mulet, *Phys. Rev. E* **104**, 054303 (2021), ISSN 2470-0053.

[15] R. J. Glauber, *J. Math. Phys.* **4**, 294 (1963).

[16] E. Aurell, D. M. Perez, R. Mulet, *J. Phys. A: Math. Theor.* **56**, 17LT02 (2022), ISSN 1751-8121.

QUASI-CLASSICAL DYNAMICS OF HYDROGEN MOLECULES TRAPPED INSIDE FULLERENE CAGES

DINÁMICA CUASI-CLÁSICA DE MOLÉCULAS DE HIDRÓGENO ATRAPADAS EN FULERENOS

J. A. Heredia-Kindelán[a,c], L. D. Fernández-Quintana[a,c], N. Halberstadt[b], L. Uranga-Piña[b,c], A. Martínez-Mesa[c†]

a) Departamento de Física, Universidad de Oriente, Santiago de Cuba, Cuba.
b) Laboratoire Collisions Agrégats Réactivité (FeRMI), Université de Toulouse III and CNRS, UMR 5589, F-31062 Toulouse Cedex 09, France.
c) DynAMoS (Dynamical processes in Atomic and Molecular Systems), Facultad de Física, Universidad de la Habana, La Habana, Cuba. aliezer@fisica.uh.cu†
† corresponding author

Recibido 19/1/2025; Aceptado 31/5/2025

We perform molecular dynamics simulations of hydrogen molecules inside fullerene cages, incorporating quantum effects via the Feynman-Hibbs effective potential method. The distance between hydrogen atoms in the molecule is kept fixed by using the constraint dynamics algorithm. We evaluate the energetic properties and the influence of quantum effects for hydrogen molecules in fullerene cages of varying size and geometry (C_n, $n = 24, 28, 60, 70$), and within a wide range of thermodynamics conditions (i.e., from $T = 130$ K to $T = 320$ K). We compute the temperature dependence of quantities such as the translational and rotational kinetic energies, the total energy and the contribution of quantum effects. It is found that quantum corrections to the total energy are significant even at room temperature. We discuss the possible influence of these properties on the hydrogen storage capacity of these materials.

Simulamos la dinámica de moléculas de hidrógeno dentro de fulerenos en forma de jaula, incorporando los efectos cuánticos mediante el método del potencial efectivo de Feynman-Hibbs. La distancia entre los átomos de hidrógeno se mantiene fija utilizando el método de dinámica molecular con ligaduras. Evaluamos las propiedades energéticas y la influencia de los efectos cuánticos de moléculas de hidrógeno en fulerenos de distintos tamaños y geometrías (C_n, $n = 24, 28, 60, 70$), dentro de un rango amplio de condiciones termodinámicas ($T = 130$ K hasta $T = 320$ K). Se estudió la dependencia, con respecto a la temperatura, de magnitudes como las energías cinéticas de traslación y de rotación, la energía total y la contribución de los efectos cuánticos. Se determinó que las correcciones cuánticas a la energía son significativas incluso a temperatura ambiente. Discutimos la posible influencia de estas propiedades sobre el almacenamiento de hidrógeno en estos materiales.

Keywords: Molecular dynamics simulations (Simulaciones de dinámica molecular); Semiclassical molecular dynamics (dinámica molecular semiclásica); Hydrogen storage (almacenamiento de hidrógeno).

I. INTRODUCTION

Today, hydrogen is considered one of the main alternatives to fossil fuels for mobile applications [1]. Hydrogen is an environmentally friendly renewable energy carrier with promising applications in various sectors. For example, efforts are underway to adopt hydrogen as a fuel in transportation, stationary and portable back-up power plants, power supply to off-grid areas, among other usages [2].

Despite its high energy density and environmentally safe nature, large-scale exploitation of hydrogen as a fuel constitutes a challenge for modern science, particularly concerning safe and efficient hydrogen storage for mobile applications. Various technologies have been developed to store hydrogen, such as compressed hydrogen gas tanks, liquefaction, chemically in the form of solid hydrides or by spillover of hydrogen, or by physical adsorption in porous materials [2–6]. Currently, none of these methods can meet the current reference U.S. Department of Energy goals for efficient on-board hydrogen storage, or they bear high energy consumption or high material costs [1].

Physisorption on nanostructured surfaces is one of the most promising alternatives to store hydrogen due to the typically high energy density attained, the reversibility, and the fast kinetics [7]. Specifically, hydrogen uptake by carbon-based nanomaterials provides valuable insight into the microscopic mechanisms underlying the adsorption process. The wide variety of thermodynamically stable carbon allotropes enables several parameters, such as the pore size and the binding energy, to be tuned almost continuously. Therefore, despite exhibiting lower storage capacities than more complex materials (for example, metal-organic and covalent-organic frameworks), carbonaceous materials remain as widespread model systems for studying H_2 physisorption [8].

While several authors addressed the evaluation of quantum effects on hydrogen physisorption within the featureless particle approximation (see [9], and references therein), studies of rotational quantum dynamics of adsorbed hydrogen molecules are scarce in the literature [10].

The purpose of this paper is to investigate the quasi-classical dynamics of hydrogen molecules encapsulated in fullerene cages of varying sizes, with a focus on the energetics and the emergence of quantum effects. Fullerenes constitute paradigmatic examples of curved carbon nanostructures. They can be regarded as the elementary building blocks of fullerites, which are appealing as hydrogen storage

media [11]. In Section *Methodology*, we describe the computational approach to effective potential molecular dynamics simulations of H_2 molecules inside fullerene cages. The computed energetic properties of endohedral $H_2@C_n$ molecules are presented in section *Results and discussion*. The main findings and some perspectives are summarized in section *Conclusions*.

II. METHODOLOGY

Within the constraint dynamics method [12], the positions of the hydrogen atoms obey the following equations of motion:

$$m\ddot{\vec{r}}_i = \vec{f}_i + \vec{\gamma}_{ij}(t), \tag{1}$$

where $\vec{r}_i$ $(i = 1, 2)$ is the position of the hydrogen atom *ith*, $\vec{f}_i$ is the force exerted on each H atom by the fullerene cage and m is the hydrogen atomic mass. The symbols $\vec{\gamma}_{ij}$ $(i \neq j)$ denote intramolecular constraint forces introduced to keep the distance between hydrogen atoms constant, that is, at each point in time:

$$|\vec{r}_{12}(t + \Delta t)|^2 = |\vec{r}_{21}(t + \Delta t)|^2 = l^2. \tag{2}$$

Here, $\Delta t = 1$ fs is the time step, $l = 0.74$ Å is the equilibrium bond distance in the hydrogen molecule.

The positions $\vec{r}_i$ and velocities $\vec{v}_i$ are propagated as follows:

$$\vec{r}_i(t + \Delta t) = \vec{r}_i(t) + \vec{v}_i(t)\Delta t + \frac{1}{2}\vec{a}_i(t)\Delta t^2, \tag{3}$$

$$\vec{v}_i(t + \Delta t) = \alpha\vec{v}_i(t) + \frac{1}{2}\left[\vec{a}_i(t) + \vec{a}_i(t + \Delta t)\right]\Delta t, \tag{4}$$

where $\vec{a}_i(t) = -\nabla_i V(\vec{r})/m$ is the instantaneous acceleration of the *ith* particle. The vector $\vec{r} = (\vec{r}_1, \vec{r}_2)$ represents the positions of the two hydrogen atoms.

Equations (3) and (4) correspond to the velocity Verlet algorithm [12], augmented by introducing the velocity rescaling factor:

$$\alpha = \sqrt{\frac{K_t}{K}}, \tag{5}$$

which enforces the canonical distribution of the total kinetic energy of the system. The target value K_t of the kinetic energy is drawn randomly from the canonical equilibrium distribution for the kinetic energy [13]:

$$\bar{P}(K_t)dK_t \propto K_T^{N_f/2-1} e^{-\beta K_t} dK_t. \tag{6}$$

N_f is the total number of degrees of freedom in the system.

The interaction potential V between the hydrogen molecule and the (frozen) host structure is modeled as a superposition of pairwise interactions of the form:

$$V(\vec{r}) = \sum_{i,\nu}\left[Ae^{-a|\vec{r}_i - \vec{r}_\nu|} - \frac{C}{\left|\vec{r}_i - \vec{r}_\nu\right|^6}\right], \tag{7}$$

where A, a, and C are constant parameters fitted to ab initio data: $A = 12676$ kcal·mol^{-1}, $a = 3.5763$Å^{-1}, $C = 200.185$ kcal·mol^{-1}Å^6 [14]. $\vec{r}_\nu$ is the position of each carbon atom in the fullerene cage.

The well depth of the C-H pair potential in equation (7) is $6.3 \cdot 10^{-2}$ kcal·mol^{-1}, and the minimum is attained at an interatomic separation of 3.4 Å. Comparatively, the equilibrium C-H distance is 1.46, 1.28, 0.97, and 0.89 times larger than the cage radii of C_{24}, C_{28}, C_{60}, and C_{70} fullerenes, respectively [15]. Therefore, we can expect guest molecules to be tightly confined by repulsive forces at the centre of the C_{24} and C_{28} cages, while the two larger fullerenes display interaction potential minima at the centre of the cavity (for C_{60}), and slightly displaced from the centre (for C_{70}).

As a result of the mismatch between the frequency of the host phonons and the characteristic time scale of the guest molecule motion, the influence of the vibrations of carbon atoms on the computed thermodynamic properties is negligible (within the investigated temperature range). A similar result has been verified for hydrogen storage in carbonaceous nanomaterials, e.g., using frozen phonon models [25]. Therefore, the results reported in following section were obtained assuming a frozen host structure.

In order to account for quantum effects at finite temperature within a molecular dynamics framework, we consider atoms moving on the Feynman-Hibbs effective potential:

$$V_{FH}(\vec{r}) = V(\vec{r}) + \frac{\beta\hbar^2}{24m}\sum_i \nabla_i^2 V(\vec{r}). \tag{8}$$

In equation (8), ∇_i^2 is the Laplacian operator with respect to the coordinates of particle i, $\beta = \frac{1}{k_B T}$ is the inverse temperature, k_B is the Boltzmann constant, and $\hbar$ is the Planck's constant.

The Feynman-Hibbs effective potential has been extensively used to incorporate moderate quantum effects [23, 24]. The second, temperature-dependent term in equation (8) accounts for the effects of quantum delocalization, i.e., it corresponds to the path integral average of position-dependent observables around the classical path, over a region of size equal to the De Broglie thermal wavelength $\sqrt{2\pi\beta\hbar^2/m}$.

For each fullerene cage and for every temperature T, the simulation procedure can be summarized as follows. A hydrogen molecule with random orientation is initially placed inside the carbon framework. The initial position of the molecular centre of mass is assigned randomly around the center of the cage, following a three-dimensional Gaussian distribution of standard deviation equivalent to 40 % of the cage radius. Initial velocities of the centre of mass along each Cartesian axis are drawn from the corresponding Maxwell-Boltzmann distribution. Upon thermalization, properties are calculated as averages over trajectories starting from 40 different initial conditions. In turn, each trajectory is propagated for 150,000 simulation steps.

Furthermore, we examine the validity of a simple model of $H_2@C_{60}$ and $H_2@C_{70}$ endohedral molecules, consisting of decoupled rotational and centre of mass translational motions. To this purpose, the computed average total energies of H_2 in

C_{60} and C_{70} fullerene cages were fitted to the superposition of the internal energies of a three-dimensional isotropic harmonic oscillator (of mass equal to $2m$, its frequency ω is considered as a fitting parameter):

$$\frac{3}{2}\hbar\omega + \frac{3}{2}\frac{\hbar\omega\, e^{-\beta\hbar\omega}}{1-e^{-\beta\hbar\omega}}, \tag{9}$$

and of a free rigid rotor (with rotational constant B_e) [22]:

$$-\frac{\partial}{\partial\beta}\left[\frac{3}{4}\ln\left\{\sum_{l\ even}(2l+1)e^{-\beta B_e l(l+1)}\right\} + \frac{1}{4}\ln\left\{\sum_{l\ odd}(2l+1)e^{-\beta B_e l(l+1)}\right\}\right]. \tag{10}$$

In practice, the sums in equation (10) were approximated with the first three non-zero terms.

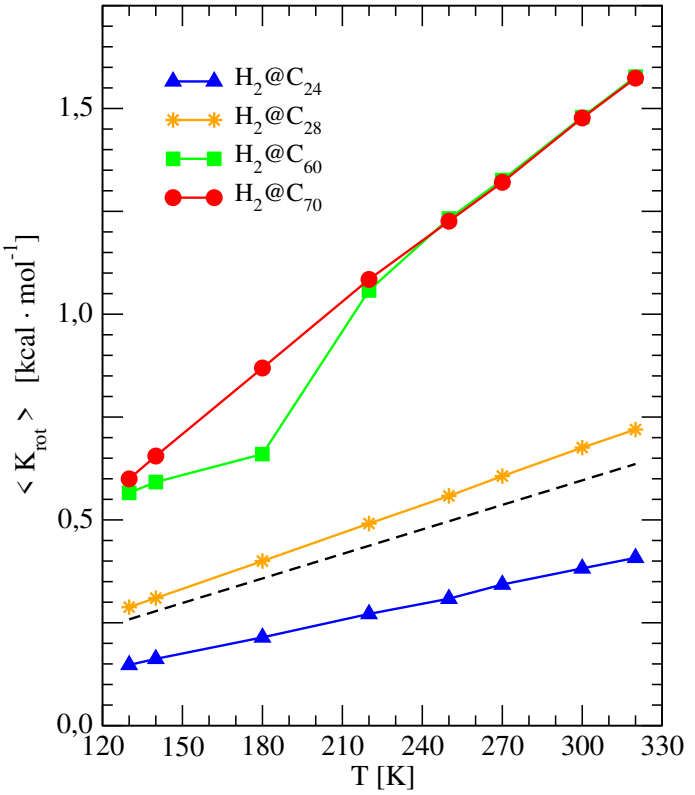

Figure 1. Average rotational kinetic energy $\langle K_{rot}\rangle$ of hydrogen molecules encapsulated in C_{24} (up triangles), C_{28} (stars), C_{60} (squares), and C_{70} (circles), as a function of temperature. The dashed line represents the temperature dependence of the rotational energy of H_2, as predicted by the energy equipartition theorem.

III. RESULTS AND DISCUSSION

In the following, we present the characterization of the energetics of $H_2@C_n$ endohedral fullerenes (n = 24, 28, 60, 70) in the range of temperatures from 130 K up to 320 K.

For each system, the computed total kinetic energy (translational plus rotational) is equal to $N_f/2\beta$, up to numerical fluctuations. However, due to the emergence of quantum effects, the kinetic energy is not evenly partitioned among all degrees of freedom at thermal equilibrium.

Figure 1 illustrates the influence of the confinement potential on the rotational motion of the guest molecule. It can be noticed that H_2 rotation is subject to larger energy barriers in the smaller fullerenes. Still, due to the small bond length of H_2, the molecule is able to complete rotations even in the smallest C_{24} cage.

On the one hand, the rotational energy of H_2 molecules trapped inside C_{24} and C_{28} cages remains rather close and increases with a slope similar to that predicted by the energy equipartition principle, at all temperatures. On the other hand, the rotational energy of hydrogen molecules in C_{60} and C_{70} fullerenes is higher than anticipated by the equipartition theorem. For these two fullerenes, the $\langle K_{rot}\rangle(T)$ curves present steeper slopes on average, compared both to the energy equipartition theorem and the smaller C_{24} and C_{28} cages. It can be seen that the average rotational energy of H_2 is very similar in C_{60} and C_{70} above 220 K, while the former is somewhat lower for temperatures between 130 K and 180 K.

This behaviour can be rationalised by considering the differences in the confinement potential exerted on H_2 molecules by the host structures. The equilibrium position of the H_2 molecule was at the centre of the cavity in C_{60}, whereas two symmetrical equilibrium positions were observed near the centre of the cage in C_{70}, oriented along the major axis. As a consequence of the nearly spherical symmetry, and the size of the buckminsterfullerene (the cage radius is 3.53Å) and C_{70} (geometrical mean radius of 3.83Å), the encapsulated hydrogen molecule behaves almost as a free rotor. Featuring the largest molecular rotational constant in nature (B_e/k_B = 87.17 K), the energy spacing between low-lying rotational levels of the free H_2 molecule (i.e., $2B_e$, $4B_e$, $6B_e$, ...) are similar to or larger than k_BT within the range of thermodynamic conditions investigated here.

The discrete character of the rotational spectra of the encapsulated molecule lies at the origin of the observed deviations from the energy equipartition principle. Although the Feynman-Hibbs method can not take the discrete character of the molecular rotational spectra into account explicitly, the method has been shown to accurately reproduce thermodynamic properties (e.g., the free energy) even in the ultra-quantum limit (i.e., for $E_{n+1} - E_n \gg k_BT$, where n represents a collective quantum number labelling the energy levels of the system) [17].

For the C_{24} and C_{28} cavities, rotational hindering by the anisotropic hydrogen-cage interaction potential creates a higher density of rotational states within the thermal and

subtermal energy regions, and the behaviour predicted by the energy equipartition theorem is approximately recovered. It can be seen, that within the investigated temperature range, the tighter the confinement imposed by the host structure, the smaller the rotational energy of hydrogen molecules encapsulated in the cavity.

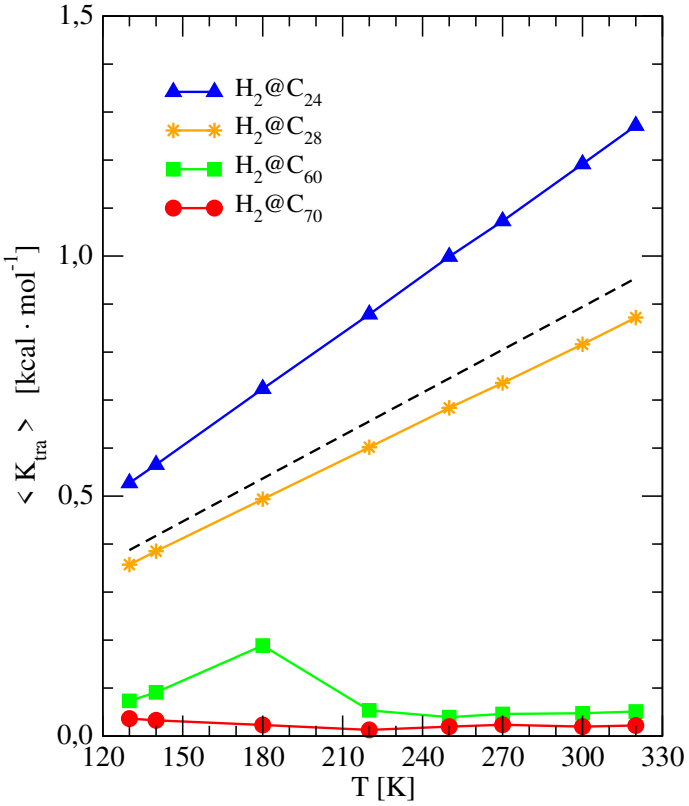

Figure 2. Average translational kinetic energy $\langle K_{tra} \rangle$ of H_2 molecules encapsulated in fullerene cages (C_{24}, C_{28}, C_{60}, and C_{70}), as a function of temperature. The dashed line represents the temperature dependence of the translational energy of H_2, as predicted by the energy equipartition theorem.

In figure 2, we show the average translational kinetic energy $\langle K_{tra} \rangle$ of hydrogen molecules trapped in the fullerene cages. Since the total kinetic energy is proportional to temperature, the temperature dependence of $\langle K_{tra} \rangle$ mirrors that of the average rotational energy. That is, for hydrogen molecules in C_{24} and C_{28}, $\langle K_{tra} \rangle(T)$ increases linearly following a similar trend to that predicted by the energy equipartition theorem. Conversely, the temperature-dependent, average translational kinetic energy of H_2 in C_{60} and C_{70} is comparatively smaller and flatter than for the two smallest fullerenes.

This trend suggests that nanoporous materials displaying inner cavities with sizes and shapes resembling C_{60} and C_{70} cages would be more suitable as hydrogen storage media. Indeed, in these nanostructures, a larger fraction of thermal energy takes the form of rotational rather than translational energy of H_2 molecules. This property translates in smaller vibrational amplitudes of guest molecules around their equilibrium positions in the cage. Since the equilibrium distance of the isotropic average of H_2-H_2 intermolecular interaction is 3.4Å [18], both C_{60}- and C_{70}-like pores can accommodate two H_2 molecules, at the expense of somewhat increased barriers to rotation due to the interaction with pore walls.

The influence of quantum effects on the energetics of $H_2@C_n$ endohedral molecules can be quantified in terms of the extent of the temperature-dependent contribution in the Feynman-Hibbs potential (equation (8)). The plots in figure 3 show that quantum effects are at least one order of magnitude larger in C_{24} and C_{28}, compared to C_{60} and C_{70}, owing to the tightest confinement imposed by the smaller nanostructures on the guest molecules.

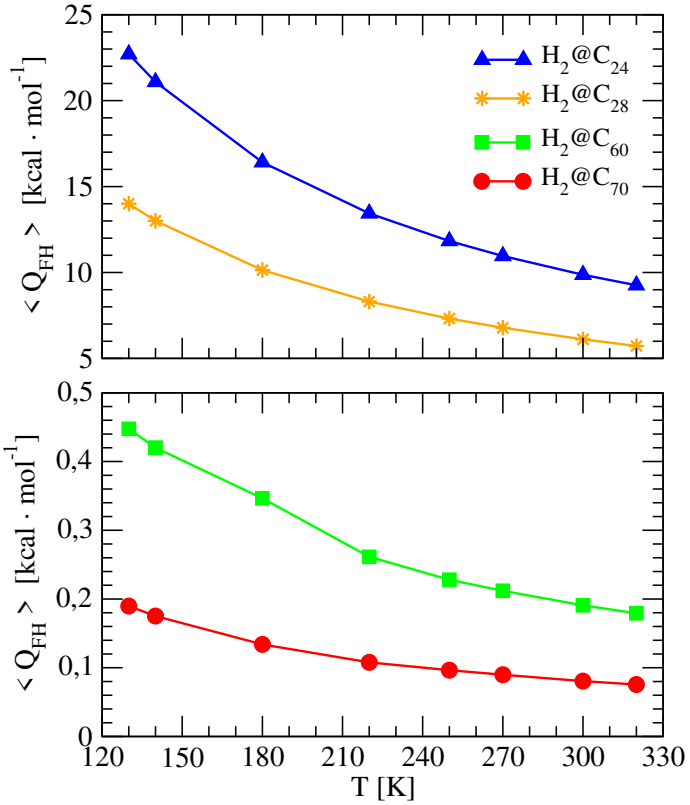

Figure 3. Average quantum contribution $\langle Q_{FH} \rangle$ in the effective Feynman-Hibbs potential for $H_2@C_n$ (n = 24, 28, 60, 70), as a function of temperature.

The magnitude of quantum effects gradually decreases as temperature gets larger, i.e, at T = 320 K, the average quantum contribution to the effective potential drops down to 41 % of its value at T = 130 K, for hydrogen trapped inside C_{24} and C_{28} cages. Within the same interval of temperature, the size of this contribution declines by 43 % and 50 % for the C_{60} and C_{70} fullerenes respectively.

In figure 4, we show the total energy of encapsulated H_2 molecules as a function of temperature. It can be seen that this quantity behaves quite differently in response to cage size.

In C_{24} and C_{28}, guest molecules are confined by repulsive interactions with the cage walls. The hydrogen molecules trapped in these structure undergo a 7% reduction of their total energy when temperature increases from T = 130 K up to 320 K. Such diminution owes chiefly to the reduction of the temperature-dependent contribution to the effective Feynmann-Hibbs potential by 60 % (13.4 kcal·mol^{-1} and 8.3 kcal·mol^{-1} for $H_2@C_{24}$ and $H_2@C_{28}$, respectively).

The Feynmann-Hibbs quantum correction gets smaller as a consequence of the decrease of the De Broglie thermal wavelength.

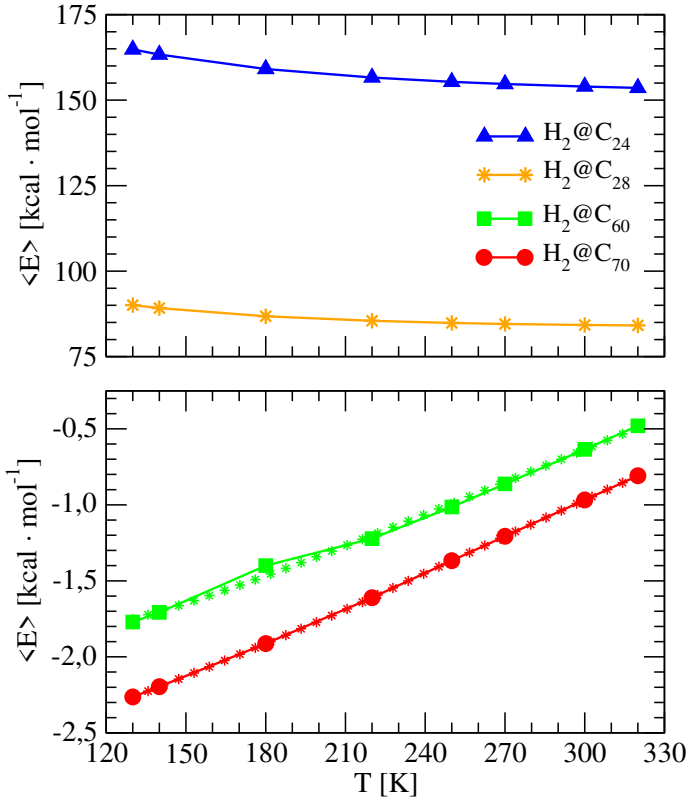

Figure 4. Average total energy ⟨E⟩ of H_2 molecules trapped in C_{24}, C_{28}, C_{60}, and C_{70} fullerene cages, as a function of temperature. In the bottom panel, star symbols correspond to the fitting to the sum of internal energies of a three-dimensional isotropic harmonic oscillator and a free rigid rotor ((equations (9) and (10)).

Notably, quantum effects are non negligible for H_2 molecules in fullerene cages, even at room temperature. Indeed, quantum corrections amount to 14 % and 16 % of the total energy at T = 130 K in C_{24} and C_{28} cages, respectively, and their participation reduces down to 6 % and 7 % at T = 320 K.

Inside C_{60} and C_{70} fullerenes, hydrogen molecules remain bound to the cage below room temperature. At T = 130 K, the average adsorption energy is 1.8 kcal·mol^{-1} in the buckminsterfullerene, and 2.3 kcal·mol^{-1} in C_{70}. The binding energy monotonously decreases as temperature rises, which indicates a gradual deterioration of the hydrogen storage capacities of cage-like fused-ring carbon nanostructures within this temperature range.

As expected, the quantum correction to the total energy decrease with temperature. In C_{60}, this contribution reduces from 0.45 kcal·mol^{-1} at T = 130 K to 0.18 kcal·mol^{-1} at T = 320 K. In C_{70} fullerenes, it decreases from 0.19 kcal·mol^{-1} at T = 130 K down to 0.08 kcal·mol^{-1} at T = 320 K.

The computed total energies ⟨E⟩(T) of the H_2@C_{60} and H_2@C_{70} endohedral molecules are well reproduced by the sum of the internal energies of a three-dimensional isotropic harmonic oscillator and a rigid rotor (equations (9) and (10), respectively, see bottom panel in figure 4). The fitting scheme yields values ω = 404.2 K and 221.8 K for the energy spacing between translational energy levels in C_{60} and C_{70}, respectively. The deviation between the results of the fitting and previous experimental and theoretical evaluations of the fundamental vibrational frequency of H_2 centre of mass in these fullerenes are within 1 % and 15 % [10, 19–21]. This level of agreement is satisfactory, considering that the functional form employed in the fitting does not account for the anharmonicity and weak anisotropy of the confining potential, nor the coupling between orbital and rotational angular momenta, and that the results of previous experimental and theoretical calculations show notable variations [20].

IV. CONCLUSIONS

We report quasi-classical simulations of the translational and rotational dynamics of hydrogen molecules inside four quasi-spherical fullerene cages, namely C_{24}, C_{28}, C_{60}, and C_{70}. Energetic properties are computed from 130 K to 320 K, covering a sizable part of the temperature range of interest for storage technology applications.

The rise in temperature causes the average rotational and translational kinetic energies of embedded hydrogen molecules to increase (roughly) linearly. The energy spacing between adjacent low-lying rotational levels of the H_2 molecule in buckminsterfullerene and in C_{70} is comparable to or greater than k_BT, which causes deviations from the energy equipartition principle. Overall, the influence of quantum delocalization on energetic properties remains non-negligible over the entire range of thermodynamic conditions investigated here.

Novel materials featuring highly ordered and randomly packed assemblies of carbon nanocages have recently been synthesized and investigated with respect to their potential applications for energy storage and conversion [16]. The connection between the energetics of endohedral H_2@C_n molecules, and the hydrogen storage capacities of these carbon-based nanostructures is as follows.

In these materials, efficient hydrogen uptake can only be achieved if there are enough large pores. For these fullerenes, the H_2-surface interaction prevents adsorption. As it happens, the tight confinement imposed on the H_2 molecules by the smaller host structures (C_{24}, C_{28}) triggers marked quantum delocalization effects.

Nanocavities resembling C_{60} and C_{70} appear to be suitable hydrogen storage media, since hydrogen molecules remain bound to the cage for temperatures up to room temperature. The hydrogen storage capacities of C_{60}- and C_{70}-like nanocages will result from a trade-off between the higher binding energy of hydrogen to the host structure, and the possibility to accommodate more than one guest molecule per pore, owing to the smaller vibrational amplitude of H_2 translational motion in the cage.

Based on the present results, we plan in the future to extend the methodology to model hydrogen uptake by more complex nanomaterials (e.g., assemblies of carbon nanocages, metal- and covalent-organic frameworks) in the high-density regime

(i.e., by including several interacting H_2 molecules). In this perspective, the motion of host atoms may become relevant for more flexible nanoporous materials. Within the present approach, the inclusion of vibrations of host structure is straightforward. Work along this line is underway.

V. ACKNOWLEDGEMENTS

The results incorporated in this publication have received funding from the European Union's Horizon 2020 and Horizon Europe research and innovation programmes, under the Marie Skłodowska-Curie grant agreements n^{o}898663, and n^{o}101155733, respectively.

REFERENCES

[1] Q. Hassan, A. Z. Sameen, H. M. Salman, M. Jaszczur, and A. K. Al-Jiboory, *J. Energy Storage* **72**, 108404 (2023).

[2] H. Barthélemy, M. Weber, and F. Barbier, *Int. J. Hydrogen Energy* **42**, 7254 (2017).

[3] S. Satyapal, J. Petrovic, C. Read, G. Thomas, and G. Ordaz, *Catal. Today* **120**, 246 (2007).

[4] N. A. A. Rusman and M. Dahari, *Int. J. Hydrogen Energy* **41**, 12108 (2016).

[5] H. Shen, H. Li, Z. Yang, and C. Li, *Green Energy Environ.* **7**, 1161 (2022).

[6] M. Hirscher, A. Züttel, A. Borgschulte, and L. J. C. T. Schlapbach, (2009) Handbook of hydrogen storage. *Ceramic Transactions*, 202.

[7] M. Bastos-Neto, C. Patzschke, M. Lange, J. Möllmer, A. Möller, S. Fichtner, C. Schrage, D. Lässig, J. Lincke, R. Staudt, et al., *Energy Environ. Sci.* **5**, 8294 (2012).

[8] M. Mohan, V. K. Sharma, E. A. Kumar, and V. Gayathri, *Energy Storage* **1**, e35 (2019).

[9] A. Martínez-Mesa and G. Seifert, *Rev. Cubana Fis.* **31**, 32 (2014).

[10] Z. Bačić, *J. Chem. Phys.* **149**, 100901 (2018).

[11] N. S. Venkataramanan, H. Mizuseki, and Y. Kawazoe, *Nano* **4**, 253 (2009).

[12] J.-P. Hansen and I. R. McDonald, *Theory of Simple Liquids: With Applications to Soft Matter* (Academic Press, 2013).

[13] G. Bussi, D. Donadio, and M. Parrinello, *J. Chem. Phys.* **126**, 014101 (2007).

[14] T. Heine, L. Zhechkov, and G. Seifert, *Phys. Chem. Chem. Phys.* **6** (2004).

[15] G. B. Adams, M. O'Keefe, and R. S. Ruoff, *J. Phys. Chem.* **98** (1994).

[16] B. Rodríguez-Hernández, T. Nelson, N. Oldani, A. Martínez-Mesa, L. Uranga-Piña, Y. Segawa, S. Tretiak, K. Itami, and S. Fernandez-Alberti, *J. Phys. Chem. Lett.* **12**, 224 (2021).

[17] R. P. Feynman and A. R. Hibbs, *Quantum Mechanics and Path Integrals* (McGraw-Hill College, 1965).

[18] U. K. Deiters and R. J. Sadus, *J. Chem. Phys.* **158** (2023).

[19] M. Ge, U. Nagel, D. Hüvonen, T. Rõõm, S. Mamone, M. H. Levitt, M. Carravetta, Y. Murata, K. Komatsu, J. Y.-C. Chen, and N. J. Turro, *J. Chem. Phys.* **134** (2011).

[20] M. Xu, F. Sebastianelli, Z. Bačić, R. Lawler, and N. J. Turro, *J. Chem. Phys.* **129** (2008).

[21] F. Sebastianelli, M. Xu, Z. Bačić, R. Lawler, and N. J. Turro, *J. Am. Chem. Soc.* **132** (2010).

[22] M. Capitelli, G. Colonna, and A. D'Angola, *Fundamental Aspects of Plasma Chemical Physics: Thermodynamics* (Springer Science, 2012).

[23] R. Rodríguez-Cantano, R. Pérez de Tudela, M. Bartolomei, M. I. Hernández, J. Campos-Martínez, T. González-Lezana, P. Villarreal, J. Hernández-Rojas, and J. Bretón, *J. Phys. Chem. A* **120**, 034302 (2016).

[24] O. Elafifi, N. Tchouar, K. Ouadah, and M. Arab Ait Tayeb, *Int. J. Mod. Phys. B* **38**, 2450296 (2024).

[25] S. Patchkovskii and T. Heine, *Phys. Chem. Chem. Phys.* **9**, 2697 (2007).

PARTICLE FLUENCE ESTIMATION FOR SAMPLES IRRADIATED AT A LONG-TERM EXPOSURE STATION (NICA COMPLEX, DUBNA)

ESTIMACIÓN DE LA FLUENCIA DE PARTÍCULAS PARA MUESTRAS IRRADIADAS EN UNA ESTACIÓN DE EXPOSICIÓN PROLONGADA (COMPLEJO NICA, DUBNA)

M. Pérez-Tápanez[a†], N. Pukhaeva[b,c], N.Zamiatin[b], O. Díaz [a†], D. Chemezov[b]

a) Higher Institute for Applied Sciences and Technology at Havana University, Havana, Cuba.marcela.perez@instec.cu; odrizo@instec.cu†
b) Joint Institute for Nuclear Research, Dubna, Russia.
c) North-Ositian State University, Vladikavkaz, Russia.
† corresponding author

Recibido 20/1/2025; Aceptado 30/5/2025

The prototype of the Target Station for Long-Term Exposure was assembled after all detectors of BM@N Experiment. During collection of the physical data with the $^{124}Xe_{54}$ beam of 3.8 GeV kinetic energy at BM@N, different samples were irradiated. Data was analyzed for precise determination of the intensity, the fluence and the absorbed dose for irradiated materials. The beam intensity and profile distributions were determined for each sample. From the obtained intensity, the fluence was calculated for each irradiated sample. Then, the absorbed dose of irradiated materials was be calculated. The study was performed within the ARIADNA Collaboration.

El prototipo de la Estación de Objetivos para Exposición a Largo Plazo fue desplegado al final de la línea de detectores del experimento BM@N. Fueron irradiadas diferentes muestras en el BM@N durante la recopilación física de datos con el haz de iones de $^{124}Xe_{54}$,de energía cinética de 3.8 GeV. Los datos fueron analizados para la determinación precisa de la intensidad, para la estimación de la fluencia y la dosis absorbida de los materiales irradiados. Para cada muestra fueron determinados la intensidad y el perfil del haz. La fluencia fue calculada a partir de la intensidad obtenida para cada muestra. Luego, se calcula la dosis absorbida por los materiales irradiados. Este estudio es llevado a cabo como parte de la Colaboración ARIADNA.

Keywords: fluence (fluencia), absorbed dose (dosis absorbida), high energy ion beam (haz de iones de alta energía), irradiated samples (muestras irradiadas).

I. INTRODUCTION

The **N**uclotron-based **I**on **C**ollider f**A**cility (NICA) is an accelerator complex that is under construction at the Joint Institute for Nuclear Research in Dubna, Russian Federation. The main purpose of NICA is to study the properties of dense baryonic matter [1]. BM@N (Baryonic Matter at Nuclotron) is the first experiment undertaken at the NICA-Nuclotron accelerator complex. Its goal is the study of heavy-ion beams interactions with fixed targets. The beam, extracted from the Nuclotron, is transported to the BM@N experimental installation. Only a 2 % of the beam interacts with the target, and it was decided to use it for applied research. Recently, after the Forward Hadron Calorimeter [2], a new Station for Long-Term Exposure (SLTE) was assembled, which is after all detectors of the BM@N experiment. This station is devoted to the irradiation of samples for applied research. The rest of the beam at the LTE station, in parallel with the operation of the BM@N set-up [3], is used for applied studies of samples of different geometry and chemical composition. Previously, some analyzes were carried out in order to determine the radiation intensity and the profile of the irradiated samples, based on the information from each of the detectors associated with the BM@N experiment [3]. This study was necessary because the samples would be set after the BM@N detector array. Finally, the integral intensity or the total number of ions passing through the samples was estimated [3].

II. MATERIALS AND METHODS.

II.1. Experimental Data Collection.

In order to estimate the fluence, it is necessary to measure the beam intensity and to determine the physical parameters of each detector located in the beam line. During the Xe beam run [3], Veto Counter (VC) registered a 80 % of the beam. In order to minimize the interactions upstream of the target, the scintillators and active parts of the Si detectors were located in vacuum, while the photomultiplier tubes (PMTs) of the scintillation counters and the front-end electronics of the silicon detectors were kept in air, with their housings mounted on the flanges of the beam pipe. In order to reject the beam halo, the beam aperture was limited by the 25 mm diameter hole in the scintillation counter (VC). Independently, the beam ions or expected fragments can be detected by a 4 mm thick quartz hodoscope (FQH), located in front of the beam hole. Information from the hodoscope is used in outline analysis for event selection and determination of event centrality.

II.2. Computer Analysis.

All data were written on an e-Log platform from the number of runs for each corresponding data. Initially, data are written in binary format, and then digitized to Root format. Information

about the bean profile is written as DST.exp files for each run. By analyzing these files, a miniDST file is created to keep all necessary information [4]. BmnRoot software [3] was used for the information processing.

II.3. Dosimetrical Analysis.

The *absorbed dose* (D) is a measure of the effect caused by radiation on materials. It is relevant to all types of ionizing radiation fields (directly or indirectly), as well as to any ionizing radiation source distributed within the absorbing medium. It is defined as:

$$D = \frac{d\varepsilon}{dm} \tag{1}$$

where, $d\varepsilon$ is the expected energy value of a particle impacted by finite volume V, and dm is the mass differential [5].

The fluence of particles (ϕ), in dosimetric studies, is a measure of the number of ionizing particles that arrive at the detector surface in a given time. It is defined as:

$$\phi = \frac{dN}{dA} \tag{2}$$

where, N is the number of particles (nucleons) that arrive at the area, and A is the surface area (cm^2). It is an important parameter, because it is used to estimate the *absorbed dose*. Therefore, the unit of measurement for fluence is the particles per square centimeter [5].

For charged particles, it is possible to obtain the *absorbed dose* value from the fluence, if the target thickness is a few percent or less of the range. Then, the energy lost in collision interactions for a fluence ϕ (charged particles$\cdot cm^{-2}$) of energy will be:

$$E = \phi\left(\frac{dT}{\rho dx}\right)\rho x \tag{3}$$

where, $dT/\rho dx$ is the collision stopping power of the foil mass, and the density thickness (ρt), is the length of the particle path through the foil. Hence, the absorbed dose in the foil can be estimated as

$$D = \phi\frac{\left(\frac{dT}{\rho dx}\right)\rho x}{\rho x} = \phi\left(\frac{dT}{\rho dx}\right) \tag{4}$$

where, the foil thickness ρx must be canceled, leaving the dose as a product of fluence and mass collision stopping power. This cancellation is very important, taking into account that the dose in the foil, does not depend at the thickness [5].

II.4. Irradiated samples.

Before the experiment, scientific and methodological tasks were selected to establish the main parameters of the beam and irradiation schemes for each type of sample [6].

Different tasks were related to the study of protective properties, radiation resistance, and radio modification of composite materials for the space industry, developed and produced at V. G. Shukhov Belgorod State Technological University (BSTU) [6]. It is also of interest in some research related to support, for spacecraft crews, in the study of the effect induced by heavy ions on seed germination and plant development features. In that sense, the structural modification and state of matter as a result of the action of accelerated ion beams on artificial sapphires (Al_2O_3) is studied.

Furthermore, radiation damage of thin polymer films (up to 100 μm thick) films, based in polytetrafluoroethylene (PTFE) and thermo-radiationally modified PTFE, polyethylene terephthalate, polyimides, and the irradiation of high-temperature superconducting tapes (1st and 2nd generation), produced by JSC "S-Innovations" (Moscow) [6], was also studied during the experiment.

The program also includes the study of the effects induced by the irradiation of targets of some metals, and measurement of the induced activity. In particular, the isotopes ^{7}Be, ^{22}Na and ^{24}Na, in the spectra of the aluminum-irradiated targets [6].

III. RESULTS AND DISCUSSION

III.1. Fluence estimation.

To determine the *fluence*, it is necessary to know the dimensions of the incident beam and the irradiated sample, as well as the coordinates where the sample is located. To achieve it, it was assumed that the sample was located just in the center of the ion beam and also that nucleons, in the beam, are distributed homogeneously. The geometry of the beam sample is presented in Figure 1.

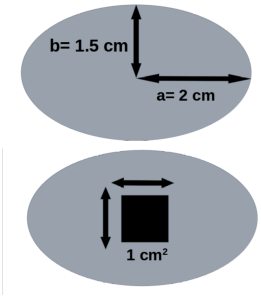

Figure 1. Bean-sample geometry. Top panel: geometric representation of the ion beam, including the dimensions of the surface radius a and b. Bottom panel: location of the sample, respect to the beam, its geometric representation and area [7]).

The shape of the beam has been approximated as an ellipse, whose radii a and b have values of 2 cm and 1.5 cm, respectively. The ellipse area represents the surface of the beam. It was calculated as follows:

$$A = \pi \cdot a \cdot b \tag{5}$$

resulting in a value of 9.4248 cm^2, and the sample has a squared shape with an area of 1 cm^2. The beam intensity was

obtained by reading the results ejected by the FQH detector at the end of the beam line [6]. This value represents the total number of nucleons transported by it [6].

To determine the number of nucleons affected in the sample, we divided the total number of nucleons by the area of the ellipse. That shows how many nucleons are found in a unit of area, and then this result must be multiplied by the area defined by the sample. This value represents the fluence of the particles in the area of interest (da), introduced in the equation (2). The approximate value of the deposited energy was also estimated, knowing that the $^{124}Xe_{54}$ beam has an energy of 3.8 GeV · nucleon^{-1}. This energy is multiplied by the number of incident nucleons on the sample area (ϕ). Finally, the total number of measured nucleons and the fluence calculated for each sample are shown in Table 1.

Table 1. Measured intensity, fluence (nucleons·cm^{-2}), and energy distribution (GeV · cm^{-2}) for each of the samples. [7]

Samples	Intensity	Fluence	Energy distribution
Seed I	2.42622e+08	6.4e+06	2.43e+07
Seed II	2.47850e+08	6.6e+06	2.51e+07
Seed III	3.46815e+08	9.2e+06	3.50e+07
Seed IV	2.24907e+08	6.6e+06	6.6e+06
Sapphire + Films + Al	5.79354e+09	1.5e+08	5.7e+08
Add composite ROCC + VTSP(1)	4.86455e+09	1.3e+08	4.94e+08
Add composite MCS + VTSP(2)	2.39928e+09	6.4e+07	2.43e+08

III.2. Uncertainty sources.

The first source of uncertainty comes from the fact that, between the sample and the FHQ hodoscope, there is a distance of 2 meters in air [3]. Therefore, when the ion beam crosses that distance, traveling from one point to another, it is possible that there are interactions, deviations, and/or energy loss that were not measured. The last causes the 100 % of the real intensity of the radiation to not be recorded. The second source of uncertainty is that we have considered that the nucleons throughout the beam are distributed homogeneously [8], in an elliptical geometry. This is an approximation, since, in reality, the nucleons tend to concentrate at the center of the beam, as shown in Figure 2.

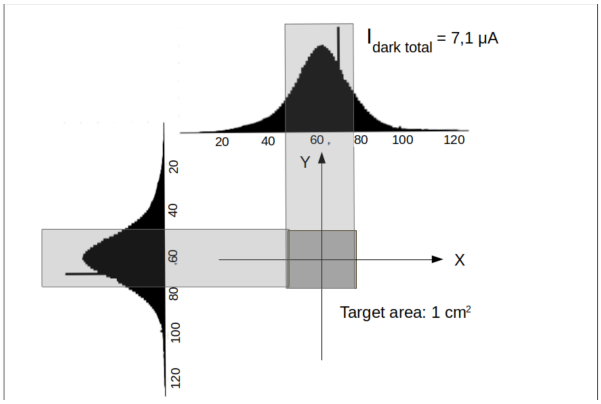

Figure 2. Gaussian intensity distribution and sample position [7]

IV. CONCLUSION

The particle fluence of the analysis of beam data that was taken during physical data collection with the ^{124}Xe beam of the 3.8 A GeV kinetic energy at the BM@N installation in the 8th Commissioning Run of the NICA Complex was calculated. This is the first experiment of irradiation of different samples for applied research in the LTE Station with high energy ions. The uncertainties of the results were analyzed to improve the precision of the calculations. Further studies are in progress to compare the parameters obtained by Monte Carlo simulations.

V. ACKNOWLEDGMENTS

The present research was supported by the Russian State Funding Program, FEFN-2024-006.

REFERENCES

[1] Nuclotron Based Ion Collider fAcility (s.f.). Joint Institute for Nuclear Research. `https://nica.jinr.ru`

[2] Nuclotron Based Ion Collider fAcility (s.f.). Baryonic Matter at Nuclotron (BM@N). Joint Institute for Nuclear Research. `https://nica.jinr.ru/ru/projects/bman.php`

[3] N. Pukhaeva, O. Belov, S. Tyutyunnikov, *Analysis of beam intensity data for determination of absorbed dose to solid materials for high-energy ion beams.* [Conference], International Seminar on Interactions of Neutrons with Nuclei, El-Sheikh, Egypt (2024, April 14th-18th). `http://isinn.jinr.ru/index.html`

[4] Official BM@N collaboration website (s.f.). DAQ Computing Center of the BM@N Experiment. Joint Institute for Nuclear Research. `https://bmn.jinr.ru/bmn-daq-computing-center`

[5] F.H. Attix, VI Quantities and Units for Use in Radiation Protection, *Introduction to Radiological Physics and Radiation Dosimetry*, WILEY-VCH Verlag GmbH & Co. KgaA (Ed.) (2004).

[6] First applied research with high-energy ion beams of the NICA Complex (s.f.). Joint Institute for Nuclear Research. https://www.jinr.ru/posts/first-applied-research-with-high-energy-ion-beams-of-the-nica-complex

[7] M. Pérez Tápanes, Student Report for START Program (2024). https://students.jinr.ru/uploads/report_files/report_student_2268_project_413.pdf

[8] N.I. Zamiatin, *Analysis of the operation of coordinate systems based on Si-detectors, information on radiation damage.* (2023). https://indico.jinr.ru/event/3531/timetable/#20230516.detailed

METAL-INSULATOR TRANSITION DESCRIBED BY NOFT

TRANSICIÓN METAL-AISLANTE DESCRITA POR LA TFON

J. F. H. Lew-Yee[a†], M. Piris[a,b,c†]

a) Donostia International Physics Center (DIPC), 20018 Donostia, Spain. felipe.lew.yee@dipc.org†
b) Kimika Fakultatea, Euskal Herriko Unibertsitatea (UPV/EHU), 20018 Donostia, Spain. mario.piris@ehu.eus†
c) IKERBASQUE, Basque Foundation for Science, 48009 Bilbao, Spain.
† corresponding author

Recibido 16/4/2025; Aceptado 16/6/2025

The metal–insulator transition (MIT) is a fundamental phenomenon in condensed matter physics and a hallmark of strong electronic correlations. Hydrogen-based systems offer a simple yet powerful model for investigating the MIT, as their insulating behavior arises purely from electron–electron interactions. In this work, we study finite hydrogen clusters with cubic geometries using Natural Orbital Functional Theory (NOFT), a method capable of accurately describing correlated systems beyond mean-field approaches. We focus on two key signatures of the MIT: the fundamental energy gap and the harmonic average of the atomic one-particle reduced density matrix. Our results show that NOFT captures the transition from insulating to metallic behavior as the interatomic distance decreases. By extrapolating the energy gap to the thermodynamic limit, we estimate a critical distance $r_c \approx 1,2$Å, in excellent agreement with quantum Monte Carlo benchmarks. These findings demonstrate the reliability of NOFT for describing strong correlation effects in large-scale models.

La transición metal–aislante (TMA) es un fenómeno fundamental en física de la materia condensada y una manifestación característica de las correlaciones electrónicas fuertes. Los sistemas basados en hidrógeno constituyen un modelo simple pero eficaz para estudiar la TMA, ya que su comportamiento aislante se debe exclusivamente a interacciones electrón–electrón. En este trabajo, investigamos cúmulos finitos de hidrógeno con geometría cúbica mediante la Teoría del Funcional de Orbitales Naturales (TFON), un método capaz de describir con precisión sistemas correlacionados más allá del campo medio. Nos centramos en dos indicadores clave de la TMA: la brecha de energía fundamental y el promedio armónico de la matriz densidad uniparticular atómica. Nuestros resultados muestran que la TFON reproduce con éxito la transición del estado aislante al metálico al disminuir la distancia interatómica. Al extrapolar la brecha al límite termodinámico, estimamos una distancia crítica $r_c \approx 1,2$Å, en excelente concordancia con estudios de Monte Carlo cuántico.

Keywords: Metal–Insulator Transition (transición metal-aislante); Strongly Correlated Electrons (electrones fuertemente corrlecionados); Reduced Density Matrix (matriz de densidad reducida); Functional Theory (teoría funcional); Natural Orbitals (orbitales naturales).

I. INTRODUCTION

The metal–insulator transition (MIT) [1] is a central concept in condensed matter physics and one of the most compelling manifestations of electron correlation effects in solids. In these transitions, materials change their electronic phase from conducting to insulating or vice versa under the influence of external parameters such as temperature, pressure, doping level, or lattice strain. While the transition may appear continuous or abrupt depending on the system, it generally reflects a subtle interplay between electron localization and delocalization. These phenomena are not only of fundamental theoretical interest but also of increasing technological relevance due to their potential integration into future microelectronic, sensing, and switching devices [2]. Materials exhibiting MIT behavior are therefore highly valued in the search for controllable, multifunctional components for next-generation electronics [3, 4].

A historically significant and conceptually rich subclass of MIT materials are Mott insulators, whose study began in 1937 [5] during a conference chaired by Sir Nevill Mott. At the time, transition-metal oxides such as NiO, MnO, and Fe_2O_3 were observed to behave as insulators despite having partially filled 3d electronic bands, which, according to conventional band theory, should result in metallic behavior. Building on the insights of de Boer, Verwey, and Peierls, Mott argued that this insulating behavior was caused by strong onsite Coulomb repulsion, which localized electrons and suppressed conduction even in the absence of a filled band. This challenged the established Bloch-Wilson picture and gave rise to the concept of the Mott transition, where electron–electron interactions, rather than band filling, govern the electronic phase of the system [6].

Contemporary research continues to explore MITs across a wide range of materials and dimensionalities [7, 8]. In particular, two-dimensional crystals with specific lattice geometries have recently demonstrated that even moderate interactions can induce Mott insulating behavior [9]. These findings highlight the universality of the MIT in systems with diverse chemical compositions, dimensionalities, and electronic structures. They also underscore the need for accurate theoretical models capable of capturing the essential physics of strong correlation. In this context, idealized systems composed of hydrogen atoms under extreme conditions offer a unique platform to isolate and study the fundamental ingredients that govern MIT phenomena [10–12].

Among idealized systems, a simple lattice of hydrogen atoms offers a particularly clear framework for illustrating

the essential mechanism of a Mott transition in its most fundamental form [13–15]. At large interatomic distances, each hydrogen atom behaves as an isolated unit, with one electron localized at each site. Exciting the system into a conducting state requires transferring an electron from its original site to a distant one, which is energetically penalized by the difference between the ionization potential and the electron affinity, known as the fundamental energy gap. This difference defines an effective Coulomb repulsion energy, usually denoted as U. As the lattice spacing decreases, the overlap between electronic wavefunctions increases, broadening the energy levels by a bandwidth W. The system becomes metallic when the kinetic energy gain associated with delocalization overcomes the Coulomb repulsion, which leads to a critical transition governed by the ratio U to W. This framework is now a cornerstone in the theoretical understanding of many-body systems that display correlated insulating and metallic phases.

While the hydrogen lattice provides an idealized but physically transparent model to explore the fundamental mechanism of the Mott MIT, accurately capturing its electronic properties remains a significant theoretical challenge. Traditional ground-state density functional theory [16, 17], despite its success in weakly correlated systems, fails to describe the insulating behavior of strongly correlated materials in the absence of explicit symmetry breaking [18], as evidenced in well-known cases such as transition metal oxides. Even advanced many-body approaches like the GW approximation often do not predict insulating states unless long-range magnetic order is imposed [19, 20]. In contrast, methods that explicitly incorporate many-body correlation effects, such as dynamical mean field theory [21, 22] and natural orbital functional (NOF) theory (NOFT) [23, 24], have been shown to correctly capture insulating phases without invoking long range spin order [25, 26]. This capability is particularly relevant in model hydrogen systems, where electron correlation alone drives localization. Within this context, NOFT offers a promising framework to study finite hydrogen clusters as minimal yet nontrivial systems for understanding the MIT. In the present work, we employ NOFT to investigate signatures of the MIT in hydrogen cubes, focusing on the fundamental energy gap and the harmonic average of the atomic one-particle reduced density matrix (1RDM) as key indicators, in order to highlight the role of electronic correlation beyond mean-field approximations.

This article is organized as follows. First, we introduce the key concepts of NOFT, along with the electron-pairing-based approximations used throughout this work. Next, the computational methodology is presented, followed by a discussion of the results. The article closes with a summary of the main findings

II. NATURAL ORBITAL FUNCTIONAL THEORY

NOFT is the formulation of the 1RDM functional theory [27–30] in the natural orbital (NO) representation [31]. It offers a computationally efficient alternative [32] to conventional wavefunction-based methods, which often exhibit steep scaling. By using the 1RDM as the central variable and reconstructing the two-particle reduced density matrix (2RDM) through well-founded approximations, NOFT allows for an accurate description of strongly correlated electronic states, showing particular robustness in multireference regimes [33–40]. In this framework, the ground-state energy is expressed as a functional of the NOs and their occupation numbers (ONs), which are variationally optimized. The presence of significantly fractional ONs reveals a multiconfigurational character, a regime traditionally addressed by methods such as CASPT2 [41]. However, these approaches require active space selection and become computationally expensive as the number of correlated orbitals increases. In contrast, NOFT correlates all electrons in all orbitals within the chosen basis set, avoiding the need to define an active space and eliminating arbitrary user choices. This makes NOFT particularly suitable for processes such as bond breaking and formation [42], where the optimal active space is not known a priori, while also offering greater accessibility for non-expert users.

In recent years, NOFT has undergone significant progress from both theoretical and computational perspectives [43–45]. A notable result of this progress is the family of Piris NOFs (PNOFs) [46–48], which have consistently demonstrated competitiveness with standard electronic structure methods. These functionals have shown effectiveness across a wide range of applications [49–51], including the description of excited states [52], molecular dynamics simulations [53], and the mitigation of delocalization errors [54]. More recently, NOFs have been incorporated into quantum computing frameworks to enhance energy estimation efficiency within the variational quantum eigensolver (VQE) algorithm, resulting in the development of a NOF-VQE [55]. On the computational side, recent advances [56–58] have considerably reduced the cost of NOF calculations. A key improvement has been the integration of modern numerical techniques inspired by deep learning, particularly momentum-based optimization methods, which have significantly accelerated convergence [58]. These developments have enabled NOFT to treat strongly correlated systems efficiently, establishing it as a practical tool for large-scale applications.

The ground-state energy of a NOF is expressed in terms of the set of NOs $\{\phi_i\}$ and their ONs $\{n_i\}$ as

$$E[\mathrm{N}, \{n_i, \phi_i\}] = \sum_i n_i H_{ii} + \sum_{ijkl} D[n_i, n_j, n_k, n_l]\langle ij|kl\rangle \tag{1}$$

where the one- and two-electron integrals are given by

$$H_{ii} = \int d\mathbf{r}\phi_i^*(\mathbf{r})\left(-\frac{\nabla_r^2}{2} + v(\mathbf{r})\right)\phi_i(\mathbf{r}) \tag{2}$$

$$\langle ij|kl\rangle = \int\int d\mathbf{r}_1 d\mathbf{r}_2 \frac{\phi_i^*(\mathbf{r}_1)\phi_j^*(\mathbf{r}_2)\phi_k(\mathbf{r}_1)\phi_l(\mathbf{r}_2)}{|\mathbf{r}_2 - \mathbf{r}_1|} \tag{3}$$

In Eq. (2), $v(\mathbf{r})$ represents the nuclear potential derived from the molecular geometry within the Born–Oppenheimer approximation, assuming no external fields. The exact form of the electron–electron interaction energy functional is unknown, and different functional forms of $D[n_i, n_j, n_k, n_l]$ define distinct NOFs.

The approximate functional in Eq. (1) explicitly depends on the 2RDM, requiring not only the N-representability of the 1RDM [59] but also that of the functional itself [60]. Specifically, the reconstructed $D[n_i, n_j, n_k, n_l]$ must satisfy the same N-representability conditions as an unreconstructed 2RDM [61], in order to ensure the existence of a compatible N-electron system. Different reconstructions of D under these constraints have given rise to the various PNOFs.

In this work, we focus on electron-pairing-based PNOFs [62]. Accordingly, we consider N_I unpaired electrons, which determine the system's total spin S, while the remaining $N_{II} = N - N_I$ electrons form pairs with opposite spins, resulting in zero net spin contribution from the paired electrons. Within the spin-restricted formalism, all spatial orbitals φ_p are doubly occupied in the ensemble, and the ONs of both spin components are equal [63]. Following the partitioning of electrons into N_I and N_{II}, the orbital space Ω is divided into two subspaces: $\Omega = \Omega_I \oplus \Omega_{II}$. The subspace Ω_{II} consists of $N_{II}/2$ mutually disjoint subspaces Ω_g, each containing a reference orbital $|g\rangle$ for $g \leq N_{II}/2$, along with N_g associated orbitals $|p\rangle$ for $p \geq N_{II}/2$. Taking spin into account, the total occupancy of each subspace Ω_g is equal to 2. Similarly, Ω_I is composed of N_I mutually disjoint subspaces; however, each $\Omega_g \in \Omega_I$ contains only a single orbital g with $n_g = 1/2$, corresponding to one unpaired electron whose spin state remains unspecified. It follows that the trace of the 1RDM equals the total number of electrons N.

This study focuses on finite hydrogen clusters, for which PNOF7 [47, 64] is employed. Previous studies have demonstrated that PNOF7 accurately reproduces the potential energy curves of such systems in smaller-scale cases [37,38]. In particular, it captures the correct physical behavior in both the bonding and dissociation regimes, yielding stable and reliable dissociation energies.

The energy expression for PNOF7 is given by

$$E\left[\mathrm{N}, \{n_p, \varphi_p\}\right] = E^{\mathrm{intra}} + E^{\mathrm{inter}} \tag{4}$$

The intra-pair component is formed by summing the energies E_g of electron pairs with opposite spins and the single-electron energies of unpaired electrons, specifically:

$$E^{\mathrm{intra}} = \sum_{g=1}^{N_{II}/2} E_g + \sum_{g=N_{II}/2+1}^{N_{II}/2+N_I} H_{gg} \tag{5}$$

$$E_g = 2\sum_{p\in\Omega_g} n_p H_{pp} + \sum_{q,p\in\Omega_g} \Pi(n_q, n_p) L_{pq} \tag{6}$$

Here, $L_{pq} = \langle pp|qq\rangle$ are the exchange-time-inversion integrals [65]. The matrix elements $\Pi(n_q, n_p) = c(n_q)c(n_p)$, where $c(n_p)$ is defined by the square root of the ONs as follows:

$$c(n_p) = \begin{cases} \sqrt{n_p}, & p \leq N_{II}/2 \\ -\sqrt{n_p}, & p > N_{II}/2 + N_I \end{cases} \tag{7}$$

The inter-subspace term is given by

$$E^{\mathrm{inter}} = {\sum_{p,q=1}^{N_B}}' \{n_q n_p \left(2J_{pq} - K_{pq}\right) - \Phi_q \Phi_p L_{pq}\} \tag{8}$$

where $J_{pq} = \langle pq|pq\rangle$ and $K_{pq} = \langle pq|qp\rangle$ are the Coulomb and exchange integrals, respectively. The term $\Phi_p = \sqrt{n_p h_p}$, with $h_p = 1 - n_p$, defines a correlation factor that becomes significant when the ON n_p deviates from 0 or 1. N_B denotes the number of basis functions considered. The prime in the summation indicates that only inter-subspace terms are included. Notably, PNOF7 introduces inter-pair static electron correlation, as Φ_p increases in regions where orbitals exhibit strong multiconfigurational character [64].

III. METHODOLOGY

The transition from a metallic to an insulating phase is generally associated with either a structural reorganization or a mechanism driven by the electron correlation. In this work, we focus on the latter, which underlies the MITs observed in hydrogen clusters. As the interatomic distance increases, the overlap between atomic orbitals responsible for conduction decreases, resulting in a reduced bandwidth. In systems with strong electron correlation, this reduction can lead to a Mott transition, where Coulomb repulsion dominates over delocalization, ultimately opening an energy gap. A critical distance exists beyond which electronic overlap becomes insufficient to sustain metallic behavior, signaling the onset of insulating character. This concept forms the basis for a first estimation of the critical interatomic distance, r_c, derived from the balance between Coulomb interaction and electronic delocalization.

An estimate of r_c can be obtained from fundamental physical arguments. The distance at which Coulomb interaction dominates over delocalization can be interpreted through the Heisenberg uncertainty principle ($\Delta p \Delta r \sim \hbar$). For an electron confined to a region of size r_c, the characteristic momentum is $\Delta p \sim \hbar/r_c$, yielding a kinetic energy of $E_k \sim (\Delta p)^2/2m \sim \hbar^2/2mr_c^2$, while the Coulomb potential energy between two electrons at distance r_c is $E_p = e^2/4\pi\epsilon_0 r_c$. The transition occurs when Coulomb repulsion becomes significantly larger than the kinetic energy, which we assume as $E_p = 10 \cdot E_k$. Solving this condition for r_c gives $r_c = 5a_0 = 2.65$ Å. This value is close to the estimate obtained by assuming a homogeneous electron gas with a critical density $n_c \sim 0.01\ a_0^{-3}$; using the relation $n_c \sim r_c^{-3}$, one obtains $r_c \sim 4.64a_0 \sim 2.45$ Å. However, studies on hydrogen chains and clusters show that the transition occurs at shorter distances. A diffusion quantum Monte Carlo study [13] benchmarks the transition between paramagnetic and antiferromagnetic body-centered cubic atomic hydrogen

in its ground state, reporting a second-order metal–insulator transition at $r_c = 2.27a_0 = 1.2$ Å.

The most rigorous way to define the MIT is by identifying the opening of a gap in the density of states at the Fermi level. However, this criterion is not directly applicable to finite clusters, which inherently exhibit a discretized spectrum. Nevertheless, the transition can still be located as the point where the fundamental energy gap surpasses the effects of finite-size discretization. Since this discretization error is not known a priori, we adopt a finite-size scaling approach in which it is accounted for by extrapolating the fundamental gap, defined as $\delta = E(\mathrm{N}+1) + E(\mathrm{N}-1) - 2E(\mathrm{N})$, to the thermodynamic limit ($\mathrm{N} \to \infty$). To this end, we compute δ for hydrogen cubes of increasing size and for a set of interatomic distances r. The resulting $\delta(\mathrm{N})$ values are fitted as a function of N using a decaying polynomial model:

$$\delta(\mathrm{N}) = \delta_\infty + \frac{A}{\mathrm{N}^p} \tag{9}$$

where δ_∞ is the extrapolated gap in the infinite system, A and p are fitting parameters, and N is the number of electrons in the system. The MIT is then identified as the point where δ_∞ becomes nonzero, indicating the emergence of an insulating phase in the thermodynamic limit.

IV. RESULTS

We begin our analysis by examining the symmetric dissociation of a large hydrogen cluster consisting of 512 atoms arranged in a cubic structure ($8\times8\times8$). All calculations were performed using the DoNOF software package [56] with the 6-31G basis set [66] and the def2-universal-jkfit auxiliary basis set, employing real orbitals within a spin-restricted framework. The perfect pairing scheme ($\mathrm{N}g = 1$) is used, as it is the highest pairing allowed by the negatively charged system. This leads to a fully correlated treatment of 512 electrons distributed over 512 spatial orbitals, making it a highly demanding electronic structure calculation.

Each configuration was defined by uniformly setting the interatomic distance between the nearest neighbours, resulting in a series of hydrogen cubes that span from a delocalised metallic regime to a localised insulating one. In the dissociation limit, the system becomes a collection of 512 non-interacting hydrogen atoms. Importantly, the correlation effects in the hydrogen cube involve all electrons equally, posing a significant challenge for electronic structure methods. To contextualise our results, we refer to a representative set of Quantum Monte Carlo studies on hydrogen systems [12–15], highlighting the broader relevance of our work within the field.

Fig. 1 presents the total electronic energy as a function of the interatomic distance r for hydrogen cubes with 512 atoms. The results obtained with PNOF7 (red) and restricted Hartree–Fock (HF, black) are shown for comparison. The PNOF7 curve exhibits a clear minimum around $r \approx 1.6$ Å. As the distance increases beyond this point, the energy gradually stabilizes, reflecting the transition toward the dissociated insulating state. In contrast, HF significantly overestimates the total energy across the entire range and fails to capture the energetic stabilization associated with electron correlation, particularly in the strongly correlated regime.

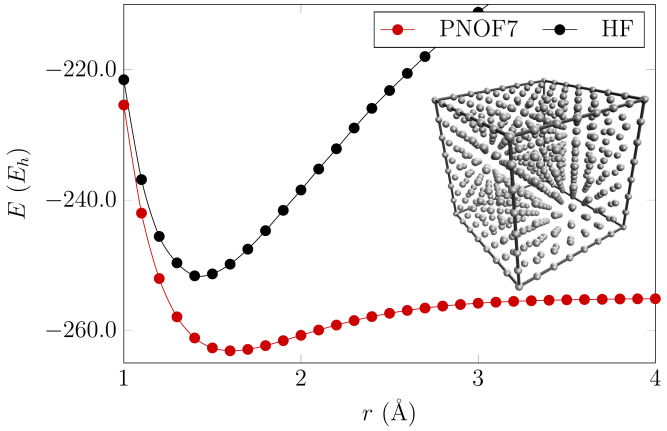

Figure 1. Potential energy curves for the symmetric dissociation of hydrogen cubes with 512 atoms.

To quantitatively describe the MIT, we computed the harmonic average γ of all off-diagonal elements $\Gamma^{\mathrm{ao}}_{\mu\nu}$ of the 1RDM on the atomic orbital basis. In this regard, we generalized the definition on Ref. [67] to count only interatomic elements as follow:

$$\gamma = \sqrt{\frac{1}{\mathrm{N}_B\,(\mathrm{N}_B-2)} \sum_{\substack{\mu\in A,\ \nu\in B \\ A\neq B}} (\Gamma^{ao}_{\mu\nu})^2} \tag{10}$$

where the summation indices indicate the selection of the components associated with the atomic orbital ϕ_μ on atom A and ϕ_ν on atom B, while omitting the elements related to atomic orbitals on the same atom. Specifically, for the 6-31G base set used here, which contains two atomic orbitals per hydrogen atom, this means excluding the diagonal blocks 2×2. Consequently, $\mathrm{N}_B\,(\mathrm{N}_B-2)$ denotes the complete count of elements in the summation, although we note that the denominator depends on the number of atomic orbitals centered on each atom. Å

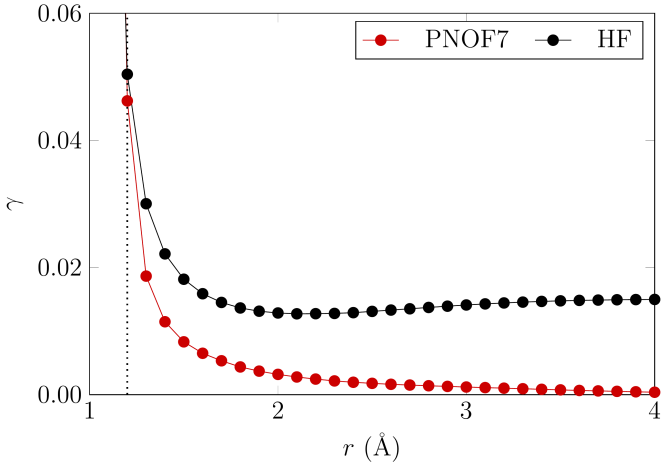

Figure 2. Harmonic average γ of the off-diagonal elements of Γ^{ao}. The critical distance (r_c) for the metal-to-insulator transition is indicated by a vertical dotted line.

Fig. 2 shows the evolution of this quantitative indicator of electronic delocalization. In the PNOF7 results (red), γ decreases rapidly as the interatomic distance increases, signaling a transition from a delocalized metallic phase to a localized insulating phase. This behavior is consistent with the expected suppression of spatial coherence: as electrons localize, the off-diagonal elements $\Gamma^{ao}_{\mu\nu}$ tend toward zero, leading to a harmonic average that vanishes in the insulating limit. In contrast, HF results (black) exhibit a much slower decay and eventual saturation of γ, failing to capture the correlation-driven localization process.

The value $r_c \approx 1.2$ Å, is the estimated critical distance for the MIT, obtained using the finite-size scaling approach. The fundamental energy gap obtained δ(N) for hydrogen cubes of various sizes, ranging from N = 8 ($2\times2\times2$) to N = 512 ($8\times8\times8$), and for a set of interatomic distances r are shown in Fig. 3.

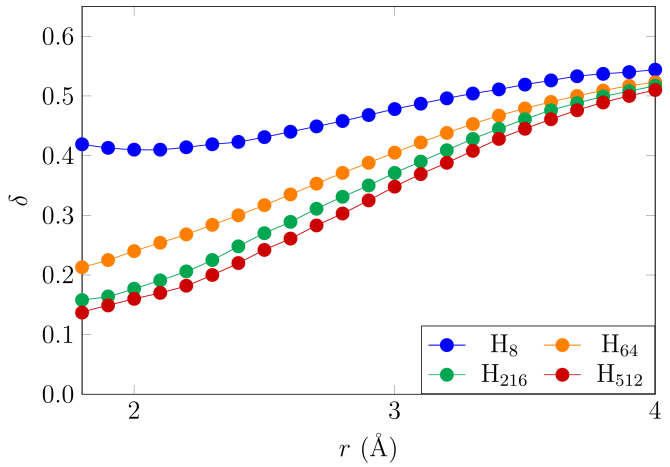

Figure 3. Fundamental energy gap for hydrogen cubes of various sizes.

The resulting values of δ(N) were fitted as a function of N using the decaying polynomial form of Eq. 9, as illustrated in Fig. 4.

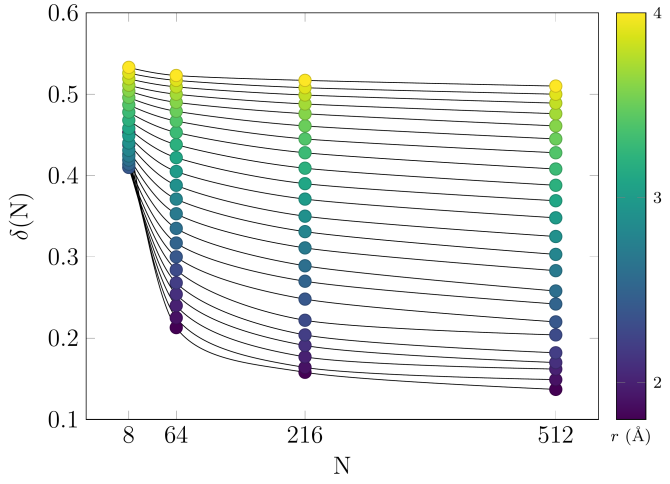

Figure 4. Fundamental energy gap δ(N) as a function of system size N for hydrogen cubes at various interatomic distances r, color-coded as indicated by the color bar on the right. The data points correspond to calculated values, and the lines represent the fits using the decaying polynomial model of Eq. 9.

Each curve corresponds to a different interatomic distance r, color coded from purple (short distances) to yellow (large distances). The fits demonstrate excellent agreement with the computed data points across all sizes and distances considered. For small r, the curves show a finite size dependence: δ(N) decreases significantly with increasing N, confirming that the finite gap observed in small clusters is a size effect. In contrast, at large interatomic distances (insulating regime), the gap is almost size independent, and the extrapolated value δ_∞ closely matches the computed data for all cluster sizes. This behavior confirms the effectiveness of the extrapolation scheme and validates its use in identifying the metal–insulator transition from finite cluster data.

Fig. 5 shows the extrapolated values of the fundamental gap δ_∞ as a function of the interatomic distance r, obtained from finite-size scaling of hydrogen cubes. The curve exhibits a smooth and monotonic increase of δ_∞ with r, transitioning from metallic to insulating behavior. At short distances, δ_∞ follows an approximately linear trend. A linear regression in the interval corresponding to $r \in [1.8$ Å, 2.5 Å$]$ produces the model $\delta_\infty = 0.190 \cdot r - 0.227$ with a determination coefficient $R^2 = 0.993$. This fit predicts the closure of the gap at a critical distance $r = 1.2$ Å, corresponding to a critical electronic density of $n_c \approx 0.54\, e^-/\text{Å}^3$. Remarkably, this value agrees with the Quantum Monte Carlo diffusion estimates of the Mott transition in atomic hydrogen [13], confirming the robustness and accuracy of the present approach.

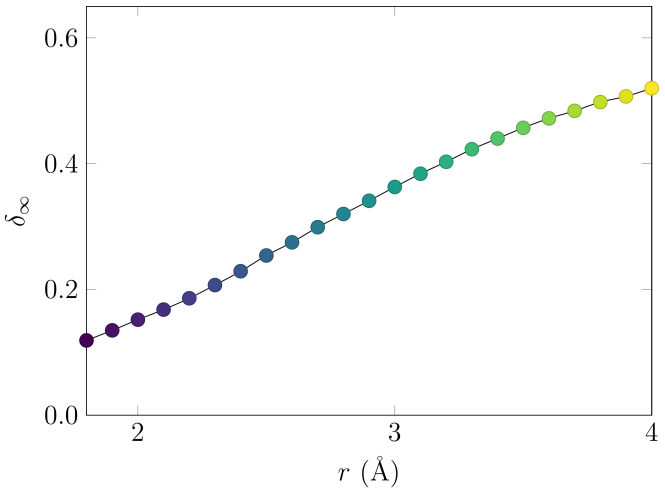

Figure 5. Extrapolated fundamental energy gap δ_∞ as a function of the interatomic distance r, obtained from finite-size scaling of hydrogen cubes with up to 512 atoms.

V. CONCLUSIONS

We have presented a comprehensive analysis of the metal insulator transition (MIT) in finite hydrogen clusters using Natural Orbital Functional Theory (NOFT). By examining both the fundamental energy gap and the harmonic average of the atomic one-particle reduced density matrix, we assessed the onset of electron localization as a function of the interatomic distance. The use of the electron-pair-based functional PNOF7 enabled an accurate description of the

metallic and insulating regimes and of the transition between them.

Through a finite-size scaling analysis applied to hydrogen cubes up to 512 atoms, we extrapolated the energy gap to the thermodynamic limit. From this analysis, we identified a critical interatomic distance of $r_c \approx 1.2$ Å, which is in excellent agreement with Quantum Monte Carlo diffusion benchmarks. These results confirm that the MIT in hydrogen clusters arises from electron correlation effects and demonstrate the ability of NOFT to capture strong correlation phenomena in large systems with high accuracy and efficiency.

Together, the findings underscore NOFT's potential as a reliable and efficient framework for exploring correlation-driven phase transitions in extended systems.

VI. ACKNOWLEDGEMENTS

JFH Lew-Yee acknowledges the Donostia International Physics Center (DIPC) and the MCIN program "Severo Ochoa" under reference AEI/CEX2018-000867-S for postdoctoral funding (Ref.: 2023/74). M. Piris acknowledges funding from MCIN/AEI/10.13039/501100011033 (Ref.: PID2021-126714NB-I00) and the Eusko Jaurlaritza (Ref.: IT1584-22).

REFERENCES

[1] N. F. Mott, *Rev. Mod. Phys.* **40**, 677 (1968).
[2] M. Imada, A. Fujimori and Y. Tokura, *Rev. Mod. Phys.* **70**, 1039 (1998).
[3] A. B. Georgescu, P. Ren, A. R. Toland, S. Zhang, K. D. Miller, D. W. Apley, E. A. Olivetti, N. Wagner and J. M. Rondinelli, *Chem. Mater.* **33**, 5591 (2021).
[4] Y. J. Lee, Y. Kim, H. Gim, K. Hong and H. W. Jang, *Adv. Mater.* **36**, 2305353 (2024).
[5] J. H. de Boer and E. J. W. Verwey, *Proc. Phys. Soc.* **49**, 59 (1937).
[6] B. H. Brandow, *Int. J. Quantum Chem. Symp.* **10**, 417 (1976).
[7] S. Kettemann, *Ann. Phys.* **456**, 169306 (2023).
[8] G. Bellomia, C. Mejuto-Zaera, M. Capone and A. Amaricci, *Phys. Rev. B.* **109**, 115104 (2024).
[9] B. Lowe, B. Field, J. Hellerstedt, J. Ceddia, H. L. Nourse, B. J. Powell, N. V. Medhekar and A. Schiffrin, *Nat. Commun.* **15**, 3559 (2024).
[10] D. M. Ceperley and B. J. Alder, *Phys. Rev. B Condens. Matter* **36**, 2092 (1987).
[11] M. A. Morales, C. Pierleoni, E. Schwegler and D. M. Ceperley, *Proc. Natl. Acad. Sci. U. S. A.* **107**, 12799 (2010).
[12] I. Silvera, *Proc. Natl. Acad. Sci. USA* **107**, 12743 (2010).
[13] J. McMinis, M. A. Morales, D. M. Ceperley and J. Kim, *J. Chem. Phys.* **143**, 194703 (2015).
[14] M. Motta, C. Genovese, F. Ma, Z.-H. Cui, R. Sawaya, G. K.-L. Chan, N. Chepiga, P. Helms, C. Jiménez-Hoyos, A. J. Millis, U. Ray, E. Ronca, H. Shi, S. Sorella, E. M. Stoudenmire, S. R. White and S. Zhang, *Phys. Rev. X* **10**, 031058 (2020).
[15] E. J. Landinez-Borda, K. O. Berard, A. Lopez and B. M. Rubenstein, *Faraday Discuss.* **254**, 500 (2024).
[16] P. Hohenberg and W. Kohn, *Phys. Rev.* **136**, B864 (1964).
[17] W. Kohn and L. Sham, *Phys. Rev.* **140**, A1133 (1965).
[18] A. I. Liechtenstein, V. I. Anisimov and J. Zaanen, *Phys. Rev. B* **52**, R5467 (1995).
[19] F. Aryasetiawan and O. Gunnarsson, *Phys. Rev. Lett.* **74**, 3221 (1995).
[20] C. Rödl, F. Fuchs, J. Furthmüller and F. Bechstedt, *Phys. Rev. B* **79**, 235114 (2009).
[21] J. Kuneš, A. V. Lukoyanov, V. I. Anisimov, R. T. Scalettar and W. E. Pickett, *Nat. Mater.* **7**, 198 (2008).
[22] O. Miura and T. Fujiwara, *Phys. Rev. B* **77**, 195124 (2008).
[23] M. Piris, *Adv. Chem. Phys.* **134**, 387 (2007).
[24] M. Piris, *Adv. Quantum Chem.* **90**, 15 (2024).
[25] S. Sharma, J. K. Dewhurst, S. Shallcross and E. K. U. Gross, *Phys. Rev. Lett.* **110**, 116403 (2013).
[26] Y. Shinohara, S. Sharma, S. Shallcross, N. N. Lathiotakis and E. K. U. Gross, *J. Chem. Theory Comput.* **11**, 4895 (2015).
[27] T. L. Gilbert, *Phys. Rev. B* **12**, 2111 (1975).
[28] M. Levy, *Proc. Natl. Acad. Sci. USA* **76**, 6062 (1979).
[29] S. M. Valone, *J. Chem. Phys.* **73**, 1344 (1980).
[30] C. Schilling, *J. Chem. Phys.* **149**, 231102 (2018).
[31] P. O. Löwdin, *Phys. Rev.* **97**, 1474 (1955).
[32] J. F. H. Lew-Yee, M. Piris and J. M. del Campo, *J. Chem. Phys.* **154**, 064102 (2021).
[33] X. Lopez, F. Ruipérez, M. Piris, J. M. Matxain and J. M. Ugalde, *Chem. Phys. Chem.* **12**, 1061 (2011).
[34] F. Ruipérez, M. Piris, J. M. Ugalde and J. M. Matxain, *Phys. Chem. Chem. Phys.* **15**, 2055 (2013).
[35] E. Ramos-Cordoba, X. Lopez, M. Piris and E. Matito, *J. Chem. Phys.* **143**, 164112 (2015).
[36] X. Lopez and M. Piris, *Theor. Chem. Acc.* **138**, 89 (2019).
[37] I. Mitxelena and M. Piris, *J. Phys. Condens. Matter* **32**, 17LT01 (2020).
[38] I. Mitxelena and M. Piris, *J. Chem. Phys.* **152**, 064108 (2020).
[39] I. Mitxelena and M. Piris, *J. Chem. Phys.* **156**, 214102 (2022).
[40] I. Mitxelena and M. Piris, *J. Chem. Phys.* **160**, 204106 (2024).
[41] P. Pulay, *Int. J. Quantum Chem.* **111**, 3273 (2011).
[42] M. Piris, X. Lopez and J. M. Ugalde, *J. Phys. Chem. Lett.* **15**, 12138 (2024).
[43] J. Liebert and C. Schilling, *SciPost Phys.* **14**, 120 (2023).
[44] L. Ding, C.-L. Hong and C. Schilling, *Quantum* **8**, 1525 (2024).
[45] M. Piris, *Chem. Sci.* **15**, 17284 (2024).
[46] M. Piris, *Int. J. Quantum Chem.* **113**, 620 (2013).
[47] M. Piris, *Phys. Rev. Lett.* **119**, 063002 (2017).
[48] M. Piris, *Phys. Rev. Lett.* **127**, 233001 (2021).
[49] L. Franco, J. F. H. Lew-Yee and J. M. del Campo, *AIP Adv.* **13**, 065213 (2023).
[50] J. F. H. Lew-Yee, J. M. del Campo and M. Piris, *J. Chem. Theory Comput.* **19**, 211 (2023).
[51] L. Franco, R. Rojas-Hernández, I. A. Bonfil-Rivera, E. Orgaz and J. M. del Campo, *Phys. Chem. Chem. Phys.* (2025).

[52] J. F. H. Lew-Yee, I. A. Bonfil-Rivera, M. Piris and J. M. del Campo, *J. Chem. Theory Comput.* **20**, 2140 (2024).
[53] A. Rivero-Santamaría and M. Piris, *J. Chem. Phys.* **160**, 071102 (2024).
[54] J. F. H. Lew-Yee, M. Piris and J. M. del Campo, *J. Chem. Phys.* **158**, 084110 (2023).
[55] J. F. H. Lew-Yee and M. Piris, *J. Chem. Theory Comput.* **21**, 2402 (2025).
[56] M. Piris and I. Mitxelena, *Comput. Phys. Commun.* **259**, 107651 (2021).
[57] L. Franco, I. A. Bonfil-Rivera, J. F. H. Lew-Yee, M. Piris, J. M. del Campo and R. A. Vargas-Hernández, *J. Chem. Phys.* **160**, 244107 (2024).
[58] J. F. H. Lew-Yee, J. M. del Campo and M. Piris, *Phys. Rev. Lett.* **134**, 206401 (2025).
[59] A. J. Coleman, *Rev. Mod. Phys.* **35**, 668 (1963).
[60] M. Piris, G. G. N. Angilella and C. Amovilli, eds., *Many-body approaches at different scales: a tribute to N. H. March on the occasion of his 90th birthday*, chapter 22, p. 261–278 (Springer, New York, 2018).
[61] D. A. Mazziotti, *Chem. Rev.* **112**, 244 (2012).
[62] M. Piris, R. Carbó-Dorca and T. Chakraborty, eds., *Quantum Chemistry at the Dawn of the 21st Century. Series: Innovations in Computational Chemistry*, chapter 22, p. 593–620 (Apple Academic Press, 2018).
[63] M. Piris, *Phys. Rev. A* **100**, 32508 (2019).
[64] I. Mitxelena, M. Rodríguez-Mayorga and M. Piris, *Eur. Phys. J. B* **91**, 109 (2018).
[65] M. Piris, *J. Math. Chem.* **25**, 47 (1999).
[66] R. Ditchfield, W. J. Hehre and J. A. Pople, *J. Chem. Phys.* **54**, 724 (1971).
[67] A. V. Sinitskiy, L. Greenman and D. A. Mazziotti, *J. Chem. Phys.* **133**, 014104 (2010).

THE ROLE OF CLAY CHARGE IN THE MOBILITY OF COMPENSATING CATIONS: AN APPROACH FROM MOLECULAR DYNAMICS

EL PAPEL DE LA CARGA DE LA ARCILLA EN LA MOVILIDAD DE LOS CATIONES DE COMPENSACIÓN: UNA APROXIMACIÓN DESDE LA DINÁMICA MOLECULAR

C. D. Marrero-Pérez [a], G. Rojas-Lorenzo[b], A. Lam[a†]

a) Zeolite Engineering Laboratory, Institute of Material Science and Technology (IMRE), University of Havana, Havana, CP. 10400. Cuba. krlodavid419@gmail.com, anabel@imre.uh.cu†
b) Instituto Superior de Tecnologías y Ciencias Aplicadas (InSTEC). Universidad de La Habana, La Habana - 10400, Cuba. german@instec.cu
† corresponding author

Recibido 5/2/2025; Aceptado 5/7/2025

The charge of clays plays an important role in the mobility of compensating cations and in swelling processes. In this work we have developed a method to generate Lithium Fluorhectorite (Li-Fh) clay models with a charge of -1.2*e* and a non-homogeneous charge distribution. This charge is closer to the experimentally reported value. We used this approach to study their interaction with water using Molecular Dynamics (MD) simulations. The MD simulations showed that the Li^+ diffusion coefficient increases by two orders of magnitude with decreasing clay charge. Population analyses and Li^+ coordination indicate a greater interaction of the cations with water molecules with decreasing clay charge, leading to a deformation in the stacking of clay layers in the 010 model. These results highlight the important influence of clay charge on cation dynamics and structural behaviour, providing insight into delamination and swelling mechanisms.

La carga de las arcillas desempeña un rol importante en la movilidad de los cationes de compensación y en los procesos de hinchamiento. En este trabajo hemos desarrollado un método para generar modelos de la arcilla Litio Fluorhectorita (Li-Fh) con carga igual a -1,2*e* y una distribución de carga no homogénea. Esta carga se aproxima más al valor reportado experimentalmente. Utilizando simulaciones de dinámica molecular (DM) hemos estudiado la interacción de la Li-Fh con agua. Las simulaciones de DM mostraron que el coeficiente de difusión del Li^+ aumenta en dos órdenes de magnitud con la disminución de la carga de la arcilla. Los análisis de población y la coordinación del Li^+ indican una mayor interacción del catión con las moléculas de agua al disminuir la carga de la arcilla, lo que conduce a una deformación en el apilamiento de las láminas en el modelo 010. Estos resultados ponen de relieve la importante influencia de la carga de la arcilla en la dinámica de los cationes y el comportamiento estructural, proporcionando una visión de los mecanismos de delaminación e hinchamiento.

Keywords: Molecular Dynamics Calculations (Cálculos de Dinámica Molecular); Diffusion in nanoscale solids (Difusión en sólidos en la nanoescala); Computer modeling; simulation (Modelación y simulación computacional).

I. INTRODUCTION

Clay materials, with their unique layered structures and inherent ion-exchange capabilities, are widespread in nature and indispensable in many technological applications [1]. The ability of clays to selectively adsorb and release ions is fundamental to a wide range of processes, including soil fertility management [2], wastewater treatment [3] and the development of advanced materials [4]. In agriculture, clays play a crucial role in retaining essential nutrients and regulating their availability to plants [5]. In environmental remediation, they are used to remove heavy metals and organic contaminants from contaminated water and soil [6]. Furthermore, the ion-exchange properties of clays are exploited in catalysis [7], drug delivery systems [8, 9] and the preparation of novel nanocomposites [10]. Consequently, a thorough understanding of the mechanisms governing ion exchange in clay materials is essential to optimise their performance in existing applications and to explore new opportunities in various scientific and technological fields. The isomorphic substitution of higher valence atoms for lower valence atoms within the clay framework creates a negative charge density that is neutralized by Group I and II cations, known as compensating cations. These compensating cations are located in the interlayer spaces and on the surface of the clay. Together with water molecules, they exhibit high mobility within the material. The interaction of these compensating cations with water molecules and the clay framework influences processes such as ion exchange and swelling. Smectite-type clays with charges between -0.2 and -0.6*e* are known to swell. However, in materials with higher charges, such as micas, the cation-clay lattice interactions prevent swelling [11]. Lithium fluorhectorite clay (Li-Fh) is a 2:1 layered silicate in which a fraction of the Mg^{2+} cations in the trioctahedral sites are replaced by Li^+ cations, resulting in a negative structural charge that is compensated by Li^+ ions in the interlayer space. Its chemical composition is $Li_x(Mg_{6-x}Li_x)F_4Si_8O_{20}$. Li-Fh can be delaminated into single layers by osmotic swelling in deionized water [11]. In previous work, we investigated the cation motion of Li-Fh clay models with a charge of -2*e* using molecular dynamics (MD) simulations [12]. However, the actual charge of this material

is much lower, closer to -1.2*e* [13,14]. To evaluate the influence of clay charge on the movement of Li^+ compensating cations and their interaction with water, we created one hundred Li-Fh models with a charge of -1.2*e* by modifying models with a charge of -2*e*. Then, MD simulations were performed to evaluate the energy of the 100 models, and we selected the most stable one to build models representing the clay lattice in three different scenarios: in the center of the crystal (bulk model), on the surface created by removing the periodicity in the crystallographic b direction (010 model), and on the surface without periodicity along the c direction (001 model). Finally, the diffusion of Li^+ in the three models with charge -1.2*e* is studied and compared with that obtained for the model with charge -2*e*. The results obtained here will shed light on the role of clay charge in the mobility of compensating cations and their interaction with the clay framework and water, thus contributing to the understanding of complex processes such as swelling and ion exchange.

II. METHODOLOGY

In our previous studies, we employed a LiFh model consisting of 75 unit cells, generated by $5 \times 5 \times 3$ replication of the LiFh unit cell along the crystallographic axes [12,15]. In each unit cell of those models, two magnesium atoms in the octahedral sheet were replaced by two lithium atoms, resulting in a -2*e* charge balanced by two lithium compensating cations (Li^+). The unit cell formula was $Li_2^+(Mg_4Li_2)F_4Si_8O_{20} \times 12H_2O$. However, this model overestimates the true charge, which is closer to -1.2*e* [13, 14]. Therefore, we developed a method to adjust the charge of the initial model [12, 15] and generate models with a -1.2*e* charge. This involved randomly replacing one lithium atom in the octahedral layer with a magnesium atom and removing one Li^+ compensating cation in 60 of the 75 unit cells, resulting in unit cells with the formula $Li^+(Mg_5Li)F_4Si_8O_{20} \times 12H_2O$. The remaining 15 unit cells retained the original formula $Li_2^+(Mg_4Li_2)F_4Si_8O_{20} \times 12H_2O$. In this way, 100 different periodic models with a non-homogeneous charge distribution of -1.2*e* were created. The Python code used in this study is available in Section S1 of the Supporting Information. The interatomic interactions in lithium fluorohectorite (LiFh) were modeled using the CLAYFF force field [16], with minor modifications to the atomic charges to ensure electroneutrality. CLAYFF incorporates electrostatic interactions, which are calculated using coulombic forces, and van der Waals interactions, which are described using a 12-6 Lennard-Jones potential. For model 010, the surface OH valence-compensating groups were modeled using Morse potential terms for edge surfaces, as proposed by Pouvreau et al [17]. However, as explained in previous work, the angle term and water potential proposed by Pouvreau et al. could not be fitted to our model [12]. We adopted the parameters of the Li^+ compensating cation, including its charge (+1*e*) and Lennard-Jones coefficients, from Koneshan et al [18]. The full details of the charges and parameters used in the CLAYFF force field can be found in Section S2 of the Supporting Information. Molecular dynamics (MD) simulations were performed using the DL_POLY code [19] to determine the total energy of the 100 periodic models. The first MD calculations were performed in the NVE ensemble during 20 ps at 300 K, with temperature control during the first 10 ps. The time step used in all simulations was 1fs. The ten models with the lowest energy were selected and additional MD simulations were performed. The second MD simulations were done in the NVE ensemble during 200 ps without temperature control. Finally, 200 ps MD runs were performed in the NPT ensemble to allow the models to adjust the volume. In all simulations the temperature was set to 300 K and the pressure in the NPT simulations was 1atm. At the end of the third MD simulation, the total energy of the ten models was evaluated and compared to select the most stable one.

The most stable model of charge -1.2*e* was used to build three different models to evaluate the Li^+ movement, see Figure 1. The first is the periodic model resembling the clay bulk. The other two models were constructed by cleaving the periodicity in the crystallographic directions b and c, as described in reference [12], and were designated 010 and 001. These two models are in contact with a water reservoir containing 1493 and 1205 water molecules, respectively, and were equilibrated as described in reference [12]. Once the three models (bulk, 010 and 001) were perfectly equilibrated, the 20 ns production runs were performed in the NPT ensemble at a pressure of 1 atm and a temperature of 300 K, with an integration time step of 1 fs. The Nosé-Hoover thermostat and barostat were used [20, 21], each with a relaxation time of 100 fs. Periodic boundary conditions were applied in all simulations, and the Ewald summation method was used to calculate the electrostatic interactions of the systems [22, 23]. The cutoff for long-range interactions -Coulomb and Lennard-Jones potentials- was set to 10 Å. The trajectory of the atoms in the NPT simulations was collected every 5000 steps for dynamics and structure analysis. Radial distribution functions (rdf), the population functions (n(r)), and the Li^+ coordination were calculated and collected every 5ps for the interaction of the Li^+ with the oxygens of clay (O_{clay}) and oxygens of water (OW). The Diffusion coefficient and the type of motion of Li^+ cations were also determined. The diffusion coefficient (D) for each elemental species was calculated from molecular dynamics (MD) trajectories using the Einstein-Smoluchowski relation, which relates D to the asymptotic slope of the mean squared displacement (MSD) in the diffusive regime [22,23]. In DL_POLY, the atomic displacements were analyzed by calculating the MSD from particle trajectories recorded in the HISTORY file at 5000 step intervals, with ensemble averaging over all particles of each element and multiple time origins. The diffusion coefficient was determined by linear regression of the MSD(t) curve according to:

$$D = \frac{1}{6N} \lim_{t\to\infty} \frac{d}{dt} \sum_{i=1}^{N} |\vec{r}_i(t) - \vec{r}_i(0)| \quad (1)$$

where N is the number of particles for the particular element, and $\vec{r}_i(t)$ is the position vector of particle i at time t. The linear regime has been carefully identified by excluding the initial short-time ballistic motion (typically t < 10 ps). This

methodology is well established for equilibrium systems and has been rigorously validated against both theoretical predicions and experimental measurements for comparable systems.

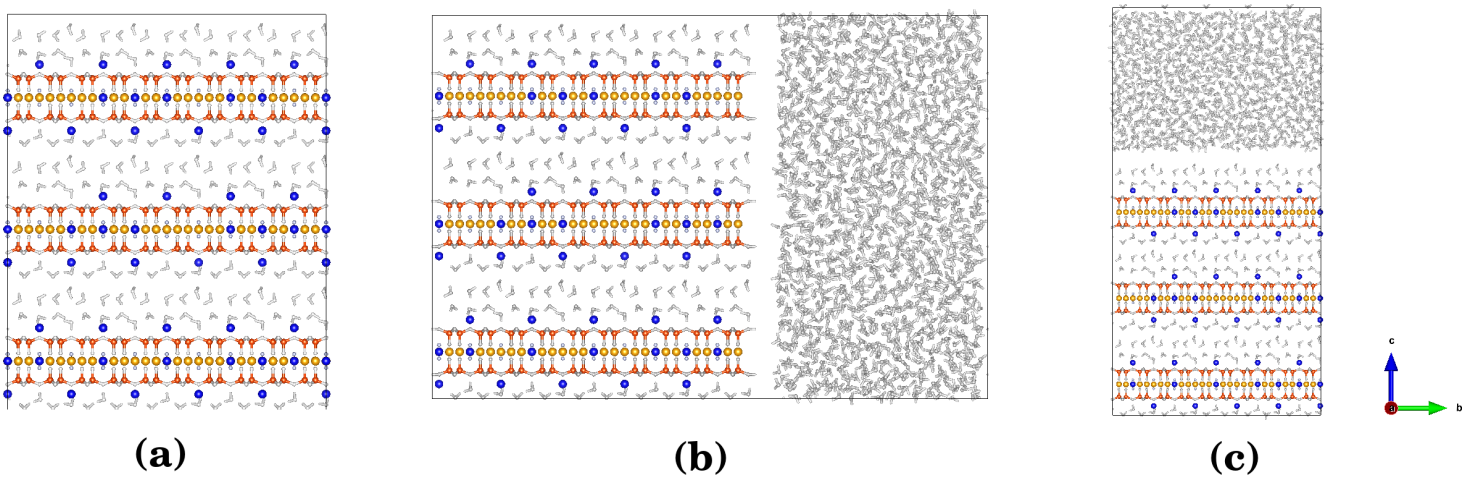

Figure 1. The models of charge -1.2e used in the simulations, (a) bulk model, (b) 010 model, (c) 001 model. The orange, gray, blue, yellow, pink, and white spheres correspond to Si, O, Li, Mg, F, and H atoms, respectively. The simulation boxes are enclosed by the black rectangles.

III. RESULTS AND CONCLUSIONS

The relative energies of the most stable models are shown in Table 1. They have been calculated as the energy difference with the model of lower energy. Model 31 exhibits the highest stability, with an energy difference of 40 kcal/mol compared to the other models. The thermal energy of the system is negligible compared to this energy gap (see Section S3 of the Supporting Information for details).

Table 1. Relative energies of the ten most stable models.

Models	ΔE (kcal/mol)
31	0
7	40
53	60
15	60
75	70
65	70
36	70
21	70
62	80

Therefore, thermal fluctuations cannot explain the observed differences in stability between the models. In model 31, the unit cells with q = -2*e*, which we consider defects, are distributed among the three clay layers: six in one layer and four or five in the other two layers. Model 31 was then used to create three clay models: bulk, 010, and 001 (see Figure 1).

As in our previous work related to the movement of Li^+ in the -2*e* charged LiFh model [12], we want to evaluate the Li^+ diffusion in different environments represented by our three models and relate this diffusion to the clay charge. In the models with -1.2*e* charge, we observed a significant number of Li^+ cations moving from their initial positions located near the hexagonal cages inside the clay layer. Of the 90 Li^+ ions in each model, 84 moved from their initial positions in the bulk model, while 80 and 78 moved in the 010 and 001 models, respectively.These results contrast sharply with our previous results for the -2*e* charged model, where only 20 of 150 Li^+ cations moved from their initial positions in the 010 model [12].

This comparison highlights the critical role of clay charge in influencing the mobility of compensating cations, which has implications for all related properties and applications of this material. During the 20 ns simulations, Li^+ cations exhibited several types of motions: (I) remaining in their initial position, (II) moving to another hexagonal cage within the same layer, (III) moving to the interlayer space, (IV) diffusing into the outer water reservoir (for 010 and 001 models), (V) crossing the interlayer and occupying the opposite layer, (VI) diffusing to another layer, and (VII) moving to an octahedral edge. Movements VI and VII were only observed in the 010 model after movements III and IV. Figure 2 shows a schematic representation of these motions in the 010 model.

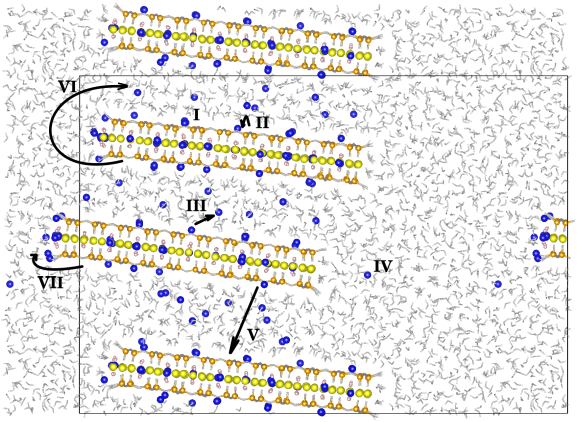

Figure 2. Schematic representation of the possible Li^+ motions at the 2 ns of 010 simulation. Various movements of the Li^+ cations in the 010 model are depicted and denoted using Roman numerals as explained in the text. The simulation box is indicated within the black rectangle, and boundary conditions were applied to enhance visualization. The orange, grey, blue, yellow, pink and white spheres correspond to Si, O, Li, Mg, F and H atoms respectively.

Table 2 shows the number of Li^+ cations that remained in their initial positions (I) and those that diffused via different types of motion. As shown, only six Li^+ ions remained in their initial positions in the bulk model, compared to 10 and 12 in the 010 and 001 models, respectively. This suggests a stronger interaction between the clay and its native cations at the edges.

Table 2. Li cations moving in the three models organized by the type of movement. (I) remaining in their initial position, (II) moving to another hexagonal cage within the same layer, (III) moving to the interlayer space, (IV) diffusing into the outer water reservoir (for 010 and 001 models), (V) crossing the interlayer and occupying the opposite layer, (VI) diffusing to another layer, and (VII) moving to an octahedral edge.

Type of movement of Li^+	Bulk	010	001
I	6	10	12
II	24	23	17
III	37	18	29
IV	-	18	14
V	23	12	18
VI	-	15	-
VII	-	12	-

In the bulk model, 24 Li^+ cations moved to another hexagonal cage within the same layer, 37 diffused into the interlayer region, and 23 crossed the interlayer and occupied positions in the opposite layer. In the 001 model, 17 Li^+ ions moved to another hexagonal cage within the same layer, 18 diffused into the opposite layer, and 29 were located in the interlayer region. During the simulation, 19 of 30 Li^+ ions diffused into the outer water reservoir. At the end of the simulation, 14 cations remained in the outer water reservoir and 5 cations had diffused beyond the 30 Å width of the water reservoir and settled in the opposite layer. In contrast, in the 001 model with a -2*e* charge, only 2 Li^+ cations diffused into the water reservoir during simulation [12]. This further emphasizes the strong relationship between the clay charge and the mobility of the compensating cations.

Clay materials, especially hectorite clays, swell when they interact with water. The amount of water in the interlayer space modulates the interactions between the clay lamellae. The cation-cation and cation-clay interactions are also modulated. Typically, clays with up to 25 weight percent water are in the crystalline swelling regime [24]. In the 010 model, the clay interacts with 2393 water molecules (900 in the interlayer space and 1493 in the external reservoir). The water content in the system is approximately 43 % by weight. This places the system in the osmotic swelling regime, suggesting that delamination of the material might be expected. The osmotic delamination of Li^+-fluorhectorite clays is known to result in nanolayers as thin as 1 nm (10) [11]. In water, the individual layers can arrange themselves into a "house of cards"structure, as observed at the end of the simulation in model 010. During simulation, we observed the displacement of the clay layers as they interacted with the water, including a deformation of the intermediate layer, which has the lowest charge density (see Figure SI1 and the link of the video_010 in the supporting information). This deformation results in a final system configuration that is highly deformed compared to the initial model. Figure SI2 shows the 010 reflection of the diffraction patterns of the initial configuration and the selected configurations: 0.65, 3.29, 4.05 and 5.31 ns. As can be seen, the 2θ values decrease during the simulation due to the increase in the b crystallographic parameter (from 81.94 to 83.61 Å) caused by the displacement of the clay layers. The intensity of the peaks also decreases, indicating a loss of crystallinity of the model.

Therefore, the Li^+ cation diffusion process in the 010 model undergoes motions different from those described for the bulk and 001 models. In particular, as the lamellar order is lost, a large number of cations are trapped in a space between the clay layers (about 33 Å) that contains a significant number of water molecules. This confinement of cations in such a disordered system could explain why the diffusion coefficient of Li^+ cations is lower in the 010 model than in the 001 model, as shown in Table III.

Table 3. Diffusion coefficients (D) of the Li^+ and water molecules in the clay models.

Model charge	D ($\times 10^{-9}$ m^2 s^{-1})				
	q = -1.2e			q = -2e[a]	
Model	Bulk	010	001	010	001
Li^+	0.1581	0.1876	0.3171	1.2427×10^{-3}	6.3917×10^{-3}
OW	1.8022	3.9434	2.7717	4.1367	3.0629

[a] Reference [12]

The diffusion coefficients (D) of the LiFh models with charge -1.2*e* are two orders of magnitude higher than those of the models with charge of -2*e* (Table 3), consistent with our previous discussion indicating that Li^+ mobility is greater in lower charged clay models. Table 3 also shows that in the LiFh models with q=-1.2*e*, the diffusion coefficients are very similar, following the trend 001 > 010 > Bulk. As discussed above, the lower D value observed in the 010 model compared to the 001 model is attributed to the confinement of Li^+ cations in the deformed interlayer region. The lower D value of the bulk model can be associated with the greater confinement of Li^+ cations within the interlayer, which restricts their movement compared to the models with surfaces in contact with a water reservoir. This confinement effect in the bulk model is also responsible for the lower D value of the water molecules.

To further characterize the diffusion mechanism, we analyzed the mean square displacement (MSD) of Li^+ cations versus time (Figure SI3 of the Supporting Information). The logarithmic plot (log(MSD) vs log(t)) reveals normal (Fickian) diffusion (slope m ≈ 1), despite cation intercalation. This behavior stems from the interlayer spacing's capacity to accommodate three water layers, preventing steric crowding and maintaining bulk-like mobility. The absence of subdiffusive exponents (m ≈ 0.5) excludes single-file or strongly confined diffusion under these conditions, consistent with expectations for such hydrated systems.

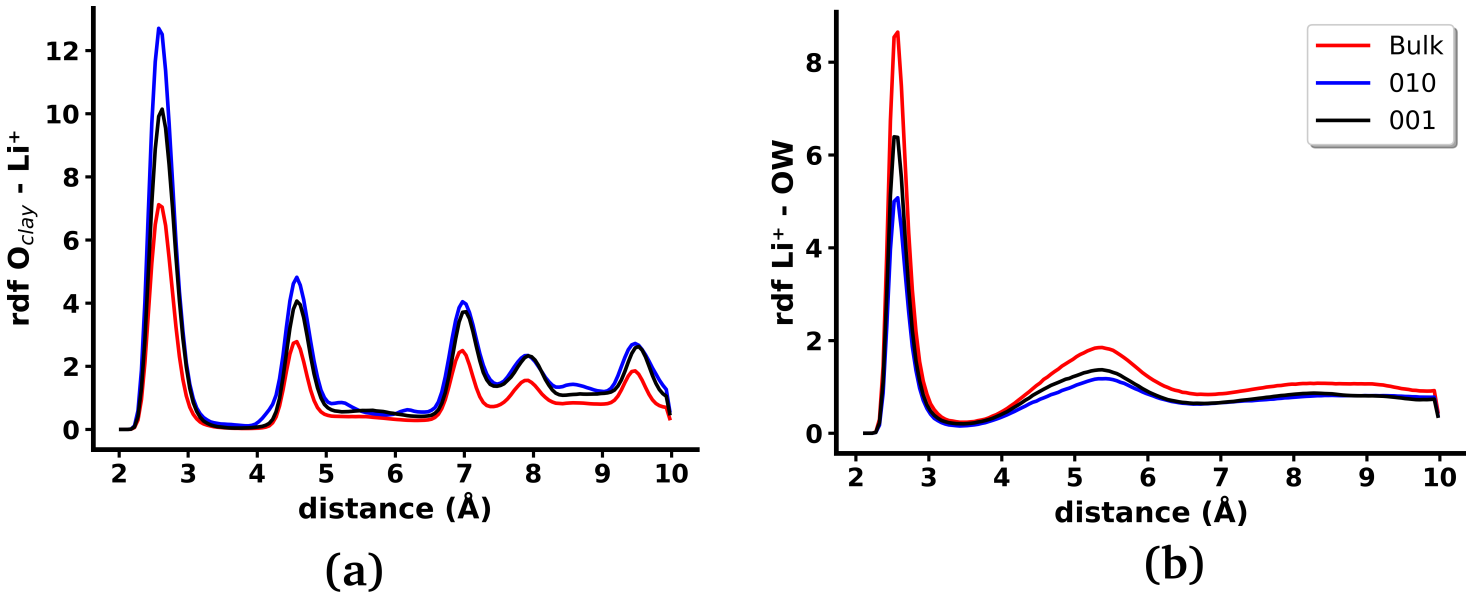

Figure 3. Radial distribution function (a) O_{clay}-Li^+ and (b) Li^+-OW for the three different models: bulk (red line), 010 (blue line) and 001 (black line).

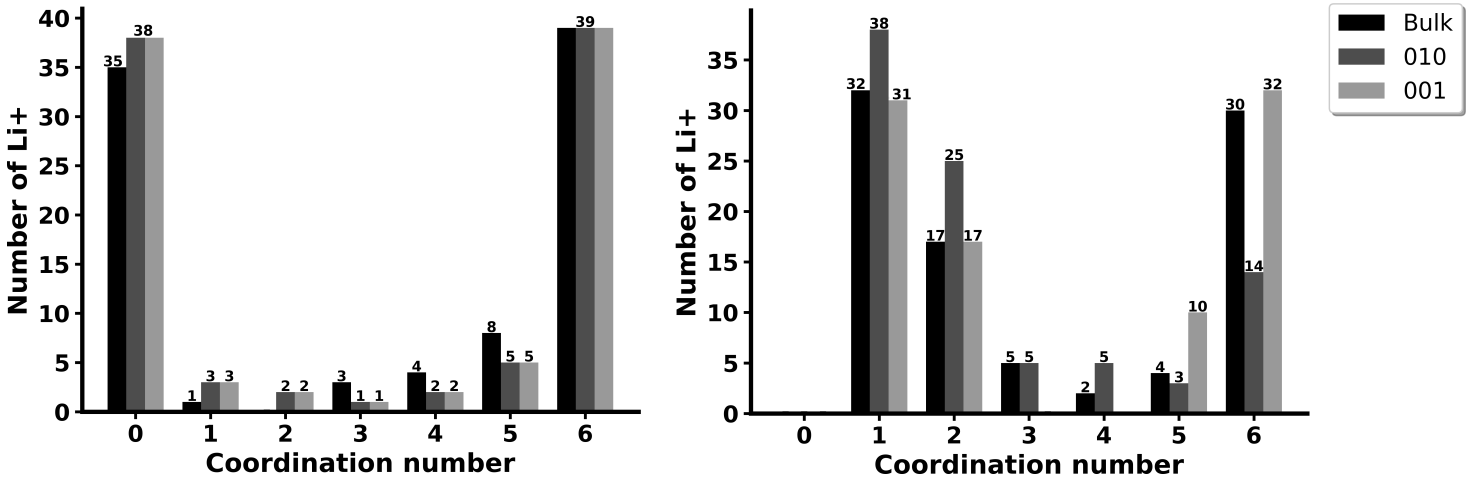

Figure 4. Number of Li^+ coordinated with (a) with clay oxygens (b) with water molecules.

Li^+ cations exhibit a jump diffusion mechanism characterized by rapid displacements. The same diffusion mechanism has been observed in our models with q = -2*e* [12]. Figure SI4 shows examples of displacements ($\mathbf{r} - \mathbf{r}_0$) as a function of time for selected Li^+, representative of movements II to V. Initially, Li^+ labeled 117 (green line in Fig. SI4) is located on a clay layer at the surface in contact with the water reservoir. This cation traverses the water reservoir during the simulation and is finally located on the opposite clay layer, having traveled a distance of 30 Å. In contrast, the labeled Li^+ 78 (black line in Fig. SI4) moves through the interlayer space. Between 9.2 ns and 14.825 ns it is confined in a hexagonal cage within the same layer. Then it diffuses back into the interlayer space, moving through it and approaching both layers. The trajectory of Li^+ 2028 (blue line in Fig. SI4) is also shown. Similar to cation 78, it diffuses through the interlayer space and approaches the opposite clay sheet for about 5.7 ns. It then remains in a hexagonal cage of the opposite sheet for about 3 ns before returning to the interlayer space. Later, at 10 ns and again at 16.5 ns, it returns to another hexagonal cage in the same layer where it was at 5.7 ns. Cations 78 and 2028 exhibit type II, III, and V motions.

The interaction of the lithium cations with clay and water significantly affects cation diffusion. This interaction can be evaluated using radial distribution functions (rdfs) and population analysis. Figure 3 shows the rdfs of lithium cations with oxygen from clay (O_{clay}-Li^+) and with oxygen from water (Li^+-OW) for the evaluated models. The rdfs for O_{clay}-Li^+ and Li^+-OW are very similar in all three models and closely resemble those obtained in the LiFh clay model with q = -2*e* [12]. The maximum of the first peaks, associated with the coordination of Li^+ with oxygens, in both O_{clay}-Li^+ and Li^+-OW is approximately 2.575.

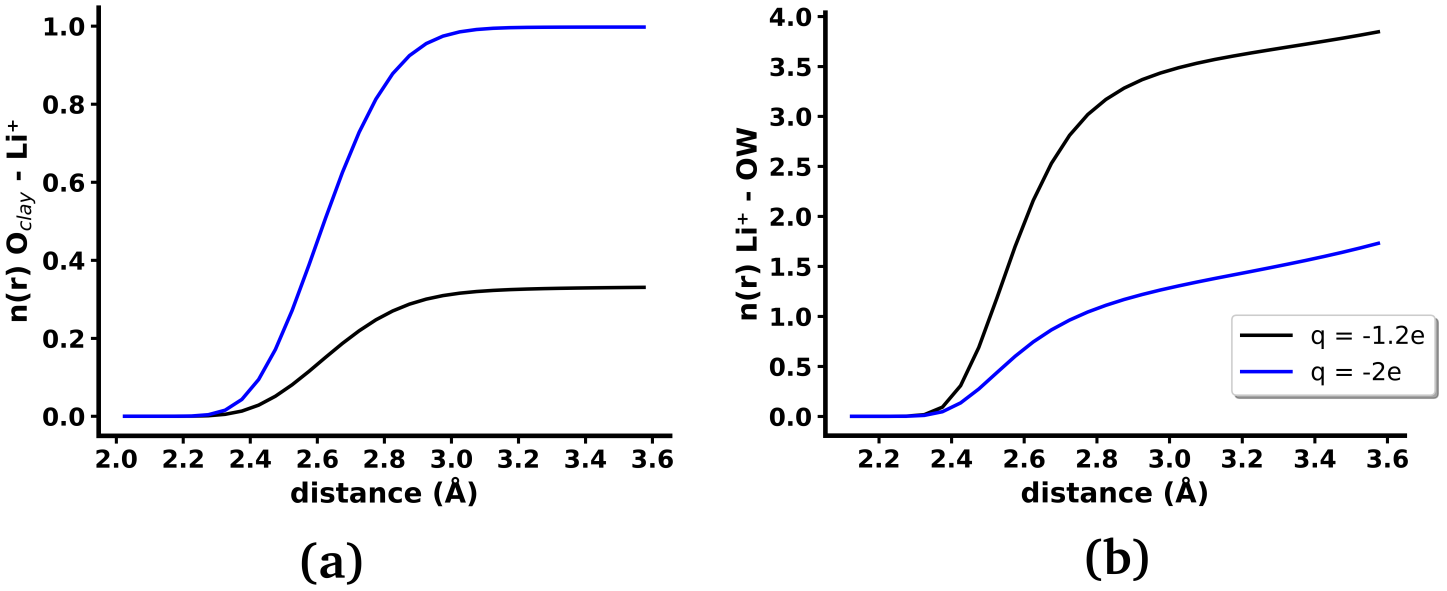

Figure 5. (a) n(r) O_{clay}-Li^+ and (b) n(r) Li^+-OW for the 001 model with charge equal -2*e* (blue line) and -1.2*e* (black line).

Figure 4 shows the coordination number of Li^+ cations with oxygen atoms from both clay and water molecules, calculated for Li^+-O distances shorter than 3 Å, using the final production run configuration for all three models. As observed, all Li^+ cations are coordinated with at least one water molecule. Those Li^+ cations that remain in their position or move to another hexagonal cage in their layer or in the opposite layer (movements I, II, and V, respectively) are coordinated with six oxygen atoms of the clay framework and with few water molecules. In contrast, Li^+ cations located in the interlayer space or diffusing into the bulk water (type III or IV motions) are expected to coordinate with a larger number of water molecules rather than the clay oxygens.

In the bulk and the 001 models, low (1) and high (6) coordination with clay and water molecules predominate, which is consistent with the results shown in Table 2. In these models, Li^+ cations are mainly located near the clay or in the interlayer space. Furthermore, there are more Li^+ cations coordinated with 5 or 6 water molecules in these models compared to the 010 model.

In the 010 model, there are more Li^+ cations coordinated with 1 and 2 water molecules. This difference is probably due to the deformation of the 010 model in the presence of water. Finally, the role of the clay charge on the mobility of the compensating cations can be better understood by analyzing the population functions, n(r), obtained from the radial distribution functions (rdf). In the Li-Fh models with a charge of -2*e* that we used previously [12], each oxygen atom in the clay experienced at least one Li^+ cation at a distance of less than 3 Å (blue line in Figure 5a). This is only possible when Li^+ is placed in the center of the hexagonal cage.

When the charge of the clay model is -1.2*e*, the value of n(r) decreases by 0.2, indicating that only 2 out of 10 oxygen atoms in the clay have a Li^+ cation at distances less than 3 Å. In contrast, the value of n(r) for Li^+-OW, which provides information about the average number of water molecules at distances lower than 3 for each Li^+ cation, increases from 1 to 3.5. This suggests that as the clay charge decreases, the cations interact less with the framework of the material and more with water molecules, leading to increased diffusion of Li^+ cations.

IV. CONCLUSION

Model 31 was found to be the most stable of the one hundred Li-Fh models generated with a charge of -1.2e. Based on this, three models were constructed: bulk, 010, and 001. The diffusion and movement of Li+ cations were studied in all three models. Li+ cations can move within the interlayer space, jump into hexagonal cavities within the same or opposite layers, and diffuse into the solution in the surface models. They can also migrate to other layers or to the edge of the octahedral sheet in the 010 model. In Li-Fh models with -1.2*e* charge, a larger number of Li+ ions diffuse with diffusion coefficients two orders of magnitude higher than in models with -2e charge. The diffusion coefficients (D) are similar in the three models, following the order 001 > 010 > Bulk. The compensating cations coordinate with a high number of clay oxygens (6) when they are in the hexagonal cavity of the clay lattice, or with a high number of water molecules (6) when they are in the interlayer or diffuse into the solution. The n(r) values also indicate that Li+ ions interact with a greater number of water molecules in the lower charge models. When the 010 model is in contact with a water reservoir, the osmotic swelling process occurs, leading to the observation of layer deformation resulting in a "house of cards"structure. A significant number of Li+ cations are trapped in the deformed structure, which is why the value of D is lower in this model than in the 001 model. The results demonstrate the importance of the clay charge for understanding the movement of Li+

cations, their interaction with clay and water molecules, and the accurate reproducibility of delamination and swelling processes of clays.

V. SUPPORTING INFORMATION

The supplementary online materials include the Python code for generating nonhomogeneous LiFh models, the force fields model description, description of the thermal energy contribution in the clay-water system, and URL links to simulation videos.

VI. ACKNOWLEDGEMENTS

The authors would like to thank Cuban National Programs PN211LH008-027 and PN223LH010-017 for financial support.

REFERENCES

[1] F. Bergaya, B. K. G. Theng, G. Lagaly, *Handbook of Clay Science: Clay Mineral Control of Soil Organic Matter: A Conceptual Model Based on Physical Interactions* (Elsevier, 2006).
[2] M. Yu, S. M. Tariq, H. Yang, Clay Minerals **57**, 51 (2022).
[3] S. Khan, S. Ajmal, T. Hussain, M. U. Rahman, J. UQ. Univ. Appl. Sci. **9**, 1 (2023).
[4] Y. Lan, Y. Liu, J. Li, D. Chen, G. He, I. P. Parkin, Adv. Sci. **8**, 2004036 (2021).
[5] A. C. D. Newman, Phil. Trans. R. Soc. Lond. A **311**, 375 (1984).
[6] B. O. Otunola y O. O. Ololade, Environ. Tech. & Innov. **18**, 100692 (2020).
[7] A. Ochirkhuyag, J. Temuujin, Minerals **14**, 629 (2024).
[8] J. Dong, Z. Cheng, S. Tan, y Q. Zhu, Expert Opin. Drug Deliv. **18**, 695 (2020).
[9] C. Aguzzi, P. Cerezo, C. Viseras, C. Caramella, Appl. Clay Sci. **36**, 22 (2007).
[10] M. M. Orta, J. Martín, J. L. Santos, I. Aparicio, S. Medina-Carrasco, E. Alonso, Appl. Clay Sci. **198**, 105838 (2020).
[11] H. Kalo, M. W. Möller, D. A. Kunz, J. Breu, Nanoscale **4**, 5633 (2012).
[12] A. Lam y G. Rojas-Lorenzo, Rev. Cubana Fis. **41**, 10 (2024).
[13] R. P. Tenório, M. Engelsberg, J. O. Fossum, G. J. da Silva, Langmuir **26**, 9703 (2010).
[14] L. Michels, C. L. S. da Fonseca, Y. Méheust, M. A. S. Altoé, E. C. dos Santos, G. Grassi, R. Droppa Jr., K. D. Knudsen, L. P. Cavalcanti, K. W. B. Hunvik, J. O. Fossum, G. J. da Silva, H. N. Bordallo, J. Phys. Chem. C **124**, 24690 (2020).
[15] A. Lam, G. Rojas-Lorenzo, Rev. Cubana Fis. **39**, 85 (2022).
[16] R. T. Cygan, J. J. Liang, A. G. Kalinichev, J. Phys. Chem. B **108**, 1255 (2004).
[17] M. Pouvreau, J. A. Greathouse, R. T. Cygan, A. G. Kalinichev, J. Phys. Chem. C **123**, 11628 (2019).
[18] S. Koneshan, J. C. Rasaiah, R. M. Lynden-Bell, S. H. Lee, J. Phys. Chem. B **102**, 4193 (1998).
[19] I. Todorov, W. Smith, K. Trachenko, M. Dove, J. Mater. Chem. **16**, 1911 (2006).
[20] W. G. Hoover, Phys. Rev. A **31**, 1695 (1985).
[21] S. Nosé, J. Chem. Phys. **81**, 511 (1984).
[22] M. P. Allen, D. J. Tildesley, *Computer Simulation of Liquids*, 2nd ed. (Oxford University Press, Oxford, UK, 2017).
[23] P. E. Smith, B. M. Pettitt, Comput. Phys. Commun. **91**, 339 (1995).
[24] F. Kraehenbuehl, H. F. Stoeckli, F. Brunner, G. Kahr, M. Mueller-Vonmoos, Clay Minerals **1**, 1 (1987).

NEW SIGMOID CURVES: BEYOND THE TRADITIONAL LOGISTIC MODELS

NUEVAS CURVAS SIGMOIDALES: MÁS ALLÁ DE LOS MODELOS LOGÍSTICOS TRADICIONALES

M. T. Pérez-Maldonado[a†], J. Bravo-Castillero[b], R. Mansilla[c], R. O. Caballero-Pérez[d]

a) Department of Theoretical Physics. Physics Faculty, University of Havana, mtperez@fisica.uh.cu†
b) UA-IIMAS-EY, Universidad Nacional Autónoma de México
c) CEPHCIS-CEIICH, Universidad Nacional Autónoma de México
d) Independent researcher
† corresponding author

Recibido 4/3/2025; Aceptado 15/6/2025

S-shaped or sigmoid curves can be defined as the solutions of autonomous first-order differential equations that satisfy four conditions. Without solving the equations, we demonstrate that the solutions of the logistic family and the Smith-Birch model satisfy these conditions. We introduce two generalizations of the Smith-Birch, whose solutions are identified as S-shaped for some range of variation of the parameters. The new models introduced here predict the spread of the disease better than traditional logistic family models for time series of the cumulative number of cases for the first 61 days of the COVID-19 pandemic in some countries.

Las curvas en forma de S o curvas sigmoidales pueden definirse como soluciones de ecuaciones diferenciales autónomas de primer orden que cumplen con cuatro condiciones, a través de las cuales se demuestra sin necesidad de resolverlos que los modelos de la familia logística generalizada y el de Smith-Birch tienen soluciones sigmoidales. Se introducen dos generalizaciones del modelo de Smith-Birch, cuyas soluciones son curvas sigmoidales para cierto rango de variación de los parámetros. Se encontraron series temporales del número cumulativo de casos para los 61 primeros días de la pandemia de COVID-19 en algunos países donde los nuevos modelos aquí introducidos predicen mejor la propagación de la enfermedad que los modelos tradicionales de la familia logística.

Keywords: Complex systems modelling (Modelado de sistemas complejos); Sigmoid curves (Curvas sigmoideas); Growth models (Modelos de crecimiento); Data fitting (Ajuste de datos); Forecast (Pronóstico).

I. INTRODUCTION

S-shaped, or sigmoid curves (SC) can be found frequently in sciences, including physics and complex systems. Their ubiquity arises from their ability to approximate step-like behaviors in a continuous and differentiable manner. The S-shape is a consequence of competition between positive feedback, which tends to produce exponential growth, and negative feedback, which produces saturation or stabilization due to limiting factors. Some paradigmatic examples of SC are the Fermi-Dirac distribution function and the magnetization in a system of two-state (spin 1/2) particles.

SC are observed in a wide variety of phenomena and have a large number of applications. For example, in computational sciences [1], neuro and behavioral sciences [2–6], molecular biology [7], chemistry [8, 9], agricultural, livestock and veterinary sciences [10–14], pedology [15], ecology [16–18], economics and marketing [19, 20], electronics [21], materials engineering [22–24], spectroscopy [25] and autonomous driving [26]. An exhaustive review of more applications can be found in [27].

Applications of SC in epidemiology deserve a special mention. The cumulative number of cases in the early stages of epidemics frequently exhibits a sigmoid growth behavior. See, for example [28–44]. Sigmoid curves can be described as solutions of first-order differential equations of the form:

$$\frac{dN}{dt} = g_{\mathbf{\Pi}}(N) \tag{1}$$

where the function $g_{\mathbf{\Pi}}(N)$ with parameter vector $\mathbf{\Pi} = \{\Pi_1, \Pi_2, \cdots \Pi_k\}$ must satisfy the conditions [45]:

I. $g_{\mathbf{\Pi}}(N)$ is C^1 over the interval $[f, c]$, with $0 \leq f < c$.

II. $g_{\mathbf{\Pi}}(f) = g_{\mathbf{\Pi}}(c) = 0$.

III. $g_{\mathbf{\Pi}}(N) > 0$ if $N \in (f, c)$.

IV. $\operatorname{sgn}(g'_{\mathbf{\Pi}}(N)) = \begin{cases} 1 & \text{if} \quad N \in [f, N^*) \\ -1 & \text{if} \quad N \in (N^*, c] \end{cases}$
where $N^* \in (f, c)$.

Condition I guarantees that for each point $\Pi^* \in \mathbb{R}^k$, there exists a unique integral curve $N = N(t, \Pi^*)$ (i.e., the graph of a non-prolongable solution) of equation (1) passing through each point (t_0, N_0) of an open set contained in the strip $\mathbb{R}\times(f, c)$ (Section 4.4, Chapter 4, [46]). Property III ensures that the solution $N = N(t, \Pi^*)$ is an increasing function, while property IV implies the existence of a unique inflection point (t^*, N^*) of the solution curve that marks accelerated growth between f and N^*, and decelerated or retarded growth between N^* and c. Condition II ensures that the stationary solutions defined by the equilibrium positions f and c determine the lower and

upper limits, respectively, of the dynamics of interest. In this way, conditions (I-IV) guarantee the existence of S-shaped solutions. Furthermore, under conditions (I-IV), equation (1) only has equilibrium positions at the endpoints of the interval, and these points cannot collapse, which means that the parameters with the positiveness conditions considered in III and IV do not bifurcate.

Equation (1) is separable, so it is solvable at least for t as a function of N:

$$t - t_0 = \int_{N_0}^{N} \frac{dN}{g\Pi(N)} \tag{2}$$

where $N(t_0) = N_0$ is the initial condition. In some particular cases it is possible to obtain N as an explicit function of t.

Different analytic and numerical methods have been used to study SC [47–51].

II. THE LOGISTIC FAMILY

The simplest sigmoid growth model is the logistic model, also known as the Verhulst model [52], a two-parameter, second-order approximation of (1)

$$\frac{dN}{dt} = rN\left(1 - \frac{N}{K}\right) \tag{3}$$

Logistic model satisfies SC conditions (I-IV) for $f = 0$ and $c = K$. It exhibits an initial exponential growth with relative growth rate r and a saturation value or carrying capacity (horizontal asymptote) at $N = K$. The inflection point is $N^* = \frac{K}{2}$, which is fixed for a given value of K only. This is the main limitation of this model: more flexibility is needed for the inflection point in order to fit different datasets. In order to do that, several generalizations have been proposed as well as for flexibilizing other features of the SC [13, 53–56]. This generalization is achieved by including more parameters. In [53] a generalized five-parameter logistic model is proposed:

$$\frac{dN}{dt} = rN^{\alpha}\left(1 - \left(\frac{N}{K}\right)^{\beta}\right)^{\gamma} \tag{4}$$

where α, β and γ are positive real numbers. In what follows we shall call model (4) the Tsoularis generalized logistic model. Conditions (I-IV) are satisfied for these parameter values with $f = 0$, $c = K$ and $N^* = K(\gamma/(\gamma + \alpha\beta))^{1/\alpha}$, so the model has SC solutions. Parameter α allows non exponential initial growth, while β and γ, along with α, change the position of the inflection point. In general, α, β and γ are intended to smooth the equation (4) vector field.

Some well-known, particular cases of (4) are shown in the next table.

Model	α	β	γ
Logistic	1	1	1
Generalized Logistic	α	1	1
Richards	1	β	1
Generalized Richards	α	β	1
Gompertz	1	$\to 0$	1
Generalized Gompertz	α	$\to 0$	1

III. THE SMITH-BIRCH MODEL

A different, lesser-known kind of generalization for the logistic model was introduced by Smith [57] in order to correct problems associated with time lags in a food-limited population. Birch [58] arrived to the same result by introducing an alternative modification in the logistic model, trying to overcome some numerical unstabilities appearing in the Richards model when fitting experimental data:

$$\frac{dN}{dt} = \frac{rN(K - N)}{AN + K} \tag{5}$$

This three-parameter model reduces to the logistic model when $A = 0$ (furthermore, the case $A = -1$ corresponds to the exponential growth). When $A > 0$ Smith-Birch model satisfies conditions (I-IV) with $f = 0$, $c = K$ and $N^* = K(\sqrt{A+1} - 1)/A$, so it produces SC. In this way, A changes the position of the inflection point. In Figure 1 some solutions for this model are shown.

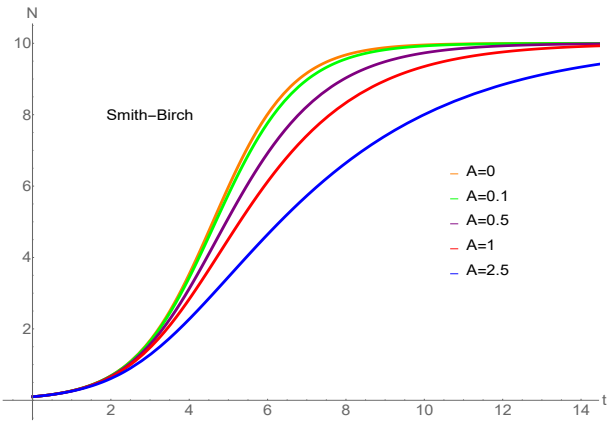

Figure 1. Smith-Birch model curves with $K = 10$, $N(0.01) = 0.1$ and $A = 0$ (orange), $A = 0.1$ (green), $A = 0.5$ (purple), $A = 1$ (red), $A = 2.5$ (blue). Inflection points correspond to $N^* = 5, 4.88, 4.49, 4.14, 3.48$, respectively.

IV. NEW SIGMOIDAL CURVES

In a previous work, partially published in [44], we applied several models of the logistic family to the time series for the cumulative number of cases during the first 61 days of the COVID 19 pandemic for 131 countries. We have found that some countries' data were not properly fitted with none of the models considered, so it is interesting to study some new, four-parameter generalizations of the Smith-Birch model:

$$\frac{dN}{dt} = \frac{rN(K-N)}{AN^p + K} \tag{6}$$

$$\frac{dN}{dt} = \frac{rN^p(K-N)}{AN + K} \tag{7}$$

which we will call Smith-Birch A and Smith-Birch B models, respectively. Both of these new models reduce to Smith-Birch when $p = 1$.

They satisfy conditions (I-III) for $A > 0$ with $f = 0$ and $c = K$. Condition IV requires a numerical analysis. Furthermore, it does not seem possible to find analytic expressions for the inflection point N^*. Hopefully, all these models, including (4), are analytically solvable for t as a function of N, using hypergeometric functions. See Appendix I for details. In Figures 2 and 3 some solutions for Smith-Birch A and Smith-Birch B models are shown.

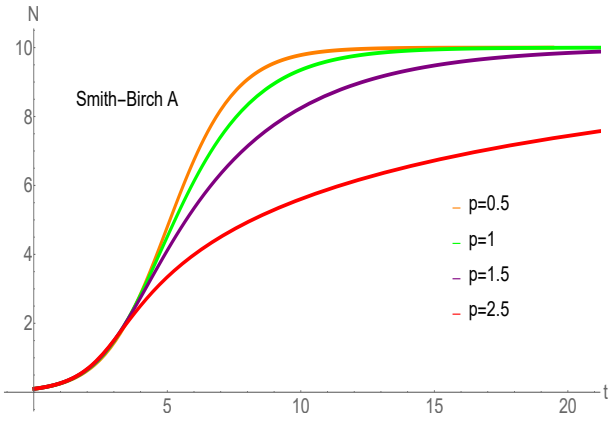

Figure 2. Smith-Birch A model curves with $K = 10$, $N(0.01) = 0.1$, $A = 1$ and $p = 0.5$ (orange), $p = 1$ (green), $p = 1.5$ (purple), $p = 2.5$ (red). Inflection points (numerically calculated) correspond to $N^* = 4.77, 4.14, 3.16, 1.82$, respectively.

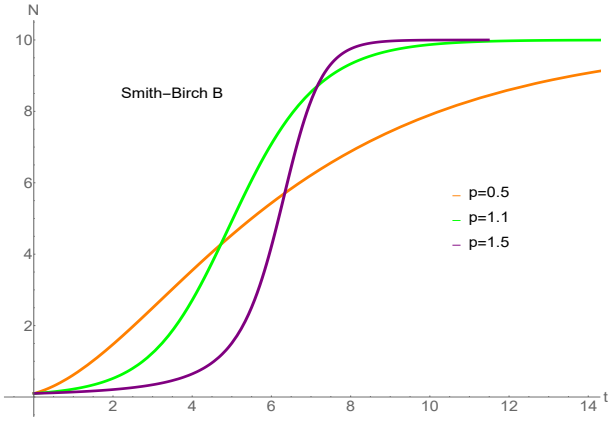

Figure 3. Smith-Birch B model curves with $K = 10$, $N(0.01) = 0.1$, $A = 0.5$ and $p = 0.5$ (orange), $p = 1.1$ (green), $p = 1.5$ (purple). Inflection points (numerically calculated) correspond to $N^* = 3.11, 5.86, 7.11$, respectively.

V. APPLICATIONS

As already mentioned, the traditional SC models listed in the table above do not fit appropriately the time series for the cumulative number of cases during the first 61 days of the COVID 19 pandemic for some countries. In these cases, Birch-Smith, Birch-Smith A or Birch-Smith B are good alternatives to resolve the problem.

The data for the adjusted curves is generated using the function `NonlinearModelFit` from the software Wolfram Mathematica to obtain the optimal values of the parameters. See Appendix II for the detailed methodology and Appendix III for some countries' optimal parameters.

In Figure 4 the results for Kiribati using several sigmoid curves are shown. In this case, the best results correspond to Birch-Smith model.

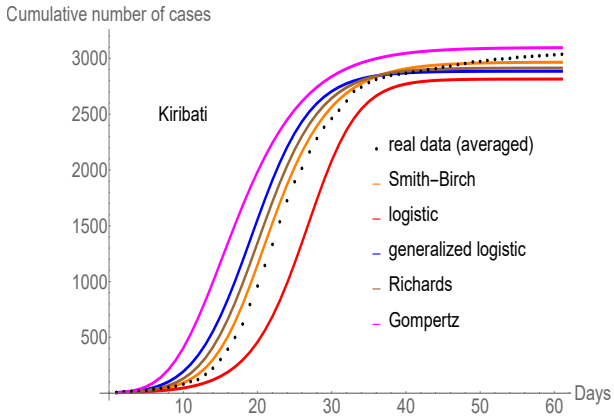

Figure 4. Results for Kiribati using several sigmoid models: Smith-Birch (orange), logistic (red), generalized logistic (blue), Richards (brown) and Gompertz (magenta). The averaged real data is shown in black dots.

In figure 5 the results for Smith-Birch model are shown separately. After the 35-day training period this model produces a good prediction for more than 10 days.

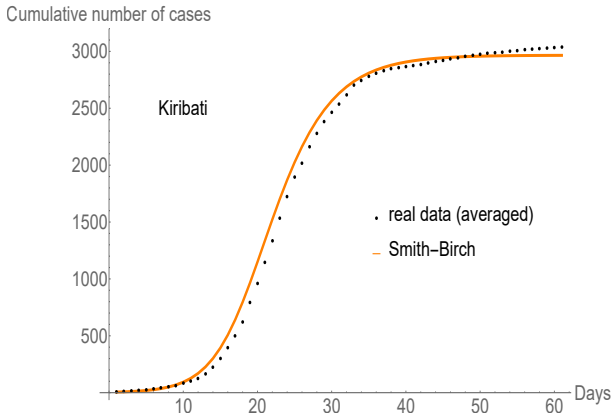

Figure 5. Smith-Birch (orange) results for Kiribati. The averaged real data is shown in black dots.

In figure 6 the results for Palau using several sigmoid models are shown. The best results correspond to Birch-Smith A model. In figure 7 the results for Smith-Birch and Smith-Birch A models are shown separately. Both models fit well during the 35-day training period, but afterwards Smith-Birch A

produces a better prediction for more than 10 days. Similar results are obtained for Somalia (figures 8 and 9).

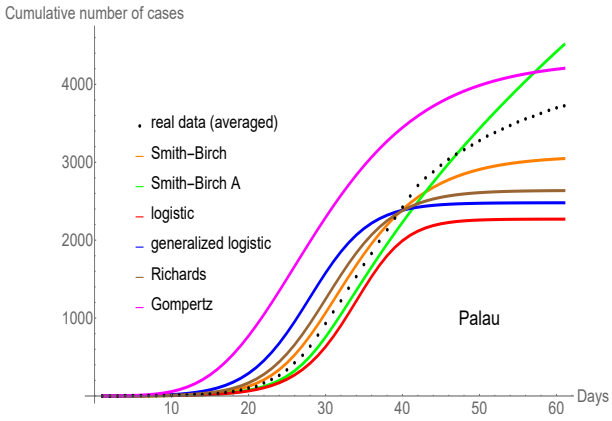

Figure 6. Results for Palau using several sigmoid models: Smith-Birch (orange), Smith-Birch A (green), logistic (red), generalized logistic (blue), Richards (brown) and Gompertz (magenta). The averaged real data is shown in black dots.

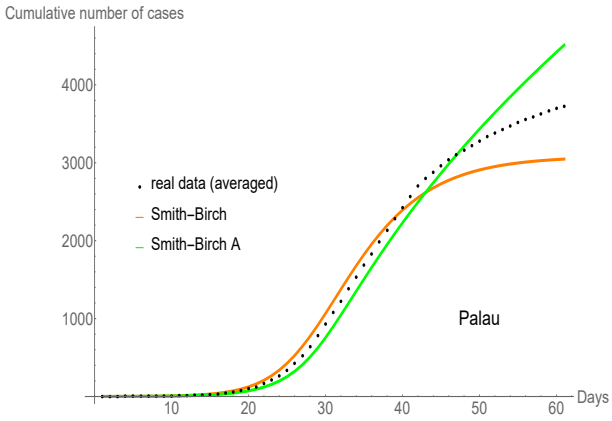

Figure 7. Smith-Birch (orange) and Smith-Birch A (green) results for Palau. The averaged real data is shown in black dots.

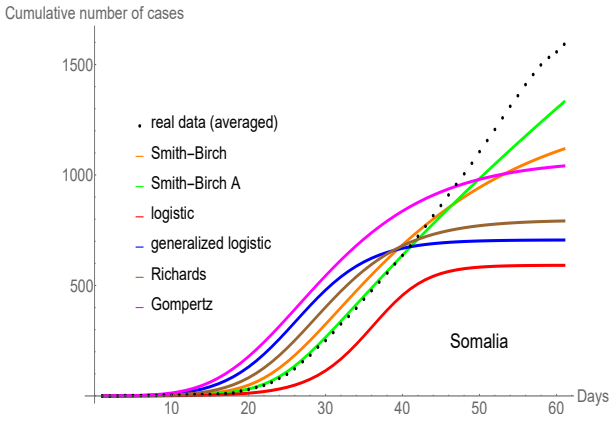

Figure 8. Results for Somalia using several sigmoid models: Smith-Birch (orange), Smith-Birch A (green), logistic (red), generalized logistic (blue), Richards (brown) and Gompertz (magenta). The averaged real data is shown in black dots.

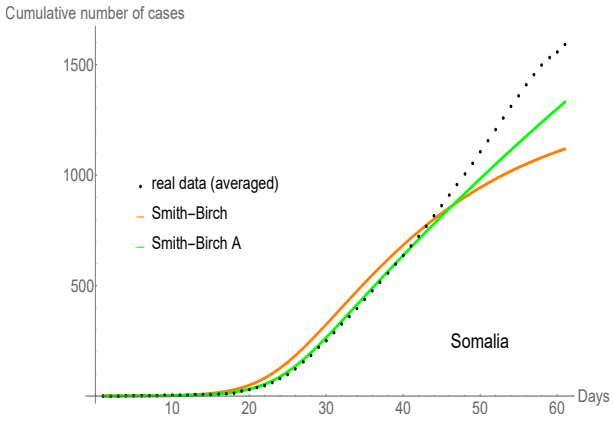

Figure 9. Smith-Birch (orange) and Smith-Birch A (green) results for Somalia. The averaged real data is shown in black dots.

Mauritius is an interesting example. As shown in Figure 10, the carrying capacity was reached in a short time. Smith-Birch A produces good results, although generalized Richards is the best model in this case. Smith-Birch, on the contrary, is a bad choice. In Figure 11 this curves are shown separately.

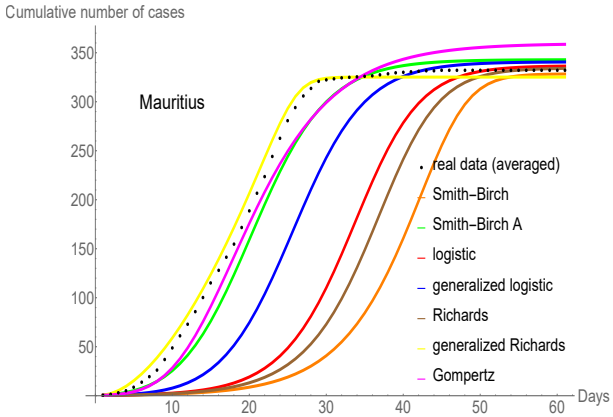

Figure 10. Results for Mauritius using several sigmoid models: Smith-Birch (orange), Smith-Birch A (green), logistic (red), generalized logistic (blue), Richards (brown), generalized Richards (yellow) and Gompertz (magenta). The averaged real data is shown in black dots.

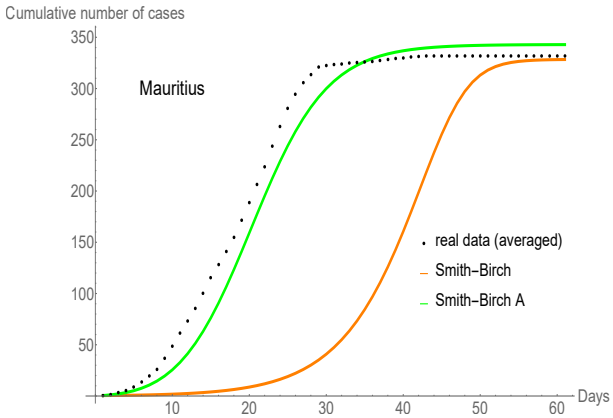

Figure 11. Smith-Birch (orange) and Smith-Birch A (green) results for Mauritius. The averaged real data is shown in black dots.

In [44] it was proven by an statistical analysis that for Cuba data the best model is generalized Gompertz. However, it is interesting to evaluate the performance of Smith-Birch

models in this case. Figures 12 and 13 show good results for Smith-Birch A model, although Smith-Birch and Smith-Birch B results are not satisfactory.

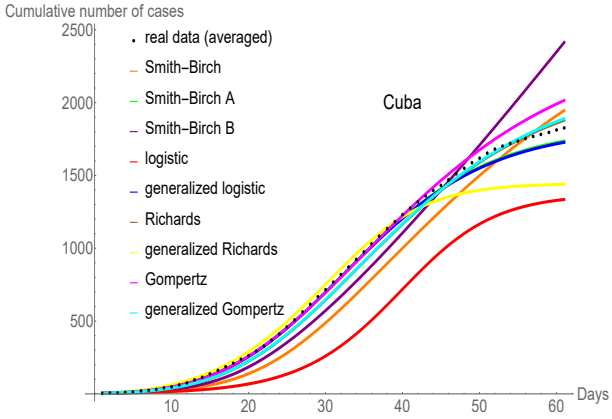

Figure 12. Results for Cuba using several sigmoid models: Smith-Birch (orange), Smith-Birch A (green), Smith-Birch B (purple), logistic (red), generalized logistic (blue), Richards (brown), generalized Richards (yellow), Gompertz (magenta) and generalized Gompertz (cyan). The averaged real data is shown in black dots.

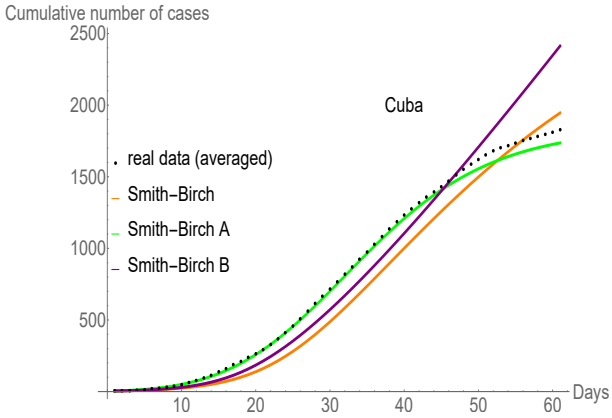

Figure 13. Smith-Birch (orange), Smith-Birch A (green) and Smith-Birch B (purple) results for Cuba. The averaged real data is shown in black dots.

The results for Cambodia using several sigmoid models are shown in Figure 14. In this case, the best model is Smith-Birch B. In Figure 15 it is shown separately, along with Smith-Birch (for comparison).

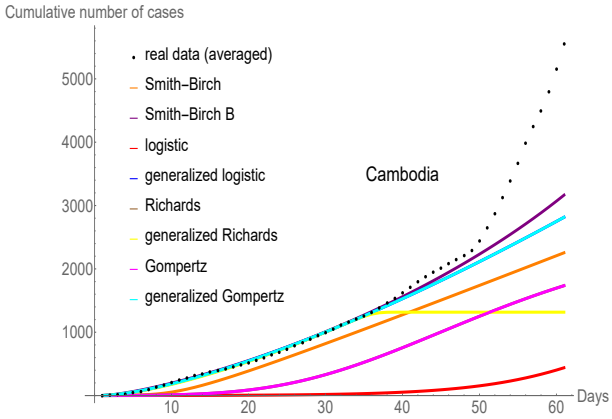

Figure 14. Results for Cambodia using several sigmoid models: Smith-Birch (orange), Smith-Birch B (purple), logistic (red), generalized logistic (blue), Richards (brown), generalized Richards (yellow), Gompertz (magenta) and generalized Gompertz (cyan). The averaged real data is shown in black dots.

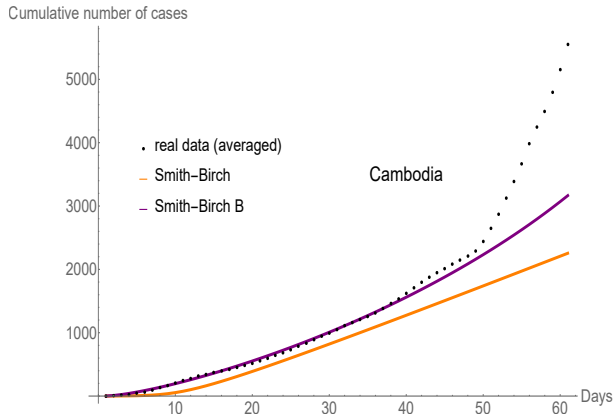

Figure 15. Smith-Birch (orange) and Smith-Birch B (purple) results for Cambodia. The averaged real data is shown in black dots.

VI. CONCLUSIONS

Two new, four-parameter sigmoid curves are introduced, as generalizations of the Smith-Birch model, a member of the logistic family. Analytic and numerical description of these two models are presented. The applicability of the new models for predicting early dynamics of infectious diseases is shown in the case of epidemiologic data from the COVID-19 pandemic in countries where traditional models failed to predict. Due to the wide variety of phenomena which can be described using sigmoid curves, further applications in other areas can be expected, for example, prediction curves of any kind as envelopes of sigmoid curves.

VII. ACKNOWLEDGEMENTS

MTPM acknowledges financial support from COIC/STIA/10104 /2024 and PAPIIT DGAPA UNAM IN101822 projects and hospitality received at Unidad Académica del IIMAS en el Estado de Yucatán, Universidad Nacional Autónoma de México. JBC appreciates the support of the PROEC/UFS/Brazil through the PRAPG Program No. 23038.003836/2023-39 of the Coordination for the Improvement of Higher Level Personnel (CAPES).

VIII. APPENDIX I: ANALYTIC SOLUTIONS FOR THE TSOULARIS GENERALIZED LOGISTIC, SMITH-BIRCH, SMITH-BIRCH A AND SMITH-BIRCH B MODELS

The Tsoularis generalized logistic model (4) with the initial condition $N(t_0) = N_0$ has the solution

$$r(t-t_0) = \begin{cases} \frac{1}{\beta\gamma}\left(\frac{1-\left(\frac{N}{K}\right)^{-\beta}}{1-\left(\frac{N}{K}\right)^{\beta}}\right)^{\gamma} F(\gamma,\gamma,\gamma+1,\left(\frac{N}{K}\right)^{-\beta})\Big|_{N_0}^{N} \\ \qquad\qquad \text{if } \alpha = 1 \\ \frac{N^{1-\alpha}}{\alpha-1} F(\frac{1-\alpha}{\beta},\gamma,1+\frac{1-\alpha}{\beta},\left(\frac{N}{K}\right)^{\beta})\Big|_{N_0}^{N} \\ \qquad\qquad \text{if } \alpha \neq 1 \end{cases} \tag{8}$$

where

$$F(a,b,c,z) = \frac{\Gamma(c)}{\Gamma(a)\Gamma(b)} \sum_{n=0}^{\infty} \frac{\Gamma(a+n)\Gamma(b+n)}{\Gamma(c+n)} \frac{z^n}{n!} \tag{9}$$

is the hypergeometric function [59].

The Smith-Birch A model (6) with the initial condition $N(t_0) = N_0$ has the solution

$$r(t-t_0) = \left(\frac{A}{Kp} N^p F(1,p,1+p,\frac{N}{K}) + \ln\left(\frac{N}{K-N}\right) \right)\Big|_{N_0}^{N} \tag{10}$$

The Smith-Birch B model (7) with the initial condition $N(t_0) = N_0$ has the solution

$$r(t-t_0) = \begin{cases} \ln\left(\frac{N}{(K-N)^{A+1}}\right)\Big|_{N_0}^{N} & \text{if } p = 1 \\ \left(\frac{A+1}{K}\ln\left(\frac{N}{K-N}\right) - \frac{1}{N}\right)\Big|_{N_0}^{N} & \text{if } p = 2 \\ \left(\frac{A}{K(2-p)} N^{2-p} F(1,2-p,3-p,\frac{N}{K}) + \right. & \\ \left. + \frac{1}{1-p} N^{1-p} F(1,1-p,2-p,\frac{N}{K})\right)\Big|_{N_0}^{N} & \text{if } p \neq 1,2 \end{cases} \tag{11}$$

It should be noted that the solution of the Smith-Birch model (5) is included in (10) and (11) when $p = 1$.

IX. APPENDIX II: METODOLOGY FOR TIME SERIES ANALYSIS

As the number of cases is typically reported at regular time intervals (daily, weekly, etc.), it is reasonable to use mathematical models whose solutions are defined over time discrete domains, so we will use discrete difference equations, instead of first-order differential equations on a continuous time domain, for describing the dynamics of the disease. A classical review on the theoretical and applied scope of first-order difference equations can be found in [60]. A didactic introduction to the study of these equations appears, for instance, in [61].

The standard way of obtaining a difference equation from a continuous one is through the transformation:

$$N(t) \to N_i, \quad \frac{dN}{dt} \to \frac{N_{i+1} - N_i}{h}, \tag{12}$$

where i represents the i-th value of the time series of n_0 length $\{N_i\}_{i=1}^{n_0}$ and h is the time step between recorded values (we are assuming that it is constant). The next steps are

1. The time series $\left\{N_i^0\right\}_{i=1}^{n_0}$ is averaged with a 7 day long moving window, resulting in the time series $\{N_i\}_{i=1}^{n}$, where $n = n_0 - 6$. This smoothing has the effect of eliminating factors like delays in reporting due to the accumulation of unreported cases. This kind of window averaging has been used before in COVID-19 literature [62].

2. From the time series $\{N_i\}_{i=1}^{n}$ the first n_1 elements are used to train each model (calibration period) and form the list of pairs $\{(N_i, N_{i+1})\}_{i=1}^{n_1-1}$.

3. The list of pairs is fitted to the model $Y = X + hg_{\mathbf{\Pi}}(X,i)$, by using the function `NonlinearModelFit` from the software Wolfram Mathematica. From here we obtain the optimal values of the parameters and store them as components of the optimal parameters vector $\mathbf{\Pi}^\star$.

4. The predicted time series $\left\{N_i^\star\right\}_{i=1}^{n}$ is computed through the `RecurrenceTable` function using the optimal values $\mathbf{\Pi}^\star$ and $N_1^\star = N_1$.

X. APPENDIX III: OPTIMAL VALUES FOR THE PARAMETERS FOR SOME COUNTRIES.

Palau:

Model	r	K	A	p
Smith-Birch	0.33	3082.82	1.43	–
Smith-Birch A	0.29	$1.65 \cdot 10^6$	6.07	1.80

Cambodia:

Model	r	K	A	p
Smith-Birch	1.67	13399.3	599.63	–
Smith-Birch B	8.82	$1.37 \cdot 10^{15}$	$1.81 \cdot 10^{11}$	0.23

REFERENCES

[1] V. Vieira, *Comput. ecol. softw.* **10**, 162 (2020).
[2] F. H. Eeckman and W. J. Freeman, *Brain Res.* **557**, 13 (1991).
[3] K. Sandberg, B. M. Bibby, B. Timmermans, A. Cleeremans, and M. Overgaard, *Conscious. Cogn.* **20**, 1659 (2011).
[4] D. R. F. Paul E. Smaldino, Lucy M. Aplin, *Sci. Rep.* **8**, 14015 (2018).
[5] J. M. J. Murre, *Psychon. Bull. Rev.* **21**, 344 (2014).
[6] C. L. T. D. Tab Rasmussen, *J. Hum. Evol.* **23**, 159 (1992).
[7] H. Qiu, K. Durand, H. Rabinovitch-Chable, M. Rigaud, V. Gazaille, P. Clavère, and F. G. Sturtz, *Biotechniques* **42**, 355 (2007).
[8] S. Pixton and R. Howe, *J. Stored. Prod. Res.* **19**, 1 (1983).
[9] A. G. A. Anna M. Michałowska-Kaczmarczyk and Tadeusz Michałowski, *J. Anal. Sci.*, Methods and Instrumentation **4**, 27 (2014).
[10] C. Y. Hsieh, S. L. Fang, Y. F. Wu, Y. C. Chu, and B. J. Kuo, *Hortic.* **7**, 537 (2021).

[11] S. H. Austin, T. R. Robinson, W. D. Robinson, and R. E. Ricklefs, *Methods Ecol. Evol.* **2**, 43 (2011).
[12] M. Michalczu, K. Damaziak, and A. Goryl, *Ann. Anim. Sci.* **16**, 65 (2016).
[13] L. Cao, P.-J. Shi, L. Li, and G. Chen, *Symmetry* **11**, 204 (2019).
[14] T. Onoda, R. Yamamoto, K. Sawamura, Y. Inoue, A. Matsui, T. Miyake, and N. Hirai, *J. Equine Sci.* **22**, 37 (2011).
[15] Y. Zhang, A. Biswas, and V. I. Adamchuk, *Geoderma* **289**, 1 (2017).
[16] K. Hufkens, R. Ceulemans, and P. Scheunders, *Ecol. Inform.* **3**, 97 (2008).
[17] B. G. Akre and D. M. Johnson, *J. Anim. Ecol.* **48**, 703 (1979).
[18] J. I. Lehr Brisbin and M. C. Newman, *Water Air Soil Poll* **57-58**, 691 (1991).
[19] L. A. Kuznar and W. G. Frederick, *Ecol. Econ.* **46**, 296 (2003).
[20] I. McGowan, *The Statistician* **35**, 73 (1985).
[21] K. Kobayashi, W. A. Borders, S. Kanai, K. Hayakawa, H. Ohno, and S. Fukami, *Appl. Phys. Lett.* **119**, 132406 (2021).
[22] D. S. Paolino and M. P. Cavatorta, *Fatigue Fract. Engng. Mater. Struct.* **36**, 316 (2012).
[23] M. El-Khawaga, S. El-Badawy, and A. Gabr, *Arabian J. Sci. Eng.* **45**, 3973 (2020).
[24] S. Mastilović, *Theor. Appl. Mech.* **45**, 95 (2018).
[25] D. Jang, G. Chae, and S. Shin, *Sens.* **15**, 25385 (2015).
[26] B. Lu, H. He, H. Yu, H. Wang, G. Li, M. Shi, and Dongpu, *Sens.* **20**, 7197 (2020).
[27] D. Kucharavy and R. D. Guio, *Procedia Eng.* **9**, 559 (2011).
[28] R. Bürger, G. Chowell, and L. Y. Lara-Díaz, *Math. Biosci.* **334** (2021), ISSN 18793134.
[29] F. Brauer, C. Castillo-Chavez, and Z. Feng, *Mathematical Models in Epidemiology*, Texts in Applied Mathematics (Springer, New York, NY, 2019).
[30] G. Zhou and G. Yan, *Emerg. Infect. Dis.* **9** (2003), ISSN 10806040.
[31] B. Pell, Y. Kuang, C. Viboud, and G. Chowell, *Epidemics* **22** (2018), ISSN 18780067.
[32] D. W. Shanafelt, G. Jones, M. Lima, C. Perrings, and G. Chowell, EcoHealth **15** (2018), ISSN 16129210.
[33] L. Dinh, G. Chowell, K. Mizumoto, and H. Nishiura, *Theor. Biology Med. Model.***13** (2016), ISSN 17424682.
[34] S. Zhao, S. S. Musa, H. Fu, D. He, and J. Qin, *Parasit. Vectors.* **12** (2019), ISSN 17563305.
[35] B. Malavika, S. Marimuthu, M. Joy, A. Nadaraj, E. S. Asirvatham, and L. Jeyaseelan, *Clin. Epidemiol. Glob. Health.* **9** (2021), ISSN 22133984.
[36] C. Y. Shen, IJID **96** (2020), ISSN 18783511.
[37] K. Wu, D. Darcet, Q. Wang, and D. Sornette, *medRxiv* (2020).
[38] G. L. Vasconcelos, A. M. Macêdo, R. Ospina, F. A. Almeida, G. C. Duarte-Filho, A. A. Brum, and I. C. Souza, *PeerJ* **2020** (2020), ISSN 21678359.
[39] K. Roosa, Y. Lee, R. Luo, A. Kirpich, R. Rothenberg, J. M. Hyman, P. Yan, and G. Chowell, *J. Clin. Med.* **9** (2020), ISSN 20770383.
[40] K. Roosa, Y. Lee, R. Luo, A. Kirpich, R. Rothenberg, J. M. Hyman, P. Yan, and G. Chowell, *Infect. Dis. Model.* **5** (2020), ISSN 24680427.
[41] Y. Wu, L. Zhang, W. Cao, X. Liu, and X. Feng, *Front. Phys.* **8**, 566 (2021), ISSN 2296-424X.
[42] M. López, A. Peinado, and A. Ortiz, *PLoS ONE* **16** (2021), ISSN 19326203.
[43] P. Pincheira-Brown and A. Bentancor, *Epidemics* **37** (2021), ISSN 18780067.
[44] M. T. Pérez-Maldonado, J. Bravo-Castillero, R. Mansilla, R. O. Caballero-Pérez, *Nova scientia* **14**, 18 (2022).
[45] G. Jarne, J. Sanchez-Choliz, F. Fatas-Villafranca, *Evol. Inst. Econ. Rev.* **3**, 239 (2007).
[46] L. S. Pontriaguin, *Ecuaciones Diferenciales Ordinarias* (Editorial Pueblo y Educación, La Habana, 1981).
[47] M. Carrillo, J. M. González, *Technol. Forecasting Social Change* **69**, 233 (2002).
[48] W. G. Bardsley, R. E. Childs, *Biochem. J.* **149**, 313 (1975).
[49] Z. Li, B. S. Yang Zhang, Z. Xing, Q. Wang, *Electronics* **11**, 1365 (2022).
[50] R. Gomeni, C. Gomeni, *Comput. Biomed. Res.* **13**, 489 (1980).
[51] H. Li, X. Jiang, G. Huo, C. Su, B. Wang, Y. Hu, Z. Zheng, nt. *J. Adv. Manuf. Technol.* **119**, 1531 (2022).
[52] P. Verhulst, *Corr. Math. Physics* **10**, 113 (1838).
[53] A. Tsoularis, J. Wallace, *Math. Biosci.* **179** (2002), ISSN 00255564.
[54] M. H. Zwietering, I. Jongenburger, F. M. Rombouts, K. van't Riet, *Appl. Environ. Microbiol.* **56**, 1875 (1990).
[55] J. Schnute, *Can. J. Fish. Aquat. Sci.* **38**, 1128 (1981).
[56] K. M. C. T. Erve , E. T. Erve, *Ecol. Modell.* **359**, 117 (2017).
[57] F. E. Smith, *Ecol.* **44**, 651 (1963).
[58] C. P. D. Birch, *Ann. Bot.* **83**, 713 (1999).
[59] M. Abramowitz, I. A. Stegun, *Handbook of Mathematical Functions with Formulas, Graphs, and Mathematical Tables* (Dover, New York, 1964), ninth dover printing, tenth gpo printing edition.
[60] R. M. May, *Nature* **261**, 459 (1976), ISSN 20522541.
[61] W. E. Boyce, R. C. DiPrima, *Elementary Differential Equations* (John Wiley & Sons, Inc., Hoboken, NJ, 2012).
[62] A. L. M. J. A. Mesejo-Chiong, Ciencias Matemáticas **34**, 19 (2020).

COMPUTATIONAL OPTIMIZATION OF A STOCHASTIC MODEL FOR SIMULATING APOPTOTIC SIGNALINGT

OPTIMIZACIÓN COMPUTACIONAL DE UN MODELO ESTOCÁSTICO PARA LA SIMULACIÓN DE LA SEÑALIZACIÓN APOPTÓTICA

J. German-Serra[a†], N. López-Marín[a]

Faculty of Physics, University of Havana, La Habana, Cuba; jorge.german@fisica.uh.cu[†]
† corresponding author

Recibido 30/1/2025; Aceptado 30/6/2025

The development of mathematical models to simulate biological processes is essential for understanding the complexity of living systems, allowing for predictions and virtual experiments that would be difficult to carry out under real conditions. In this work, we present a mathematical model to simulate the process of apoptosis or programmed cell death, using the Gillespie algorithm. Additionally, an optimization of this model is proposed, which reduces computation time and enables the model to simulate apoptosis in the cells of a tumor under topical treatment. Results are also presented demonstrating that both models are equivalent. The optimization reduced the execution time of the simulation by two days.

El desarrollo de modelos matemáticos para simular procesos biológicos es fundamental para comprender la complejidad de los sistemas vivos, permitiendo hacer predicciones y realizar experimentos virtuales que serían difíciles de llevar a cabo en condiciones reales. En el presente trabajo presentamos un modelo matemático para simular el proceso de apoptosis o muerte programada en una célula, utilizando el algoritmo de Gillespie. Se propone además, una optimización de este modelo, que permite disminuir el tiempo de cálculo y utilizar el modelo para simular la apoptosis en las células de un tejido tumoral que fue sometido a un tratamiento tópico. Se presentan además resultados que demuestran que ambos modelos son equivalentes. La optimización permitió disminuir el tiempo de ejecución de la simulación en dos días.

Keywords: Stochastic models (modelos estocásticos); Complex systems (sistemas complejos); Computer modeling (modelado computacional); Monte Carlo methods (métodos de Monte Carlo); Systems biology (biología de sistemas).

I. INTRODUCTION

Apoptosis, or programmed cell death, is a vital biological process that facilitates the controlled elimination of unnecessary or damaged cells. This mechanism plays a crucial role in maintaining a stable internal environment, even in the face of external changes, and ensures the proper functioning of the tissues. Dysregulation of apoptosis is associated with various diseases, particularly neurodegenerative disorders and cancer. In cancer, malignant cells often develop the ability to evade apoptosis, allowing them to survive and proliferate uncontrollably. Understanding the complex mechanisms that govern apoptosis and its disruptions is essential to develop targeted therapies. These therapies aim to reactivate apoptotic pathways, promoting the selective death of cancer cells while minimizing damage to normal tissues, ultimately enhancing the efficacy of treatment and improving patient outcomes [1–7].

Given the high costs associated with developing less invasive and more effective treatments, mathematical modeling of apoptosis presents a promising tool to increase our understanding of this cellular process. Specifically, computational algorithms that efficiently simulate all biochemical interactions within cells can provide valuable insights into the behavior of cancer and other diseases. Using these models, researchers can better predict outcomes and tailor therapies to individual patient needs. Various mathematical models used to simulate apoptosis are based on different approaches, including agent-based models [8–10], Boolean networks [11, 12] , differential equations [14–16], and stochastic methods grounded in Monte Carlo simulations using their own algorithms or the Gillespie algorithm [17–19].

In the study of physical systems where randomness is fundamental, traditional deterministic methods often prove insufficient. In these cases, the Gillespie algorithm, originally developed to model stochastic chemical reactions, becomes highly relevant in physics. This algorithm enables accurate simulation of discrete, random processes over time, including phenomena such as particle diffusion [20] , molecular population dynamics [21], and the evolution of non-equilibrium systems. Its versatility makes it a powerful tool in fields like statistical physics, biophysics, and materials science, especially when microscopic fluctuations have significant macroscopic consequences.

In this work, we present a mathematical model of cell death by apoptosis that incorporates the internal dynamics of biochemical species within the cell. In addition, we introduce an optimized version of the model, demonstrating results that validate its accuracy and equivalence. We apply this enhanced model to simulate apoptosis in cells of an epithelial tumor undergoing topical treatment and present the results of these simulations.

II. METHODS

II.1. Apoptosis model

The activation of the intrinsic pathway of apoptosis illustrated in Figure 1. This process begins with the permeabilization of the mitochondria, which leads to the release of cytochrome C (CytC) into the cytoplasm. The regulation of mitochondrial membrane permeabilization involves the Bcl-2 protein family, which can promote or inhibit apoptosis by directly influencing channels in the outer mitochondrial membrane. Specifically, Bax facilitates the formation of pores, while Bcl-2 acts to inhibit it. Once cytochrome C is released into the cytoplasm, it triggers the assembly of a multiprotein complex known as the apoptosome, which subsequently activates the caspase cascade via caspase-9 (C9), resulting in cell death by apoptosis. Additionally, after membrane permeabilization, the SMAC protein (Second Mitochondria-derived Activator of Caspases) is released into the cytoplasm, where it binds to inhibitors of apoptosis (XIAPs). This binding prevents XIAPs from stopping the apoptotic process, allowing apoptosis to progress [22].

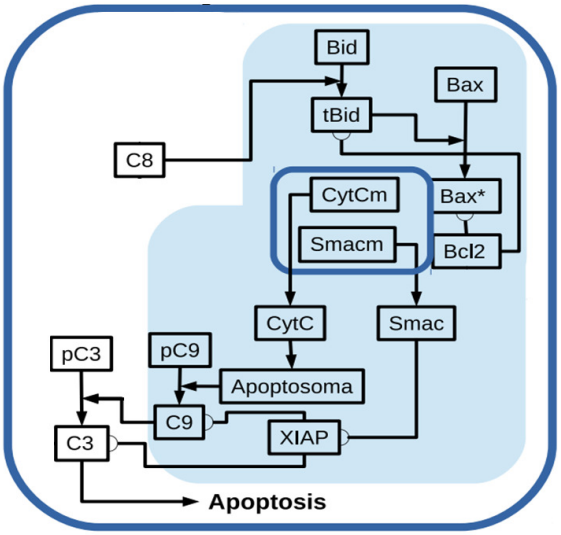

Figure 1. Intrinsic pathway of apoptosis activation. Cell degradation by apoptosis begins when Caspase 3 (C3) is activated. The intrinsic pathway is shaded in blue and begins when pores open in the mitochondrial membrane, and Cytochrome C (CytC) and SMASCs are released into the cytosol. Cytochrome C forms a protein complex, Apoptosome, which activates C3 through C9. The Bcl-2 protein family regulates the formation of pores in the mitochondrial membrane: Bax and/or Bak, represented by Bax in the model, are responsible for the formation of the pores, while Bcl-2, Bcl-xL, or Mcl-1, represented by Bcl-2, inhibit it.

The Gillespie algorithm was used to simulate cell death by apoptosis. This is a stochastic simulation method designed to model the time evolution of chemical reactions in systems with a finite number of molecules. The algorithm captures the inherent randomness of the reaction events by simulating the waiting times between reactions and determining which reaction occurs next on the basis of their rates. It operates under the Markovian assumption, meaning that the future state of the system depends only on its current state. Using exponential distributions to model waiting times and random sampling to select reactions, the Gillespie algorithm effectively simulates complex biochemical processes [23,24].

Table 1. Reactions that participate in the intrinsic pathway

No	Reaction
1	C8 + Bid → C8:Bid
2	C9 + Bid → C9:Bid
3	Bid + Bax → Bid:Bax
4	Bid:Bax → tBid + Bax
5	tBid + Bax → tBid:Bax
6	tBid:Bax → tBid + Bax
7	Bid2 + Bax → Bid2:Bax
8	Bid2:Bax → Bid2 + Bax
9	Cytc + Apaf → Apop
10	Apop + pC9 → Apoptosome:2pC9
11	Apoptosome:2pC9 → Apop + 2pC9
12	C9 + C9 → C9:C9
13	C9:C9 → C9 + C9
14	XIAP + Smac → XIAP:Smac
15	XIAP:Smac + pC9 → XIAP:pC9
16	XIAP:pC9 → XIAP + pC9
17	Apaf + Apaf → Apaf:Apaf
18	Apaf:Apaf → Apaf + Apaf
19	Cytc + CytC → Cytc:CytC
20	Smac → Smac

The interactions within the intrinsic pathway of apoptosis, as depicted in Figure 1, are represented through the reactions listed in Table 1 and the corresponding molecules in Table 2. The rate constants for these reactions (K) were obtained from the literature [25,26]. These reactions take place inside the cell, specifically in the cytoplasm, which is assigned a volume of $\Omega = 1000\mu m^3$, reflecting the typical cytoplasmic volume. The model assumes that a healthy cell maintains an equilibrium among the concentrations of molecules such as Bid, Bax, Bcl-2, and the complexes Bcl2:tBid and Bcl2:Bax. Under these conditions, the levels of tBid and activated Bax are sufficiently low to prevent apoptosis. However, if this equilibrium is disrupted, the concentration of tBid rises, leading to cell death. To simulate this scenario, the initial concentration of tBid is set to a value greater than zero, and this value is proportional to the apoptotic signal. The model also considers that when the concentration of activated Bax reaches the threshold value of $10nM$, pores are formed in the mitochondrial membrane, activating reactions 19 and 20 from Table 1. Finally, the cell is considered dead when the Caspase-3 concentration reaches $10nM$.

All simulations were developed in the C programming language[1] and executed on a personal Asus computer equipped with an Intel® Celeron® CPU N3050, running at 1.60 GHz, with 4 GB of RAM and a 64-bit operating system.

II.2. Optimization of the apoptosis model

The simulation of apoptosis in a single cell takes approximately 7 seconds on the computer used for these calculations. To simulate apoptosis in a tissue composed of

[1] Although not publicly archived, the simulation code supporting this study will be made available to researchers upon formal request to the corresponding author

millions of cells, it is crucial to minimize this time as much as possible. This can be achieved either by using a more powerful computer or by optimizing the model for greater efficiency.

Table 2. Molecules and initial concentrations used in the model of cell death by apoptosis using the Gillespie algorithm.

Symbol	Description	$\mathbf{X}_0$ (nM)
$C8$	Active form of Caspase-8	0
Bid	BH3-binding domain death agonist	25
$C8 : Bid$	Complex of C8 with Bid	0
$C9 : Bid$	Complex of C9 with Bid	0
$pC3$	Procaspase-3, inactive	100
$C8 : p3$	Complex of Caspase-8 with procaspase-3	0
$C3$	Active form of Caspase-3	0
$C9 : pC3$	Complex of C9 with procaspase-3	0
$Apaf$	Activating Factor (Apaf-1)	80
$pC9$	Inactive form of Apoptosome-9	20
$Apop$	Apoptosome complex	0
$Apoptosome : 2pC9$	Complex of Apoptosome with 2 procaspase-9	0
$C9 : C9$	Complex of C9 with C9	0
$XIAP : Smac$	X-linked Inhibitor of Apoptosis	30
$XIAP : pC9$	Complex of XIAP with procaspase-9	0
$XIAP : C9$	Complex of XIAP with caspase-9	0
$Apaf : Apaf$	Complex of Apaf-1 dimer	0
$Cytc : CytC$	Cytochrome c inside the mitochondria	50
$Smac$	SMAC inside the mitochondria	50

The reactions that lead to the permeabilization of the mithochondrial membrane are more time consuming in the simulation. For this reason, we propose to eliminate the reactions [3−7] shown in Table 1 and replace them with a single reaction. This new reaction has tBid and Bax as reactants, tBid and activated Bax as products, and K as the rate constant of the optimized reaction (Figure 2). The new rate constant was chosen so that the time to permeabilize the membrane would be the same for both models. We used the original apoptosis model to determine the opening times of the mitochondrial membrane (t_{org}). Subsequently, using the optimized model, we change the parameter K to obtain the opening time of the membrane (t_i) for each value of K. Finally, we selected $K = K_i$ that corresponded to the t_i closest to t_{org}.

The strength of the apoptotic signal is directly proportional to the initial concentration of tBid, as previously discussed. In contrast, the initial concentration of Bcl2 influences membrane permeabilization but is not included in the reaction of the optimized model. To address this limitation, we calculated the values of K for various initial concentrations of these molecules, denoted as $[tBid_0]$ and $[Bcl2_0]$. This dependence requires the application of the previously described method each time these initial concentrations change, which is inefficient given our goal of applying this optimized model to a heterogeneous epithelial cell tumor, where cells exhibit varying initial concentrations of all molecules.

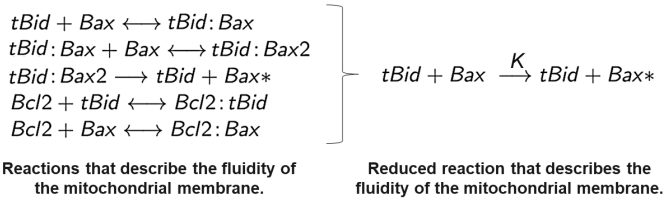

Figure 2. Reactions that permeabilize the mitochondrial membrane (left) and the resulting reaction in the optimized model (right).

To improve efficiency, we develop a matrix of K values for every combination of $[tBid_0]$ and $[Bcl2_0]$. We defined a range for initial tBid concentrations from $25nM$ to $2510nM$ with increments of approximately $38nM$, and for initial Bcl2 concentrations from $40nM$ to $60nM$ with increments of $5nM$. Consequently, we calculated the values of K for each combination, which resulted in a matrix with 67 rows and 21 columns. This matrix can be used in simulations involving multiple cells with different initial concentrations of the aforementioned molecules.

II.3. Simulation of apoptosis in an epithelial tumor

Using the optimized model of apoptosis, we successfully simulated an epithelial tumor after topical treatment. The tumor is modeled as a three-dimensional matrix of **m** layers deep and in each layer **n × n** cells. In this case, we modeled 6 layers of 100×100 cells each.

This model operates under the assumption that drug concentration decreases exponentially with increasing tumor depth. Since the initial concentration of tBid is directly related to the apoptotic signal, we modeled a tumor with a depth of $1mm$, where the initial concentration of tBid ($[tBid_0]$) decreases exponentially with depth. To incorporate cellular variability, we assumed that the initial levels of the relevant proteins differ between individual cells. The initial concentrations of these proteins were uniformly distributed around their mean values (see Table 2), with a variance of 20 %.

These simulations were performed on an Intel i7 computer with 12 cores and 16GB of RAM.

III. RESULTS AND DISCUSSION

III.1. Optimization of mithochondrial membrane permeabilization reactions

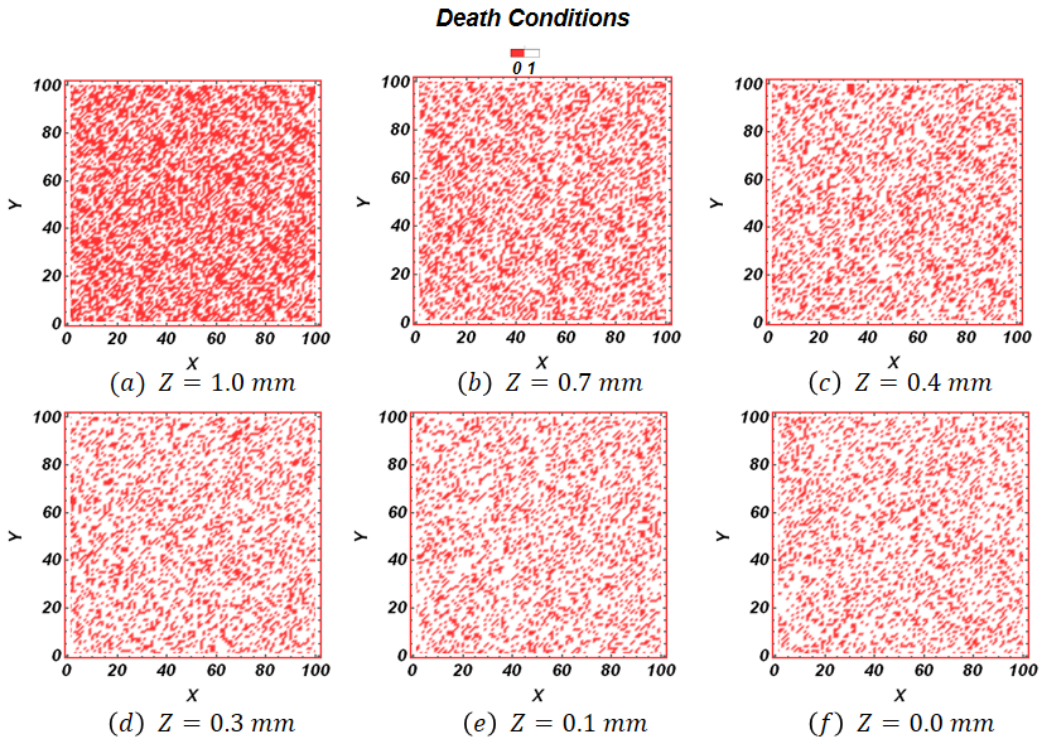

Figure 3. Cell survival matrices at different tumor depths after topical treatment of an epithelial tumor. The tumor is modeled as a three-dimensional matrix consisting of six layers, each containing 100×100 cells. Cell death by apoptosis was simulated: cells that died within 3500 seconds after treatment are shown in red, while surviving cells are shown in white.

In the apoptosis model, the mitochondrial membrane becomes permeabilized, leading to the release of CytC and SMASCs into the cytosol when the concentration of activated Bax reaches $10nM$, approximately 12040 molecules. To validate the functionality of the optimized model, we compare the time at which activated Bax reaches this threshold. Figure 4 shows only the first 200 seconds of the simulation in which the membrane opening occurred to demonstrate that in both models the time at which activated Bax reaches the membrane opening threshold concentration is quite similar, indicating that the two models are equivalent and confirming the precision of the determined value of K.

In the apoptosis model, mitochondrial membrane permeabilization occurs when activated Bax concentration reaches 10 nM (~ 12040 molecules), triggering the release of cytochrome c (CytC) and SMASCs into the cytosol. To validate the optimized model's functionality, we compared the time at which activated Bax reaches this threshold. Figure 4 displays the initial $200s$ of the simulations, demonstrating comparable threshold attainment times in both models. This kinetic equivalence confirms the consistency of the model and validates the determined parameter K.

III.2. Influence of Initial Concentrations of Bcl-2 and tBid on the Kinetic Constant of the reaction

We calculated K values for various initial concentrations of tBid and Bcl-2. Figure 5 presents the density plot of the resulting matrix. In particular, when the initial concentration of tBid exceeds $137nM$, K becomes independent of the initial concentration of Bcl-2.

We initially performed a tumor simulation on a small scale. In this model, the tumor is represented as a three-dimensional array consisting of 67 layers, each layer corresponding to a specific value of $[tBid_0]$ in the K matrix calculated previously. Within each layer, we simulate cell death by apoptosis for 100 cells arranged in a 10 x 10 grid.

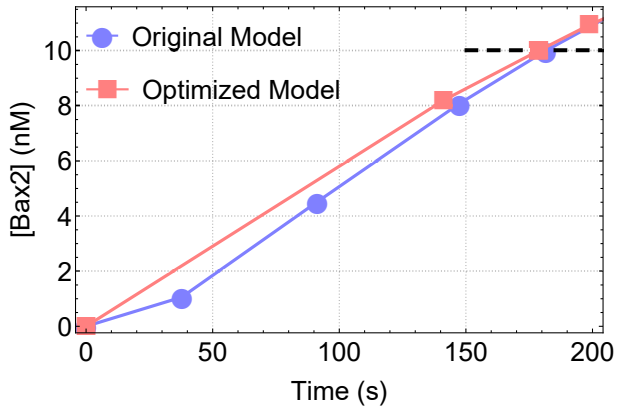

Figure 4. Activated Bax concentration as a function of time for both models. The black dashed line at 10 nM indicates that the times of mitochondrial membrane permeabilization are similar.

The initial concentrations of the other proteins involved in the apoptosis process varied around the mean values presented in Table 2. For the simulation, we assumed that if a cell did not undergo apoptosis within 3500 seconds, which is the mean time of cell death by apoptosis, it would continue to survive.

This approach allowed us to calculate the number of dead cells in each layer, as illustrated in Figure 6.

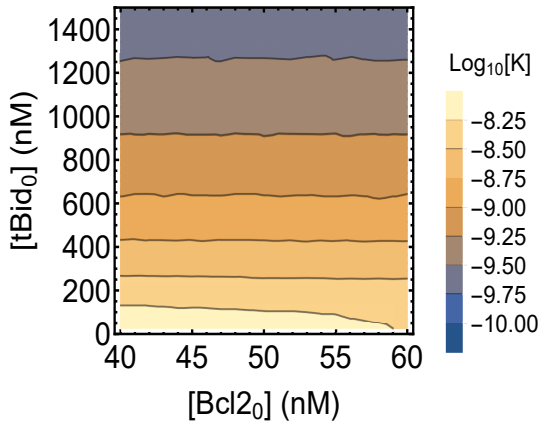

Figure 5. Density plot of the kinetic constant K as a function of the initial concentrations of tBid and Bcl-2 in logarithmic scale.

In particular, in the upper layers of the tumor (where $[tBid_0] > 251nm$, corresponding to $Z < 0.5\ mm$), the number of dead cells does not increase as $[tBid_0]$ increases. This result can be explained by considering that, when the initial concentration of tBid is very high, the likelihood of the optimized reaction occurring is also significantly elevated in the Gillespie algorithm. Consequently, until Bax is fully consumed, none of the other reactions in the model that contribute to increasing Caspase-3 levels and subsequent cell death takes place (see Table 2, references [26–29],).

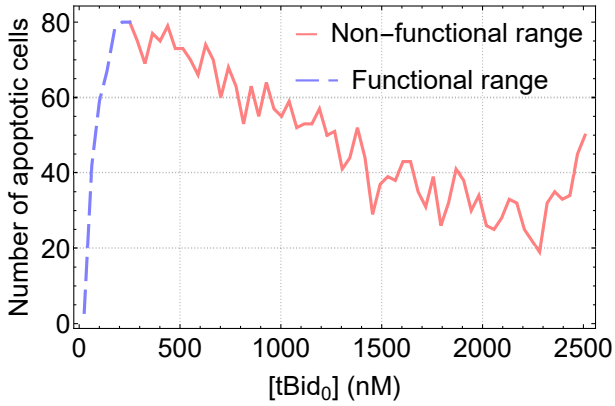

Figure 6. Number of dead cells as a function of tBid initial concentration. In blue, the functional range in which $[tBid_0]$ is proportional to the apoptotic signal.

To maintain the initial concentration of tBid proportional to the strength of the apoptotic signal, we selected initial concentrations in the range of 61 to $251nM$ for our subsequent simulations. By narrowing the range of $[tBid_0]$ values, we refined the K matrix used in the model, as shown in Figure 7. This adjustment highlights that at low concentrations of tBid, variations in Bcl-2 become increasingly influential. This effect is attributed to the distinct propermeabilizing and antipermeabilizing functions that each protein performs, respectively.

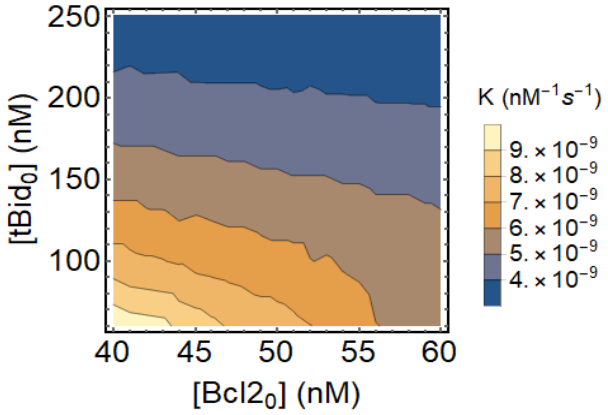

Figure 7. Density plot of the kinetic constant K as a function of the initial concentrations of tBid and Bcl-2.

III.3. Simulation of cell death by apoptosis in tumor tissue

Using the results of the previous section, we simulated an epithelial tumor treated with a topical drug to investigate how the number of cells undergoing apoptosis changes as a function of depth and the initial concentration of tBid. The tumor is modeled as a three-dimensional matrix consisting of six layers, each containing a 100 x 100 grid of cells. We assume that the average initial concentration of tBid in each of the six layers decreases exponentially. This approach is supported by experimental evidence that shows that topical drug application enhances absorption in the upper layers of the skin [30,31].

In the simulations, a cell was considered to undergo apoptosis if death occurred before 3500 seconds. In this case, it was assigned a value of 1. In contrast, if the cell did not die, it was assigned a value of 0. The density plots representing the matrices at various values of Z are presented in Figure 3. Dead cells are white and those that survive are red. It can be seen that as the depth increases, the density of cells that undergo apoptosis decreases. This result is in agreement with experimental data that demonstrate that some topical treatments are effective only for superficial tumors [32].

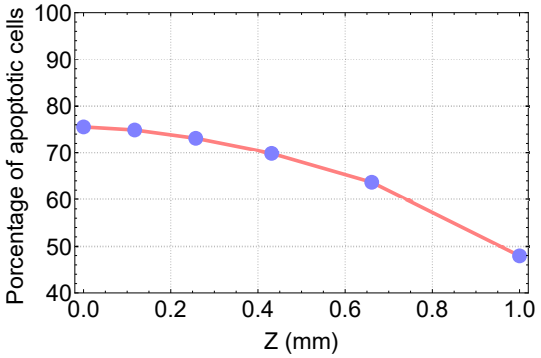

Figure 8. Percentage of dead cells versus tumor depth (Z). The tumor is modeled as a three-dimensional matrix consisting of six layers, each with 100×100 cells. A cell was considered apoptotic if it died within 3,500 seconds of treatment. For each layer, the percentage of dead cells was calculated.

To get an idea of the exact number of cells that died as a function of Z, we show these results in Figure 8. Almost 75 % of

the cells near the surface died from apoptosis and this number decreases as the depth of the tumor increases. At 1 *mm* depth, more than 50 % cells survive.

III.4. Simulation time versus optimization

Figure 9 compares the simulation times for both models in simulations with different initial concentrations of Bcl-2, while keeping the initial concentrations of other molecules constant.

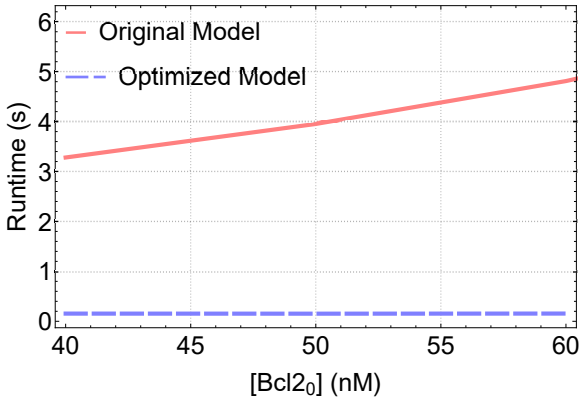

Figure 9. Simulation time as a function of the initial concentration of Bcl-2 for the apoptosis model that includes all reactions of membrane permeabilization (original) and the one that includes only one reaction (optimized).

The recorded time reflects how long each simulation takes to complete the membrane permeabilization process, which involves the set of simplified reactions. This time represents how long both simulations take to complete the permeabilization process of the membrane, where the set of reactions that we simplify participate. We can see that by increasing the initial concentration of Bcl-2, keeping $[tBid_0]$ constant, the time of the original model increases, while in the optimized model it is practically independent of this variable. In particular, at high initial concentrations of Bcl-2, the advantages of our optimization become even more pronounced. Given that this model will be applied to thousands of cells within tumor tissue, optimization is significantly improved.

In Tables 3 and 4 we show a comparison of simulation times for various initial concentrations of tBid and Bcl-2. The concentration values in the tables were selected as the limits used in our tumor simulations.

Table 3. Simulation time for the unoptimized model (s)

Concentration	**tBid$_0$ = 62.7 nM**	**tBid$_0$ = 250.8 nM**
Bcl2o = 40nM	3.90	3.515
Bcl2o = 60nM	6.626	4.406

Table 4. Simulation time for the optimized model (s)

Concentration	**tBid$_0$ = 62.7 nM**	**tBid$_0$ = 250.8 nM**
Bcl2o = 40nM	0.24861	0.134928
Bcl2o = 60nM	0.341222	0.144051

These results demonstrate that the performance of the optimized model is superior. To help the reader better understand the machine time saved with the proposed optimization, we present a straightforward calculation. We simulate 10000 cells across 6 layers. If each cell requires 6.626*s* to open the membrane, representing the maximum possible time, the total computational time would be $6 \times 10000 \times 6.626 = 397560$ s, which is equivalent to approximately 4.5 days of simulation. In contrast, using the optimized model, the maximum simulation time would be $6 \times 10000 \times 0.341 = 20460$ s, or about 5.6 hours. This significant reduction in machine time demonstrates that our optimization represents a significant advance in the study of cell death by apoptosis.

IV. CONCLUSION

In this study, we have developed a model that qualitatively simulates cell death by apoptosis, capturing the timing and concentration dynamics of key molecules involved in the intrinsic pathways. Our optimization of the equations governing mitochondrial membrane permeabilization has significantly reduced simulation times without compromising the accuracy of the cell death timing or the qualitative behavior of the involved molecules. The findings regarding the independence of K from Bcl-2 concentrations at high tBid levels provide valuable insights into the complex interactions within apoptotic signaling pathways. The substantial reduction in computation time enhances the feasibility of applying our model to simulate apoptosis in tissues containing large numbers of cells, making it a powerful tool for studying cell death in various biological contexts, particularly in tumor environments. Our model not only contributes to a deeper understanding of apoptosis but also lays the groundwork for future research aimed at exploring therapeutic strategies that target apoptotic pathways. We believe that this work will facilitate further advancements in computational biology and cancer research, ultimately leading to improved treatment approaches for diseases characterized by dysregulated apoptosis.

V. ACKNOWLEDGEMENTS

REFERENCES

[1] S. Kumari, R. Dhapola, D. H. Reddy, Apoptosis **28**, 943 (2023).

[2] V. K. Sharma, T. G. Singh, S. Singh, N. Garg, S. Dhiman, Neurochem. Res. **46**, 3103 (2021).

[3] C. Hu, X. Zhang, N. Zhang, W.-Y. Wei, L.-L. Li, Z.-G. Ma, Q.-Z. Tang, Clin. Transl. Med. **10**, e124 (2020).

[4] K. Tsuchiya, Microbiol. Immunol. **64**, 252 (2020).

[5] B. A. Carneiro, W. S. El-Deiry, Nat. Rev. Clin. Oncol. **17**, 395 (2020).

[6] O. Morana, W. Wood, C. D. Gregory, Int. J. Mol. Sci. **23**, 1328 (2022).

[7] M. Jiang, L. Qi, L. Li, Y. Li, Cell Death Discov. **6**, 112 (2020).

[8] B. Roche, J. M. Drake, P. Rohani, BMC Bioinform. **12**, 1 (2011).

[9] B. N. Brown, I. M. Price, F. R. Toapanta, D. R. DeAlmeida, C. A. Wiley, T. M. Ross, T. D. Oury, Y. Vodovotz, Math. Biosci. **231**, 186 (2011).
[10] J. S. Yu y N. Bagheri, Front. Bioeng. Biotechnol. **8**, 249 (2020).
[11] H. Sizek, A. Hamel, D. Deritei, S. Campbell, E. Ravasz Regan, PLoS Comput. Biol. **15**, e1006402 (2019).
[12] P. Dutta, L. Ma, Y. Ali, P. Sloot, y J. Zheng, BMC Syst. Biol. **13**, 1 (2019).
[13] L. C. Gomes-Pereira, M. Chaves, J. Roux, en *2020 28th Mediterranean Conference on Control and Automation (MED)* (IEEE, 2020), pp. 887–892.
[14] P. Schröder, A. Wagner, D. Stöhr, M. Rehm, y W. Ehlers, PAMM **19**, e201900310 (2019).
[15] M. Hendrata, J. Sudiono, Comput. Math. Methods Med. **2016**, 1 (2016).
[16] R. M. Schmitz, S. M. Willerth, G. van Rensburg, R. Edwards, J. Med. Biol. Eng. **40**, 41 (2020).
[17] R. A. Gatenby, Y. Artzy-Randrup, T. Epstein, D. R. Reed, y J. S. Brown, Cancer Res. **80**, 613 (2020).
[18] P. P. González-Pérez, M. Cárdenas-García, en *International Conference on Practical Applications of Computational Biology & Bioinformatics* (Springer, 2018), pp. 17–26.
[19] J. H. Buchbinder, D. Pischel, K. Sundmacher, R. J. Flassig, I. N. Lavrik, PLoS Comput. Biol. **14**, e1006368 (2018).
[20] D. Bernstein, Phys. Rev. E **71**, 041103 (2005).
[21] A. M. Kierzek, Bioinformatics **18**, 470 (2002).
[22] R. Abbas, S. Larisch, Cells **9**, 663 (2020).
[23] D. T. Gillespie, J. Phys. Chem. **81**, 2340 (1977).
[24] D. T. Gillespie, Annu. Rev. Phys. Chem. **58**, 35 (2007).
[25] S. Raychaudhuri, E. Willgohs, T.-N. Nguyen, E. M. Khan, T. Goldkorn, Biophys. J. **95**, 3559 (2008).
[26] J. G. Albeck, J. M. Burke, S. L. Spencer, D. A. Lauffenburger, P. K. Sorger, PLoS Biol. **6**, e299 (2008).
[27] F. Fantini, A. Greco, C. Del Giovane, A. Cesinaro, M. Venturini, C. Zane, T. Surrenti, K. Peris, P. Calzavara-Pinton, J. Eur. Acad. Dermatol. Venereol. **25**, 896 (2011).
[28] M. Rehm, H. J. Huber, H. Dussmann, J. H. Prehn, EMBO J. **25**, 4338 (2006).
[29] N. J. Waterhouse, J. C. Goldstein, O. Von Ahsen, M. Schuler, D. D. Newmeyer, D. R. Green, J. Cell Biol. **153**, 319 (2001).
[30] B. Newell, W. Zhan, J. Control. Release **360**, 447 (2023).
[31] J. J. Calcutt, M. S. Roberts, Y. G. Anissimov, Pharm. Res. **39**, 783 (2022).
[32] N. Gupta, G. Gupta, D. Singh, Front. Nanotechnol. **4**, 1006628 (2022).

CORRELATING TEXTURE AND ELECTROMECHANICAL PROPERTIES OF ACTIVATED CARBONS: FIRST STEPS

CORRELACIONANDO TEXTURA Y PROPIEDADES ELECTROMECÁNICAS DE CARBONES ACTIVADOS: PRIMEROS PASOS

H. Reborido[a†], R. Machado-García[b], D. Cascaret-Carmenaty[b], O. Quesada-González[b], P. Muné[a†]

a) Departamento de Física, Universidad de Oriente, Cuba. mune@uo.edu.cu†
b) Departamento de Química, Universidad de Oriente, Cuba
† corresponding author

Recibido 10/11/2024; Aceptado 21/2/2025

Keywords: Porous materials (Materiales porosos); Activated carbons (Carbones activados); Electrical conductivity (Conductividad eléctrica); Mechanical properties (Propiedades mecánicas).

The growing demand for activated carbons has driven the development of inexpensive and easily applicable experimental methods for evaluating their behavior. One promising avenue, for the obtaining of activated carbon, lies in utilizing agro-industrial residues. This approach offers a sustainable path to minimize environmental impact while producing high-value materials from affordable sources [1,2].

This note presents a simple experimental method for determining four electromechanical parameters of powdered activated carbon samples. These parameters are then used to derive a mathematical expression describing the dependence of sample conductivity on applied uniaxial pressure. Furthermore, the note shows evidence of a certain correlation between some of these parameters and the texture of the activated carbon samples.

For electrical characterization of the activated carbon a two-point method was used. A known mass of material was compacted uniaxially (~ 50 mg) under increasing pressures within an insulating matrix using piston and base electrodes. An ohmmeter was used to measure the electrical resistance across the electrodes at 29 °C [3]. This study focuses on the ratio of density to resistivity ρ_m/ρ, a parameter that can be determined using the expression:

$$\frac{\rho_m}{\rho} = \frac{m}{R \cdot A^2} \tag{1}$$

Here m represents the mass of the carbonaceous material, R is the electrical resistance and A is the cross-sectional area. This ratio exhibits a linear relationship with uniaxial pressure applied to the carbonaceous powder, particularly in the range of 20-240 MPa. Moreover, this parameter offers the advantage of being independent of uncertainties associated with measuring the distance between contacts.

At this point, the linear relationship between the parameter and uniaxial pressure, focusing on carbonaceous materials derived from various sources is explored. Figure 1 illustrates this linear dependence. Let us see first the obtention of the carbonaceous materials derived from sugar cane bagasse. In this case three samples were prepared. Two were treated with acid and base, respectively, while one remained untreated. Treatments involved a 24-hour impregnation in 0.5 mol/L activating agent solution, followed by washing with distilled water and drying at 105 °C. All samples were then subjected to pyrolysis at 850 °C in an argon flux of 5 mL/min for 30 minutes and cooled down to room temperature in the same argon flux. The resulting material from the pyrolysis was washed in deionized water using ultrasound with a power of 40 W during 5 minutes. Despite these differences in treatment, the parameter consistently displays a linear behavior with applied uniaxial pressure. Similar linear behavior was also observed in carbonaceous materials derived from other agro-industrial residuals, namely coconut shells, peanut hulls, and rice husks (see Figure 1). These materials were first transformed into black carbon through pyrolysis at 600 °C in a nitrogen flux of 80 mL/min. Subsequently, all carbons were physically activated using steam at 850 °C for 30 minutes. As last step, the resulting material was cooled down until ambient in the same nitrogen flux. The studied powders had similar particle size; it was less than 63 in all samples. Linear least-squares fitting of the experimental data yielded high correlation coefficients ($r^2 > 0.99$), confirming a strong linear relationship in all cases. Uncertainties in the intercept and slope were below 4 %.

On the other hand, the effective-medium approximation (EMA) provides a framework for understanding the effective conductivity σ_e, of porous materials, such as those studied here. Equation (2) describes the effective conductivity of the porous material, where represents the conductivity of the carbonaceous matrix and c is the pores concentration [4]:

$$\sigma_e = \sigma_B \left(1 - \frac{3}{2}c\right) \tag{2}$$

Here $c < 3/2$, indicating that the percolation threshold has been exceeded.

The sample volume exhibits an exponential dependence on the uniaxial pressure, as described by (3):

$$V = A_1 e^{-\beta_1 P} \tag{3}$$

where P represents the uniaxial pressure, A_1 is the volume at zero pressure and β_1 is the compressibility coefficient [5].

Experimental data presented in Figure 1 can be described by the following expression:

$$\frac{\rho_m}{\rho}(P) = A_2 + \beta_2 P \tag{4}$$

Combining (3) and (4) allows us to express the sample electrical conductivity as a function of pressure, as shown in equation (5):

$$\sigma_e = \frac{1}{m}(A_2 + \beta_2 P) A_1 e^{-\beta_1 P} \tag{5}$$

This relationship suggests that uniaxial pressure has two opposing effects on the electrical conductivity of the sample. At lower pressures, the electrical conductivity increases with pressure due to improved contact between the grains. Higher pressures, however, lead to grain fracture and consequently a decrease in conductivity.

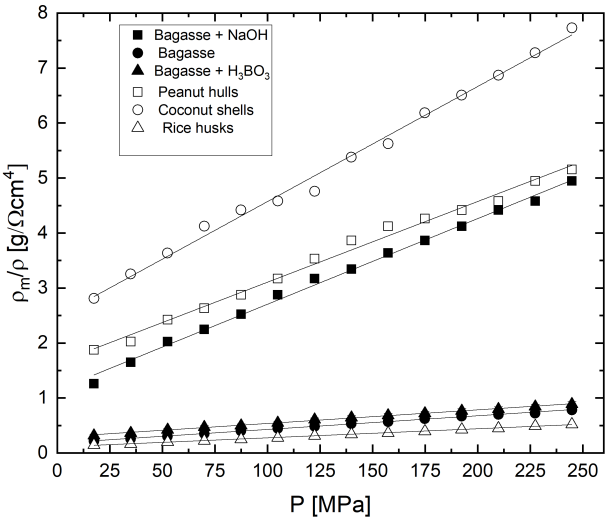

Figure 1. $\frac{\rho_m}{\rho}(P)$ dependence of different carbonaceous materials derived from sugar cane bagasse and others agro-industrial residuals. The continue lines represent the linear fittings of the experimental data obtained by least squares method.

Figure 2 presents both experimental data and theoretical calculations, using (5), for the dependence of effective conductivity on uniaxial pressure. The inset illustrates the procedure for determining β_1 and A_1 starting from the linear behavior of $\ln(V)$ as a function of uniaxial pressure. Also, this figure shows increasing uncertainty with pressure in the experimental data for coconut shell and peanut hull samples. A few data points (two or three per sample) deviate significantly from (5), even accounting for experimental uncertainty. This deviation is likely due to the empirical nature of (5) and uncertainties in parameters A_1, β_1, A_2, and β_2 (below 1 % and 5 %, respectively, for A_1 and β_1). The equation (5) also predicts a maximum of $\sigma_e(P)$ at $P_{max} = \frac{1}{\beta_1} - \frac{A_2}{\beta_2}$, which can be observed, for the sample derived from peanut hulls, into the pressure range of the measure.

Equation (6) enables the determination of the electrical conductivity of the carbonaceous material, σ_B , independent of pore effects. This aspect is crucial for evaluating the suitability of activated carbons for electrical applications:

$$\sigma_e(P \to 0) = \frac{A_1 A_2}{m} = \sigma_B\left(1 - \frac{3}{2}\frac{V_p}{A_1}\right) \tag{6}$$

Here V_p represents the pore volume linked to meso and macropores.

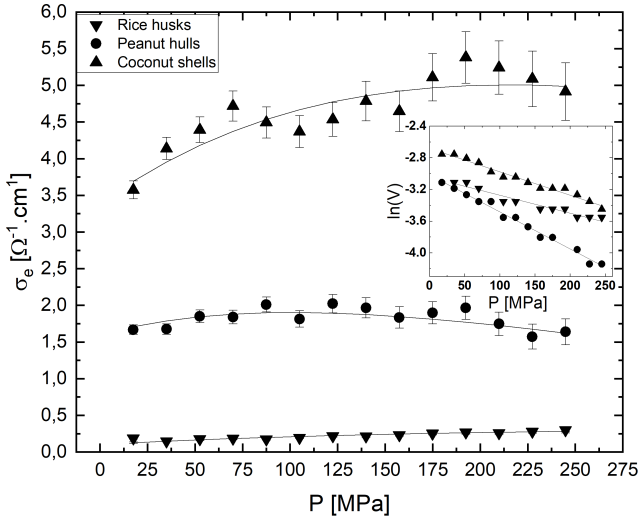

Figure 2. Effective conductivity as a function of the uniaxial pressure for carbonaceous materials obtained from the biomass described in the legend. The solid lines represent the conductivity values calculated using equation (5). The inset depicts the linear relationship between natural logarithm of volume and pressure, which confirms Equation (3).The error bars represent the experimental uncertainties.

Due to the small size of micropores, they are considered as part of the carbonaceous matrix. The pore volume, V_p^*, is usually determined by means of adsorption and desorption of nitrogen (N_2) by the carbonaceous material and it is given in cm^3/g. However, in (6), $V_p = mV_p^*$, where $m = 50$ mg . In addition, the mathematical expression $P \to 0$ refers the limit of low pressures, where the linear and exponential dependencies on P are satisfied.

Table I provides an example of applying (6) to samples with effective electrical conductivity as a function of uniaxial pressure, as depicted in Figure 2. The results indicate that the sample derived from coconut shells exhibits the highest value of σ_B, followed by the sample derived from peanut hulls. The sample obtained from rice husks demonstrates the least desirable behavior due to its lowest value of σ_B. This observation aligns with the presence of a significant percentage of SiO_2 in the carbonaceous materials obtained

from rice husks [2]. Also, it is easy of verifying for all samples $\frac{V_p}{A_1} < 0.16$ that satisfies the condition predicted by EMA.

Table 1. V_p, A_1, A_2, and σ_B of the samples presented in Figure 2.

Biomass	$V_p\,[\mathrm{cm}^3]$	$A_1\,[\mathrm{cm}^3]$	$A_2\left[\frac{g}{\Omega\,\mathrm{cm}^4}\right]$	$\sigma_e\left[\frac{1}{\Omega\,\mathrm{cm}}\right]$
Coconut shells	0.0104	0.068	2.48	4.39
Peanut hulls	0.0056	0.049	1.64	1.93
Rice husks	0.0035	0.048	0.110	0.12

In summary, this study has successfully derived an expression for the dependence of effective conductivity, σ_e, on uniaxial pressure, P, leveraging the linear relationship between the product of density and conductivity, $\rho_m\sigma_e$, and pressure, alongside the established relationship between sample volume and applied uniaxial pressure. The four parameters in (5) provide a unique "fingerprint"for characterizing the electro-mechanical properties of activated carbons. This finding suggests that the methodology employed in this study holds promise for evaluating the textural properties of activated carbons, serving as a valuable preliminary assessment tool. A series of ongoing research projects aim to further explore this approach, potentially leading to a more comprehensive understanding of the relationship between texture and electro-mechanical behavior in activated carbons.

REFERENCES

[1] Z. Heidarinejad, M. Hadi Dehghani, M. Heidari, I. A. Mika Sillanpää, *Environ. Chem. Lett.*, **18**, 393 (2020).

[2] R. G. Machado-García, "Synthesis of composites based on activated carbon and TiO_2 doped with Co and Fe from residues for the photocatalytic degradation of Cibacron yellow F-4G dye", PhD. Thesis, Universidad de Oriente (2022).

[3] V. N. Rubchevskiy, S. A. Ovchinnikova, Yu. A. Chernyshov, I. V. Zolotarev, Yu. A. Yatsenko, E. I. Toryanik, A. V. Gryzlov, and S. S. Kubrak, *Coke Chem.*, **57**, 381 (2014).

[4] D. Stroud, *Phys. Rev. B*, **12**, 8 (1975).

[5] N. Warren, *J. Geophys. Res.*, **78**, 352 (1973).

PYROELECTRIC RESPONSE AND FIGURES OF MERIT OF LEAD-FREE FERROELECTRIC CERAMICS

RESPUESTA PIROELÉCTRICA Y FIGURAS DE MÉRITO DE CERÁMICAS FERROELÉCTRICAS LIBRES DE PLOMO

A. C. Iglesias-Jaime[a], A. Peláiz-Barranco[a,b,c†], J. D. S. Guerra[c], T. Yang[b]

a) Grupo de Materiales Ferroicos, Facultad de Física–IMRE, Universidad de la Habana. San Lázaro y L, Vedado. La Habana 10400, Cuba. pelaiz@física.uh.cu†
b) Functional Materials Research Laboratory, School of Materials Science and Engineering, Tongji University, 4800 Cao'an Road, Shanghai 201804, China.
c) Grupo de Ferroeléctricos Multifuncionais, Instituto de Física, Universidade Federal de Uberlândia, Minas Gerais, 38408-100, Brazil.
† corresponding author

Recibido 4/2/2025; Aceptado 26/3/2025

Keywords: Ferroelectrics (ferroeléctricos); pyroelectrics (piroeléctricos); pyroelectric devices (dispositivos piroeléctricos).

I. INTRODUCTION

Lead-free ferroelectric materials have been extensively studied as a quest to replace lead-based ferroelectric commonly used in engineering systems such as actuators, batteries, sonars, sensors, electromechanic engines, etc [1–3]. Numerous authors have conducted research on various aspects of the ferroelectric, dielectric and piezoelectric properties. However, there not many studies specifically addressing its pyroelectric behavior [4, 5].

The $(Bi_{0.5}Na_{0.5})_{1-x}Ba_xTiO_3$ (BNT-xBT) system has been reported as one of the most promising materials to replace the lead-based systems, receiving a growing interest from the scientific society [2, 6–10], but with only a few publications regarding its pyroelectric behavior [6–8]. The main pyroelectric investigations of the BNT-xBT have been centered on the morphotropic phase boundary (MPB), around x = 0.06 *at* %, and have involved doping with elements such as tantalum, zirconium and manganese in order to enhance the pyroelectric properties [6–8].

Recently, $(Bi_{0.5}Na_{0.5})_{1-x}Ba_xTiO_3$ lead-free ferroelectric ceramics (x = 0, 2, 5, 8, 10, 12, 16, 18 *at* %) were studied considering x-ray diffraction, Raman spectroscopy, dielectric and piezoelectric behavior [9, 10]. From these results, a new phase diagram has been proposed considering a wider compositional range than those reported in the literature, which offers new insights for a better understanding on the features of the phase diagram for the ceramic system [9]. Also, very good piezoelectric parameters were reported for composition showing tetragonal phases [10]. From this point of view, the two highest barium concentrations have been selected in order to evaluate the pyroelectric behavior in a wide temperature range. It is known that depending on the specific application, selecting an optimal pyroelectric material becomes crucial to achieve maximum efficiency in pyroelectric devices. In this sense, the evaluation of several parameters, such as the figures of merit (FOMs) is very important [11], which guide us toward the most suitable material for the intended purpose. Generally, FOMs are described by four characteristic parameters known as current responsivity (F_i), voltage responsivity (F_V), detectivity (F_D) and the energy harvesting figure of merit (F_E), as expressed by the equations (1) to (4), respectively [11, 12].

$$F_i = \frac{p}{\rho C_p} \tag{1}$$

$$F_V = \frac{p}{\rho C_p \varepsilon_0 \varepsilon} \tag{2}$$

$$F_D = \frac{p}{\rho C_p \sqrt{\varepsilon_0 \varepsilon \tan\delta}} \tag{3}$$

$$F_E = \frac{p^2}{\varepsilon_0 \varepsilon} \tag{4}$$

F_i characterizes the maximum current that can be generated, F_V represents the maximum voltage output of the sample, F_D provides the voltage responsivity with the optimal signal-to-noise ratio and F_E characterizes the capacity for energy harvesting from temperature change [13, 14]. The p parameter corresponds to the pyroelectric coefficient, ρ represents the density, C_p is the specific heat at constant pressure, ε denotes the dielectric permittivity, and $\tan\delta$ represents the dielectric losses of the material [15].

In this context, the objective of the present paper is to evaluate the pyroelectric response and the corresponding figures of merit for $(Bi_{0.5}Na_{0.5})_{1-x}Ba_xTiO_3$ (x=16 and 18 *at* %) ceramic system.

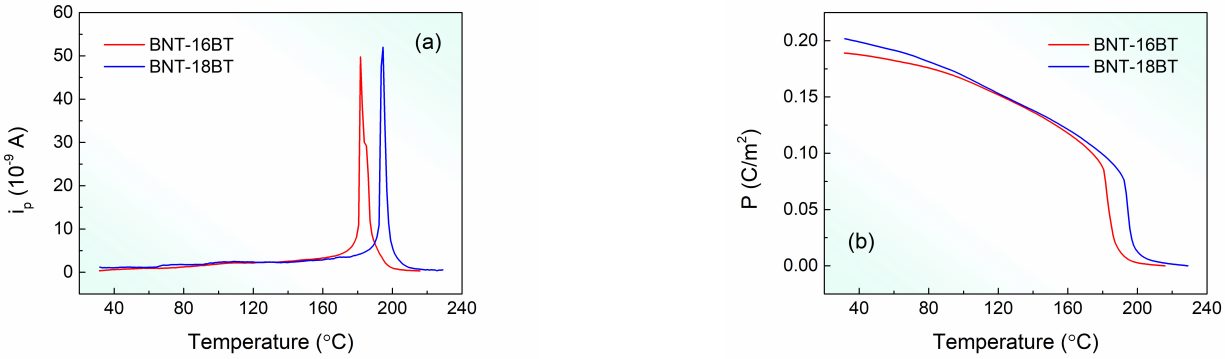

Figure 1. Temperature dependence of (a) pyroelectric current (i_p) and (b) remnant polarization (P), for the studied samples.

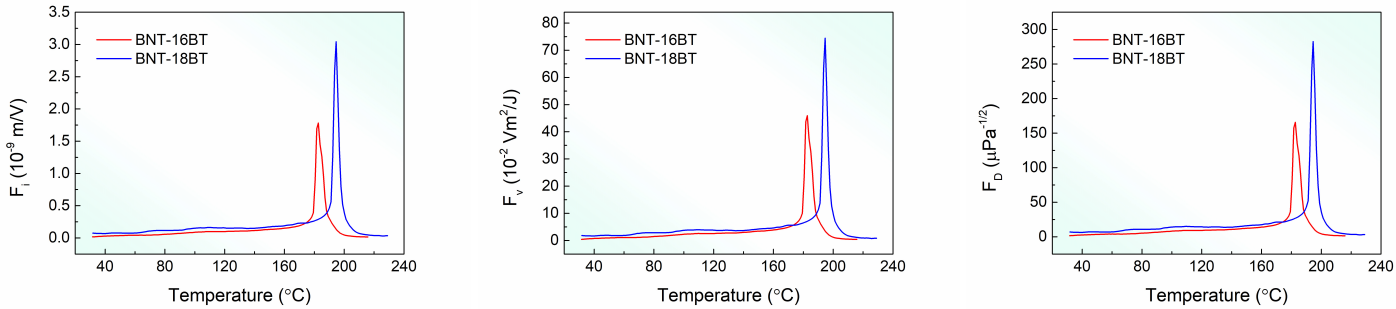

Figure 2. Temperature dependence of the FOMs for the studied samples.

II. EXPERIMENTAL PROCEDURE

$(Bi_{0.5}Na_{0.5})_{1-x}Ba_xTiO_3$ ceramics, for x = 16 and 18 *at* %, were prepared by using the solid-state reaction sintering method. High purity oxides (Bi_2O_3: 99.999 %; Ba_2CO_3: 99.36 %; Ti_2O_2: 98 %; Na_2CO_3: 99.5 %) were mixed and manually milled using a mortar for 2 hours. The samples were calcinated at 800 °C for 1 hour in air atmosphere. The powders were milled again and pressed as thin discs by using 2 ton/cm^2. The disc ceramics were sintered at 1150 °C for 2 hours in an air atmosphere, using a covered platinum crucible to prevent bismuth loss through evaporation. The samples were hereafter labeled as BNT-16BT and BNT-18BT, respectively. The structural analysis confirmed the formation of a pure perovskite structure without additional spurious phases, showing a tetragonal phase [9].

Silver paint electrodes were applied on the opposite parallel surfaces of disk-shaped ceramics samples by a heat treatment at 590 °C. The polarization process was carried out at 100 °C, applying an electric field of 2 kV/mm. Once polarized the samples, the pyroelectric current (i_p) was directly measured through the static method using a Keithley 6485 Picoammeter covering a wide temperature range (25 – 210 °C). The remnant polarization (P) and the pyroelectric coefficient were calculated from the temperature dependence of i_p [16]. The temperature dependence of the pyroelectric figures of merit (FOMs) were obtained by using Eqs. (1), (2), (3) and (4), as well as the dielectric parameters reported elsewhere [9].

III. RESULTS AND CONCLUSIONS

Figure 1 shows the temperature dependence of the pyroelectric current (i_p) and the remnant polarization (P) for the studied compositions. A typical peak for the pyroelectric current around 180 - 200 °C has been obtained for both samples, with the corresponding decreasing to zero at the reported depolarization temperature (T_d) [9]. It is important to note the high thermal stability through the studied temperature range, which is a relevant behavior to be consider for applications involving high-temperature sensors [17].

Figure 2 shows the temperature dependence for the corresponding FOMs, given by equations (1), (2) and (3). The behavior is similar to that obtained for the pyroelectric current (T_d) [9], with well-defined peaks below the depolarization temperature and also high thermal stability. The maximum obtained values for the FOMs, located near around this critical temperature, are higher than those for other reported materials, such as $BaCe_{0.12}Ti_{0.88}O_3$ [18], $Ba_{0.85}Ca_{0.15}Zr_{0.1}Ti_{0.9}O_3$ [19] and $PbNb_{0.02}(Zr_{0.95}Ti_{0.05})_{0.98}O_3$ [20], which were even polarized at higher electric fields than the studied ceramics.

Table 1 summarizes the obtained values of the FOMs from Figure 2, at room temperature, of the studied samples and other ceramic systems reported in the literature. It can be observed that F_i values of both studied samples are quite modest in comparison with the literature average, which can be attributed to the low p values obtained. The BNT-18BT shows better results than those of BNT-16BT, being the F_V

parameter which exhibit the best result, representing the maximum voltage output that can be obtained from the sample.

The most relevant result which has been obtained in the present study corresponds to the F_E parameter, in particular for BNT-18BT. Figure 3 shows this FOM at room temperature for several reported materials, included the studied compositions, suggesting the suitability of BNT-18BT for pyroelectric energy harvesting (PyEH) [28]. This high F_E value is mostly attributed to the low permittivity value of this sample at room temperature [10].

Table 1. FOMs at room temperature for the studied compositions and other reported ceramic systems.

Materials	$\mathbf{F_i}$ (10^{-9} mV)	$\mathbf{F_V}$ (10^{-2} m^2/C)	$\mathbf{F_D}$ (μPa$^{-0.5}$)
BNT-16BT	0.02	0.42	1.5
BNT-18BT	0.07	1.8	6.8
BCT 21 [21]	1.71	0.9	-
BNT-BT-ST [22]	-	1.8	5.89
BTS [23]	1.03	0.2	-
BCSZT [5]	3.86	1.7	28.4
BNKLBTT [24]	2.21	3.0	14.8
BNT-BTZ [7]	2.03	2.2	10.5
PLZT-25 [25]	1.10	4.4	50.1
PLZT-50 [25]	0.12	0.16	1.9
PLZT 4/86/14 [26]	2.90	4.8	35.4
PLZT-0.11Cr [27]	1.55	1.16	8.3

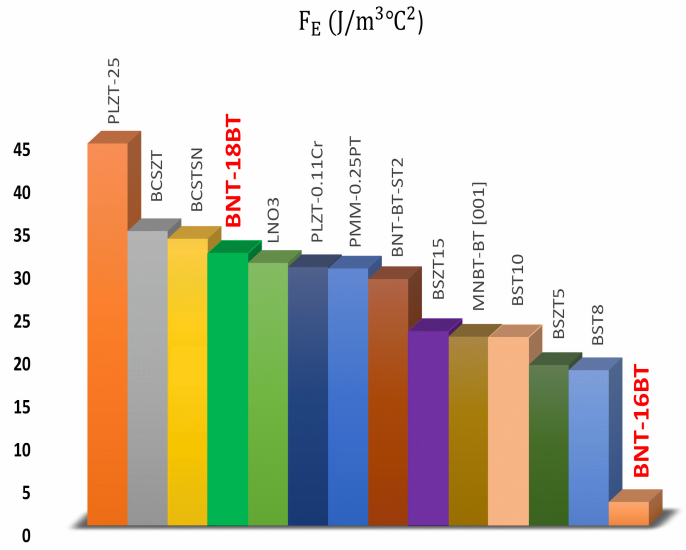

Figure 3. F_E values at room temperature for the studied samples, BNT-16BT and BNT-18BT, and other previous reported materials. PLZT-25 [25], BCSZT [5], BCSTSN [29], LNO3 [15], PLZT-0.11Cr [27], PMN-0.25PT [12], BNT-BT-ST2 [22], BSZT15 [30], MNBT-BT [001] [31], BTS10 [32], BSZT5 [30], BST8 [32].

From this point of view and considering the previous piezoelectric results [10] for the studied BNT-18BT, this compound emerges as an excellent candidate for energy harvesting applications based in the pyroelectric, piezoelectric effect or their combination.

IV. ACKNOWLEDGEMENTS

The authors acknowledge the National Council of Scientific and Technological Development (CNPq) Grants (Nos. 303447/2019-2, 309494/2022-2 and 408662/2023-9), Minas Gerais Research Foundation (FAPEMIG) Grants (Nos. PPM-00661-16 and APQ-02875-18), Coordenação de Aperfeiçoamento de Pessoal de Nível Superior—Brasil (CAPES)—Finance Code 001 and PROAP/CAPES—AUXPE 0237/2021 (UNESP—Ilha Solteira, So Paulo) from Brazil, for the financial support. Special thanks to ICTP for financial support of Latin-American Network of Ferroelectric Materials (NT-02). Thanks to the National Program for Basic Sciences of Cuba (Project No. PN223LH010-068) and the National Program for Nanoscience and Nanotechnology (Project No. PN211LH008-069). This work was supported by the National Key R&D Program of China (No. 2023YFE0198300).

REFERENCES

[1] K. Uchino, *Lead-Free Piezoelectrics*, Eds. S. Priya and S. Nahm, Chapter 17 (Springer, New York, 2012), pp. 511.
[2] I. Coondoo, N. Panwar and A. Kholkin, *J. Adv. Dielect.* **3**, 1330002 (2013).
[3] S. Supriya, *Coord. Chem. Rev.* **479**, 215010 (2023).
[4] R. W. Whatmore, *J. Appl. Phys.* **133**, 080902 (2023).
[5] H. He. X. Liu. E. Hanc, C. Chen, H. Zhang and L. Lu, *J. Mat. Chem. C* **8**, 1494 (2020).
[6] A. Balakt, C. Shaw and Q. Zhang, *Ceram. Int.* **43**, 3726 (2017).
[7] F. Guo, B. Yang, S. Zhang, F. Wu, D. Liu, P. Hu, Y. Sun, D. Wang and W. Cao, *Appl. Phys. Lett.* **103**, 182906 (2013).
[8] J. Abe, M. Kobune, T. Nishimura, T. Yazaw and Y. Nakai, *Integr. Ferroel.* **80**, 87 (2006).
[9] B. R. Moya, A. C. Iglesias-Jaime, A. C. Silva, A. Peláiz-Barranco and J. D. S. Guerra, *J. Appl. Phys.* **135**, 164106 (2024).
[10] A. C. Iglesias-Jaime, T. Yang. A. Peláiz-Barranco and J. D. S. Guerra, *Rev. Cub. Fis.* **39**, 33 (2022).
[11] H. Li, C. Bowen and Y. Yang, *Adv. Funct. Mater.* **31**, 2100905 (2021).
[12] C. R. Bowen, J. Taylor, E. LeBoulbar, D. Zabek, A. Chauhan and R. Vaish, *Energy Environ. Sci.* **7**, 3836 (2014).
[13] D. Zhang, H. Wu, C. R. Bowen and Y. Yang, Small **17**, 2103960 (2021).
[14] S. B. Land and D. K. Das-Gupta, *Handbook of advanced electronic and photonic materials and devices*, Chapter 1 (Academic Press, 2001).
[15] S. B. Lang, *Phys. Today* **58**, 31 (2005).
[16] S. B. Lang, *Source Book of Pyroelectricity* (Gordon and Breach, Chience Publishers Inc., New York, 1974).
[17] X. Jian, K. Kim, S. Zhang, J. Johnson and G. Salazar, *Sensors* **14**, 144 (2014).
[18] S. M. Zeng, X. G. Tang, Q. X. Liu, Y. P. Jiang, M. D. Li, W. H. Li and Z. H. Tang, *J. Alloy. Compd.* **776**, 731 (2019).
[19] M. Sharma, V. P. Singh, S. Singh, P. Azad, B. Ilahi and N. A. Madhar, *J. Electron. Mater.* **47**, 4882 (2018).
[20] H. Wei and Y. Chen, *Ceram. Int.* **41**, 6158 (2015).

[21] K. S. Srinkanth and R. Vaish, *J. Eur. Ceram. Soc.* **37**, 3927 (2017).
[22] S. Patel, A. Chauhan, S. Kundu, N. A. Madhar, B. Ilahi, R. Vaish and K. B. R. Varma, *AIP Advances* **5**, 087145 (2015).
[23] K. Srikanth, S. Patel and R. Vaish, *Int. J. Appl. Ceram. Technol.* **15**, 546 (2018).
[24] S. T. Lau, C. H. Cheng, S. H. Choy, D. M. Lin, K. W. Kwok and H. L. Chan, *J. Appl. Phys.* **103**, 104105 (2008).
[25] J. D. S. Guerra, A. Peláiz-Barranco, A. C. Silva, F. Calderón-Piñar and A. Iglesias-Jaime, *Ferroelectrics* **611**, 138 (2023).
[26] P. Qiao, Y. Zhang, X. Chen, M. Zhou, G. Wang and X. Dong, *Ceram. Int.* **45**, 7114 (2019).
[27] K. K. Bajpai, K. Sreenivas, A. K. Gupta and A. K. Shukla, *Ceram. Int.* **45**, 14111 (2019).
[28] A. Thakre, A. Kumar, S. Hyun-Cheol, J. Dae-Yong and R. Jungho, *Sensors* **19**, 2170 (2019).
[29] X. Liu, D. Xu, Z. Chen, B. Fang, J. Ding, X. Zhao and H. Luo, *Adv. Appl. Ceram.* **114**, 436 (2015).
[30] M. Aggarwal, M. Kumar, R. Syal, V. P. Singh, A. K. Singh, S. Dhiman and S. Kumar, *J. Mater. Sci. Mater. Electron.* **31**, 2237 (2020).
[31] R. Sun, J. Wang, F. Wang, T. Feng, Y. Li, Z. Chi, X. Zhao and H. Luo, *J. Appl. Phys.* **115**, 074101 (2014).
[32] K. S. Srinkanth, V. P. Singh and R. Vaish, *Int. J. Appl. Ceram. Techn.* **15**, 140 (2018).

RADIOACTIVITY LEVELS AND RADIATION HAZARD IN SANDS FROM CUBAN BEACHES

NIVELES DE RADIACTIVIDAD Y PELIGROSIDAD POR RADIACION EN ARENAS DE PLAYAS CUBANAS

G. Pérez[a], H. Cartas[b],A. O. Casanova[a], O. Díaz[a†]

a) Dpto. de Física Nuclear, Instituto de Tecnologías y Ciencias Aplicadas, Universidad de La Habana, La Habana, Cuba; odrizo@instec.cu†
b) Centro de Estudios Ambientales, Cienfuegos, Cuba.
† corresponding author

Recibido 18/11/2024; Aceptado 20/5/2025

Keywords: radioactivity (radiactividad); radiation hazard (radiación peligrosa); beach sands (arenas de playa); Cuba.

The natural radionuclides ^{238}U, ^{232}Th and ^{40}K are called primordial radionuclides, because they are present on the Earth since the creation of the planet. The nonuniform distribution of natural radionuclides has been observed in various environmental matrices such as soil, sand, water, air, sediment, etc. Natural radionuclides often reach these matrices by the weathering process of rocks and other materials.

The purpose of the present study was to determine the levels of natural radioactivity (^{226}Ra, ^{232}Th and ^{40}K) on the sands of some Cuban white sand beaches (Fig. 1), in order to assess the potential radiological risks to their users.

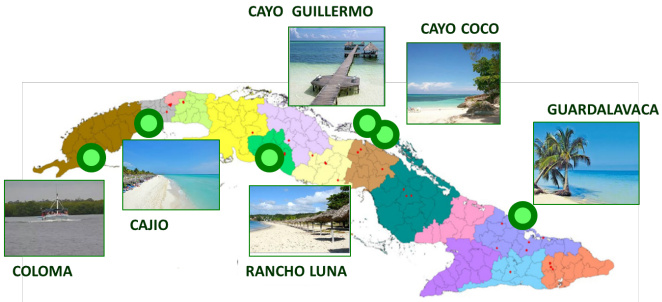

Figure 1. Location of the studied sand beaches

Beach sand samples, which reached equilibrium at the end of a time of one month, were counted for 48 hours on a well calibrated HPGe gamma spectrometer at the Center for Environmental Studies at Cienfuegos, Cuba [1]. In the study, while ^{40}K activity concentrations were determined directly based on 1460 keV gamma ray, the ^{238}U and ^{232}Th activity concentrations were indirectly determined from the daughter nuclides of these radionuclides. The ^{214}Pb or ^{214}Bi activity concentrations of the samples need to be accepted as a measure of the ^{226}Ra content rather than ^{238}U itself [2] . That is, in the analysis of the samples, for ^{226}Ra activity, ^{214}Bi's 609 keV and ^{214}Pb's 352 keV gamma transitions were used, while for ^{232}Th activity, ^{228}Ac's 911 keV gamma transition was used. The activity concentrations of natural radionuclides for beach sand samples under study, and some reported worldwide, are presented in Table 1. The measured activities are directly related to natural gamma radiation and represent the geological background of the rock settings. The only exception is the activity of ^{232}Th measured on the beach sand of La Coloma, with a mean activity slightly higher than the mean concentration of ^{232}Th worldwide (30 Bq $\cdot$ kg^{-1} [3]).

Table 1. Activity concentrations of ^{226}Ra, ^{232}Th and ^{40}K (main ± SD, in Bq $\cdot$ kg^{-1}) in Cuban and worldwide beach sands.

Beach	**^{226}Ra**	**^{232}Th**	**^{40}K**
La Coloma, Cuba	19 ± 1	37 ± 1	40 ± 8
Cajio, Cuba	6 ± 1	6 ± 3	47 ± 7
Rancho Luna, Cuba	4.5 ± 0.7	2.6 ± 0.5	274 ± 12
Cayo Coco, Cuba	12 ± 1	4.6 ± 0.6	10.6 ± 0.7
Cayo Guillermo, Cuba	5.7±0.7	2.1±0.4	135±8
Guardalavaca, Cuba	2.1±0.7	1.5±0.4	15±1
Xiamen, China [4]	15±4	11±8	396±75
Zonguldak, Turkey [5]	23±1	20±2	245±14
Ao Phrao, Thailand [6]	11±2	6.4±0.8	174±67
Tamil Nadu, India [7]	13±4	6±1	379±40
El Ingles, Spain [8]	23±1	31±2	726±32
Penang, Malaysia [9]	31±8	36±6	369±17
UNSCEAR [3]	35	30	400

Radiological parameters such as *radium equivalent* activity (R_{aeq}), *absorbed dose rate* (D_R) and *gamma index* (I_γ) were calculated (Table 2) using the following standard formulas:

$$R_{aeq}(\text{Bq}\cdot\text{kg}^{-1}) = C_U + 1.43C_{Th} + 0.0077C_K \quad (1)$$

$$D_R(\text{nGy}\cdot\text{h}^{-1}) = 0.462C_U + 0.604C_{Th} + 0.0042C_K \quad (2)$$

$$I_\gamma = \frac{C_U}{150} + \frac{C_{Th}}{100} + \frac{C_K}{1500} \quad (3)$$

where, C_U, C_{Th} and C_K, (given in $\text{Bq}\cdot\text{kg}^{-1}$), are the activity concentrations of ^{238}U, ^{232}Th and ^{40}K, respectively. The safety value for this I_γ index is ≤ 2 [3].

Table 2. Radiological indexes.

Beach	$\mathbf{R_{aeq}}$ ($\text{Bq}\cdot\text{kg}^{-1}$)	$\mathbf{D_R}$ ($\text{nGy}\cdot\text{h}^{-1}$)	$\mathbf{I_\gamma}$
La Coloma, Cuba	72	33	0.52
Cajio, Cuba	15	8	0.13
Rancho Luna, Cuba	10	15	0.24
Cayo Coco, Cuba	19	9	0.13
Cayo Guillermo, Cuba	10	10	0.15
Guardalavaca, Cuba	4	3	0.04
Xiamen, China [4]	34	30	0.47
Zonguldak, Turkey [5]	53	33	0.52
Ao Phrao, Thailand [6]	21	16	0.25
Tamil Nadu, India [7]	24	26	0.40
El Ingles, Spain [8]	73	60	0.95
Penang, Malaysia [9]	85	52	0.81
World average [3]	81	59	2

The calculated R_{aeq} values varied from 4 to 72 $\text{Bq}\cdot\text{kg}^{-1}$, showing that all studied sands show activity lower than the recommended safety limit. The dose rate varied from 3 to 33 $\text{nGy}\cdot\text{h}^{-1}$, all they are also lower than the worldwide average value of 59 $\text{nGy}\cdot\text{h}^{-1}$.

Finally, the estimated values of gamma representative level index ranged from 0.04 to 0.52, confirming that mean values are lower than the recommended safety limits. We recommend performing a similar study of beach sands from other important Cuban resorts.

REFERENCES

[1] O. Díaz Rizo, H. Cartas Águila, R. Gutiérrez Manso, S. Reyes Peña, G. Pérez Zayas, *Nucleus* **72**, 48 (2022).

[2] F. F. Ozmen, M. Tavuz, M. R. Tunc, I. Boztosun, *Radiat. Prot. Dosim.* **158**(4), 461 (2013).

[3] United Nations Scientific Committee on the Effects of Atomic Radiation (UNSCEAR), *Sources and Effects of Ionizing Radiation. Report to General Assembly, with Scientific Annexes*, United Nations, New York (2000).

[4] H. Yingnam, L. Xinwei, D. Xiang, F. Tingting, *Mar. Pollut. Bull.* **91**, 357 (2015).

[5] H. Aytekin, M. C. Tufan, C. Küçük, *J. Radioanal. Nucl. Chem.* **303**, 2227 (2015).

[6] P. Kessaratikoon, N. Choosiri, R. Boonkrongcheep, U.Youngchuay, *J. Phys. Conf. Ser.* **1285**, 012013 (2019).

[7] V. Thangam, A. Rajalakshmi, A. Chandrasekaran, B. Arun, S. Viswanathan, B. Venkatraman, S. Bera, *J. Radioanal. Nucl. Chem.* **331**, 1207 (2022).

[8] J. A. Arnedo, A. Tejera, J.G. Rubiano, H. Alonso, J.M. Gil, R. Rodriguez, P. Martel, *Radiat. Prot. Dosim.* **156**(1), 75 (2013).

[9] H.K. Shuaibu, M. U. Khandaker, T. Alrefae, D. A. Bradley, *Mar. Pollut. Bull.* **119**, 423 (2017).

HACIA EL STM: LA HISTORIA TRAS LA PRIMERA IMAGEN DE RESOLUCIÓN ATÓMICA EN CUBA

TOWARDS THE STM: THE STORY BEHIND THE FIRST ATOMIC RESOLUTION IMAGE IN CUBA

M. P. Hernández*[a], J. A. Martínez[a†]

Instituto de Ciencia y Tecnología de Materiales (IMRE), Universidad de La Habana, La Habana, Cuba. javmar@imre.uh.cu†
†para la correspondencia

Recibido 1/5/2025; Aceptado 1/6/2025

* Fallecida el 15 de agosto de 2024 (Rev. Cubana Fis. **41**, 153, 2024).

La microscopía de barrido por efecto túnel constituye una herramienta ampliamente utilizada en las investigaciones de nanociencia y nanotecnología. Esta técnica tiene la ventaja de permitir estudiar las capas superficiales sin dañarlas o destruirlas y de alcanzar la resolución atómica. Su sencillez en comparación con otros instrumentos científicos ha permitido que diferentes laboratorios construyan sus propios microscopios. Se presenta aquí cómo fue construido el STM de la Universidad de La Habana y cómo se alcanzó con él por primera vez en Cuba la resolución atómica.

Scanning tunneling microscopy is a widely used tool in nanoscience and nanotechnology research. This technique has the advantage of allowing the study of surface layers without damaging or destroying them and of achieving atomic resolution. Its simplicity compared to other scientific instruments has allowed different laboratories to build their own microscopes. Here we present how the STM at the University of Havana was built and how it achieved atomic resolution for the first time in Cuba.

Keywords: Laboratory experiments and apparatus (Experimentos y aparatos de laboratorio); History of science (Historia de la ciencia); Scanning tunneling microscopes (Microscopios de barrido de efecto túnel).

I. INTRODUCCIÓN

Una de las herramientas más empleadas por la nanociencia es el microscopio de barrido por efecto túnel (STM, del inglés: scanning tunneling microscope). Este microscopio es un resultado de la aplicación práctica del efecto túnel de la mecánica cuántica en la investigación científica.

El STM permite la obtención de imágenes topográficas de una superficie, la manipulación de átomos y moléculas, y brinda la posibilidad de caracterizar sus propiedades eléctricas locales. Con él podemos obtener información de la densidad electrónica de los orbitales moleculares incluso a nivel de moléculas individuales y estudiar los mecanismos de transporte de carga a través de las moléculas.

El STM ha jugado un papel primordial en el estudio de las monocapas autoensambladas (SAMs, del inglés: self–assembled monolayers) mediante el análisis de la orientación espacial y conformación de las moléculas individuales sobre los sustratos.

Trabajando con el STM a resolución atómica es posible obtener información estructural detallada de las interacciones atómicas en el sistema sustrato–adsorbato, haciendo posible fabricar estructuras más sofisticadas con potenciales aplicaciones en dispositivos electrónicos moleculares como alambres, conmutadores y diodos.

Aquí ofrecemos algunos datos sobre la construccion del primer STM cubano, que permitio obtener las primeras imágenes de resolución atómica en nuestro país.

II. EL MICROSCOPIO DE BARRIDO POR EFECTO TÚNEL

Los antecedentes STM se remontan a noviembre de 1926, cuando Friedrich Hund envió para su publicación un artículo en el cual resolvía la ecuación de Schrödinger para el caso de un electrón que se mueve entre dos pozos de potencial separados por una barrera [1]. Hund encontró que existía una probabilidad de que bajo determinadas condiciones la función de onda del electrón atravesara la barrera y pudiese pasar al pozo vecino [1]. En éste, y una serie de artículos sucesivos publicados en 1927, Hund demostró los casos en que puede producirse este fenómeno y lo aplicó a la interpretación de espectros moleculares [2]. Trabajando independientemente, en un artículo publicado en 1928, Leonid Mandelstam y Mihail Leontovič llegaron a las mismas conclusiones [3]. De este modo fue postulado teóricamente el llamado "efecto túnel", nombre que le fue dado por Walter Schottky en 1931 [4]. Entre 1927 y 1928, Ralph Howard Fowler y Lothar Nordheim, e independientemente Julius Robert Oppenheimer demostraron que la emisión por efecto de campo provocada por un campo eléctrico externo en metales podía ser explicada a través de la aparición de una corriente eléctrica que atravesaba mediante efecto túnel la barrera de potencial de la superficie del material [2, 5–8].

En 1978, los científicos suizos Gerd Binnig y Heinrich Rohrer, del IBM Zurich Research Laboratory, concibieron la idea de utilizar el efecto túnel para realizar estudios topográficos de mapeo de superficies basados en las ideas planteadas por Fowler, Nordheim y Oppenheimer. Con este objetivo, aplicaron pequeños voltajes de polarización entre una muestra conductora y una punta de tungsteno, la cual se encontraba a

fracciones de nanómetro de la superficie de la muestra dentro de una cámara con ultra alto vacío (UHV, del inglés: ultra high vacuum). En esas condiciones, ellos consiguieron provocar la aparición de una corriente por efecto túnel, estable, entre la superficie y la punta. Binnig y Rohrer con la colaboración de Christoph Gerber y Edward Weibel, fabricaron un equipo que trabajaba según este principio. De este modo, en 1981, se construyó el primer STM [9–11], por el cual Binnig y Rohrer recibieron el Premio Nobel de Física en 1986 [12, 13].

Desde los primeros momentos tras su invención, el STM ha sido una importante herramienta extensamente empleada en la caracterización de superficies de materiales, en el estudio de los procesos de adsorción de moléculas y nanopartículas y en la fabricación de dispositivos de electrónica molecular [14–18].

Sin embargo, la manipulación de átomos y moléculas, demostrada en 1990 por Donald M. Eigler y Erhard K. Schweizer [19], es su mayor fortaleza: ningún otro microscopio puede situar átomos y moléculas en posiciones determinadas. Esta capacidad permite fabricar estructuras partiendo de un diseño del material, átomo a átomo o molécula a molécula.

Dada su estructura relativamente sencilla, ha sido factible que diversos grupos científicos construyan sus propios STM, con más o menos originalidad, generando incluso publicaciones científicas relativas a la construcción o automatización de los STM [20, 21]. De hecho, en la literatura científica abundan ejemplos de investigaciones realizadas en los más diversos países, desarrollados o no, utilizando microscopios de barrido por efecto túnel "caseros" [22–30]. El costo de un microscopio comercial había impedido durante años poder disponer de ellos en los laboratorios de nuestro país, de ahí la necesidad e importancia de acometer el trabajo de construir uno por nuestros propios esfuerzos.

III. EL STM DEL IMRE

Las primeras ideas de construir un STM propio se remontan a los finales de los 90 del siglo XX, durante el desarrollo en el entonces Instituto de Materiales y Reactivos (IMRE) de la Universidad de La Habana (UH) –hoy Instituto de Ciencia y Tecnología de Materiales- de una tesis doctoral en la que se emplearon datos publicados de mediciones de electrones balísticos de uniones Schottky metal-semiconductor usando un BEEM (en inglés: Balistic Electron Emission Microscope), para desarrollar un modelo que explicara las heterogeneidades en dichas uniones [9]. El BEEM es un desarrollo del STM, al cual se le agrega otro terminal aparte de los de la muestra y la punta. De este modo, para construir un BEEM primero debía construirse un STM. Entonces, se decidió fomentar una colaboración con laboratorios que tuvieran STM o que hubieran construido su propio microscopio. Esta colaboración permitiría la compra de componentes fundamentales, utilizadas en estos microscopios, como el piezoeléctrico y el motor de pasos. Surgió entonces la posibilidad de establecer un intercambio con un grupo del Centro de Investigación y Estudios Avanzados del Instituto Politécnico Nacional (CINVESTAV-IPN), en Mérida, México; donde el Dr. Andrés Iván Oliva Arias ya había construido un STM [20]. A esta colaboración le faltó financiamiento y no pudo realizarse, pero desde entonces, nos aferramos a la idea de la construcción en Cuba de un STM, por la sencillez de su construcción y de sus potencialidades para el estudio de superficies que nos abría las puertas para las investigaciones en nanoestructuras.

Años después, se estableció una colaboración científica entre nuestro grupo en el IMRE con el Dr. José Valenzuela Benavides, del Centro de Ciencias de la Materia Condensada (CCMC) de la Universidad Nacional Autónoma de México (UNAM) —actualmente Centro de Nanociencias y Nanotecnología (CNyN)—, en Ensenada, Baja California, México, quien ya poseía experiencia en la fabricación de este instrumento. Con el financiamiento por parte de becas doctorales del Centro Latinoamericano de Física (CLAF) y de la Red de Macrouniversidades de América Latina y el Caribe, y proyectos internacionales financiados por la UNAM se pudo finalmente iniciar la construcción de nuestro STM.

Este microscopio de barrido por efecto túnel construido está integrado por las siguientes partes: una mesa antivibratoria, un cabezal que contiene el piezoeléctrico, la punta para el barrido y un circuito preamplificador, una base que soporta la muestra —y que contiene, además, un motor de pasos y los tornillos para el ajuste del cabezal—, una unidad de control de microscopio —que consta de: un circuito de realimentación, amplificador de alto voltaje, controlador de motor de pasos y una fuente—, una computadora, una tarjeta de adquisición de datos y un programa que controla la operación del microscopio.

La construcción del equipo se inició en 2007 en Ensenada. Primero, se fabricaron las piezas que conforman la base y el cabezal, que posteriormente fueron ensamblados. El cabezal consistió en un cilindro de acero donde van colocados el tubo piezoeléctrico y el circuito de preamplificación. La base consistió en un cilindro de aluminio donde está el portamuestras y en cuyo interior está el motor de pasos, que tiene como función acercar la punta a la muestra. (Figura 1). Tres tornillos de rosca fina de fueron insertados al cilindro de aluminio, que soportan el cabezal del STM. Uno de los tornillos acopló con el eje del motor de pasos, y los otros dos quedaron libres, siendo la función de estos dos últimos, realizar la aproximación gruesa de la punta a la muestra. El ajuste fino se realiza por medio del giro del tornillo acoplado al motor, que empuja la parte trasera del cabezal hacia arriba, provocando que su parte delantera aproxime paso a paso la punta a la muestra. Entre los tres tornillos va ubicada la muestra a analizar, sujetada a la base mediante una presilla que, además, hace la función de contacto eléctrico con la muestra. La base dispone de dos conectores, uno para realizar la conexión con el cabezal y el otro hacia la unidad de control. Finalmente, mediante resortes y pernos, fue asegurada la colocación rígida del cabezal sobre la base, como aparece en la Figura 1 y una tapa de aluminio fue incorporada para proteger el sistema del ambiente exterior.

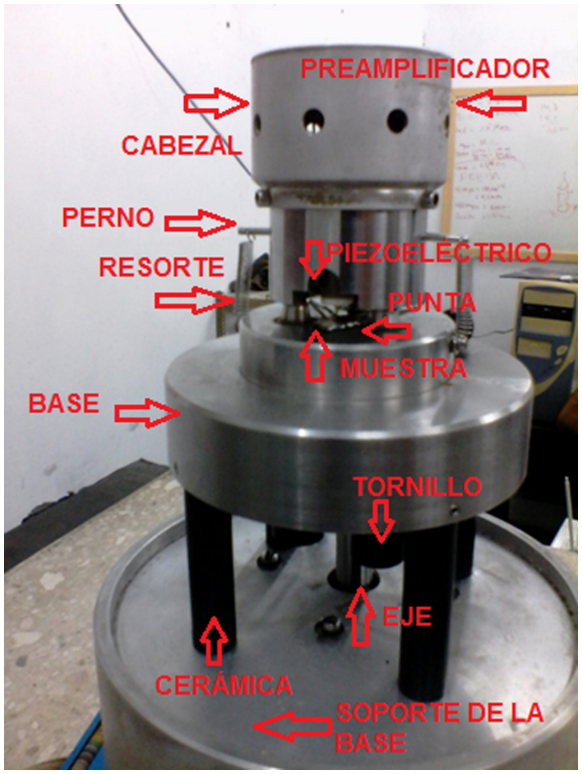

Figura 1. Base y cabezal del STM.

El cilindro piezoeléctrico, diseñado especialmente para su utilización en STM y microscopía de fuerza atómica, está constituido por segmentos denominados +X, –X, +Y, –Y y Z, permiten realizar, mediante la aplicación de señales eléctricas, deformaciones mecánicas en el cabezal en las direcciones X, Y y Z. En el interior del piezoeléctrico, solidaria con este, se colocó una cerámica para sostener una aguja de jeringuilla, que sirvió perfectamente como soporte a la punta del microscopio (Figura 1). Los segmentos +X, –X, +Y, –Y, Z del piezoeléctrico y la aguja de jeringuilla, fueron conectados al circuito electrónico de preamplificación colocado en la parte superior del cabezal. Terminados el cabezal y su base, se conectaron a una unidad comercial de STM disponible en el laboratorio del Dr. Valenzuela en la UNAM y se verificó su funcionamiento con resultados satisfactorios.

El siguiente paso fue la construcción de la unidad de control, un bloque electrónico integrado por un circuito de realimentación, un circuito amplificador de alto voltaje, un controlador de motor de pasos y una fuente. Esta unidad de control también gobierna al motor de pasos a través de un circuito integrado comercial. El circuito de realimentación consiste en un control automático proporcional–integral (PI). Su función es controlar el valor de la corriente de túnel mediante la comparación de la señal adquirida y un valor de referencia fijado por el operador, que es el llamado punto de operación del microscopio. Para la automatización del sistema fue empleada una tarjeta de adquisición de datos comercial. Esta fue configurada para generar las señales de barrido en las direcciones X y Y, que se aplican sobre el piezoeléctrico del cabezal y adquirir la señal provenientes de la unidad de control.

El programa de automatización del STM fue diseñado utilizando LabVIEWTM, entorno de programación gráfico, extensamente empleado en la automatización de experimentos científicos, incluso de STM [21]. El programa de automatización constó de tres bloques fundamentales: uno para la generación de las ondas de barrido, otro en la adquisición de los voltajes de túnel y, finalmente, para el procesamiento de datos y formación de la imagen.

El bloque de generación de ondas del programa utiliza los dos canales de salida analógica de la tarjeta. Estas ondas tienen una forma triangular y, al ser aplicadas a los segmentos X y Y del piezoeléctrico producen un barrido bidimensional de la superficie por la combinación de los movimientos en X y Y. Teniendo en cuenta que el voltaje en la dirección Z del piezoeléctrico es proporcional a la topografía de la superficie, su muestreo permite obtener información para construir la imagen de la superficie. De este modo, la repetición sucesiva del barrido en X y Y permite obtener la imagen de la superficie [31]. Realizados todos estos pasos a lo largo de los años 2007 y 2008 en Ensenada y La Habana, quedaba concluida como tal la construcción del microscopio. Sin embargo, quedaban aún por construir un sistema de aislamiento vibracional, un sistema para fabricar las puntas, así como la conexión a tierra. Y lo más importante, demostrar mediante una imagen, la capacidad del microscopio para obtener resolución atómica.

El aislamiento vibracional es fundamental en este microscopio. Debido a la alta resolución del STM, capaz de ver átomos, las vibraciones mecánicas provenientes de la propia edificación donde se encuentra ubicado, la presencia de fuentes de ruido mecánico, como los pasos de las personas, el movimiento de automóviles, etcétera, afectan notablemente la calidad de las imágenes. Para alcanzar la resolución atómica, es necesaria una resolución lateral de al menos 10 pm, por lo que es necesario reducir las vibraciones externas al menos por debajo de 1 pm [18]. Las vibraciones externas pueden ser minimizadas aislando el instrumento de medición de las vibraciones externas, mediante el empleo de sistemas antivibratorios [32]. Las mesas antivibratorias también son sistemas que se venden comercialmente, pero que con cierto grado de creatividad pueden ser sustituidas convenientemente por sistemas “caseros”.

Una mesa antivibratoria consiste en un sistema mecánico que idealmente tiene el comportamiento de un oscilador armónico críticamente amortiguado [32]. En este oscilador, las vibraciones que actúan sobre él son absorbidas y el sistema es restablecido en su posición original en un mínimo de tiempo. De este modo, un STM colocado en una mesa antivibratoria permanece aislado de las vibraciones propias de la edificación donde está instalado, que pueden variar considerablemente en amplitud y frecuencia según el tipo de construcción, piso y lugar de emplazamiento [34]. De este modo, el diseño de estos sistemas puede ser muy variado. La construcción resultante es una combinación de materiales rígidos de gran masa, como granito y acero, para eliminar los efectos de las altas frecuencias; materiales elásticos, como gomas y colchones de aire, para eliminar las bajas frecuencias; hasta obtener el adecuado amortiguamiento.

La mesa antivibratoria construida en el IMRE para el STM fue aislada del suelo mediante piezas de goma. Sobre estas fue colocado un cajón de madera relleno con arena e, inmerso en ella, la base de un soporte metálico de gran masa. Sobre este soporte se colocaron alternativamente piezas de goma y de granito, además de un neumático inflado, a modo de colchón de aire (Figura 2).

Figura 2. Mesa antivibratoria con el STM.

Al no contar con un medidor comercial de vibraciones, el funcionamiento de la mesa antivibratoria se evaluó de la siguiente forma: Sobre la superficie superior de la mesa antivibratoria se instaló un interferómetro de Michelson [34] observando la aparición de franjas de interferencia en ausencia de vibraciones mecánicas externas, así como el inmediato restablecimiento de estas, décimas de segundo después de realizar perturbaciones mecánicas en el local. La observación de las franjas de interferencia en ausencia de vibraciones forzadas en el local, así como el rápido restablecimiento del patrón de interferencia con posterioridad a la realización de estas, fueron los indicadores para considerar la existencia de un buen aislamiento vibracional.

La resolución lateral del STM está determinada por el ancho e intensidad del filamento de corriente túnel, por el potencial aplicado, por las propiedades físicas de la punta y la muestra, y por los estados electrónicos de la superficie y la punta [36].

De este modo, disponer de puntas de calidad es imprescindible para lograr buenas imágenes con resolución atómica.

Una punta debe de cumplir los siguientes requisitos: longitud corta, simetría cónica o hiperbólica, ápice afilado y ser fabricada de un metal relativamente inerte. Los métodos electroquímicos son fáciles y rápidos para obtener puntas baratas y confiables para STM [37–39]. De este modo, para la fabricación de las puntas empleamos el método electroquímico de corriente alterna [37]. En este método, un alambre de tungsteno de 0.25 mm de diámetro es sumergido en un electrólito a una profundidad entre 0.4 y 1 mm. El electrólito empleado fue una solución de hidróxido de sodio de concentración 2-6 mM. Como contraelectrodo empleamos un aro de cobre colocado sobre la superficie del electrólito. Para esto fue construido un equipo [39] basado en el diseño de J. P. Ibe y colaboradores [40], que permitió la fabricación de las puntas, mediante la aplicación de un voltaje hasta que, por la acción de la reacción electroquímica, el tungsteno forma la punta de geometría cónica (Figura 3).

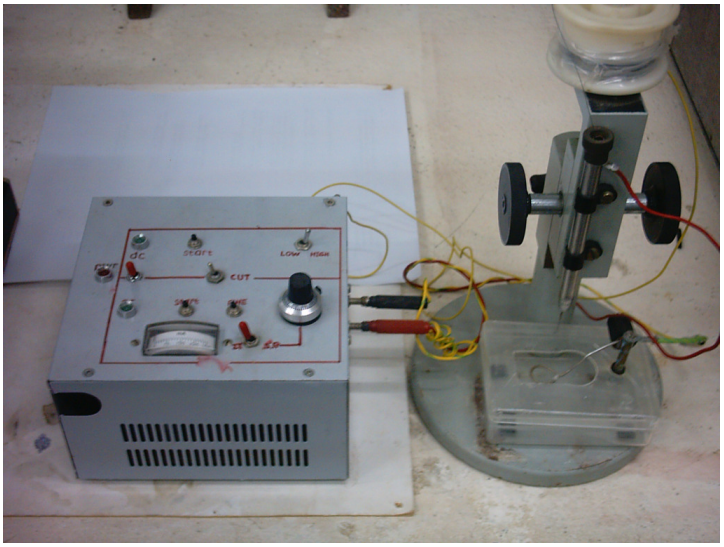

Figura 3. Equipo para la fabricación de puntas.

Sin embargo, a pesar de ya tener el STM, el sistema antivibracional y la fabricación de puntas listas, no fue de inmediato que alcanzamos la resolución atómica, debido a que el ruido eléctrico en las imágenes impedía ver los átomos. Durante un tiempo, fuimos asegurándonos que cada una de las partes que componían el microscopio funcionaban bien. Fue un ejercicio en el creamos circuitos de prueba, mediciones de señales de corriente y voltaje en el tiempo en todos los circuitos del STM. Un reacomodo de todas las tierras resolvió el ruido en las imágenes, para lo cual fue necesario modificaciones en la instalación.

Finalmente, el 24 de febrero de 2009 fue la fecha en que se logró adquirir por primera vez una imagen con resolución atómica en Cuba, correspondiente a una superficie de grafito (Figura 4). Para lograr la resolución atómica se realizó una calibración preliminar basada en la medición de tamaños de granos de oro, y pistas de disco compacto, previamente observadas con un microscopio electrónico de barrido (SEM, del inglés: scanning electron microscope) y luego se realizaron sucesivos barridos de la muestra disminuyendo su amplitud y seleccionando la frecuencia de barrido adecuada, hasta que fue posible visualizar los átomos.

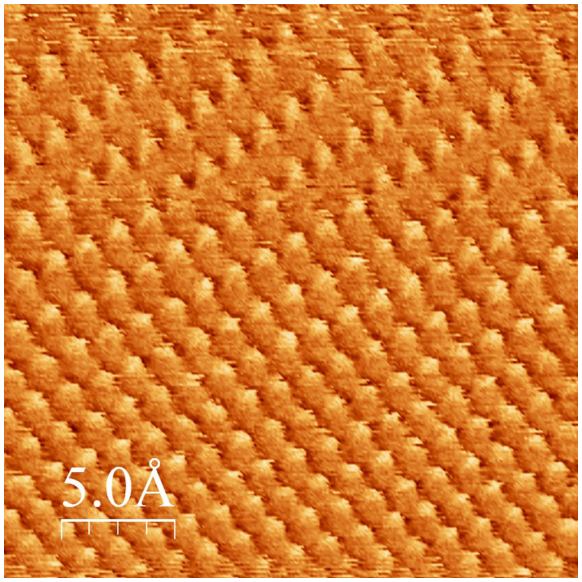

Figura 4. La primera imagen de resolución atómica adquirida en Cuba, átomos de grafito. IMRE, Universidad de La Habana, 24 de febrero de 2009.

El siguiente paso, consistió en la calibración del cabezal del microscopio en las direcciones X y Y, a partir de las imágenes de resolución atómica, que proporcionaban las distancias entre los átomos de grafito.

En imágenes de resolución atómica realizadas sobre áreas de diferente tamaño, aplicando diferentes voltajes al piezoeléctrico en la dirección X e Y, realizamos el conteo de la cantidad de átomos presentes a lo largo de un perfil trazado sobre la imagen, y podemos establecer la magnificación para cada voltaje.

En el caso de la calibración del eje Z, el procedimiento fue el siguiente. Conociendo el valor de la altura de los escalones monoatómicos del grafito, la medición de los voltajes en Z en escalones monoatómicos permitió realizar la calibración.

Este proceso, descrito en pocos párrafos, no estuvo exento de dificultades, errores e imprevistos. Un caso curioso fue en una ocasión la afectación que sobre el STM estuvo realizando durante algunos meses un aire acondicionado defectuoso, que incrementaba desmesuradamente la humedad del local donde se encontraba el equipo, lo que se manifestó en un incremento del ruido eléctrico en el cabezal del STM. Varias semanas tomó identificar el origen de esta fuente de ruido, que fue eliminada después de reparar el aire. Originalmente, la mesa antivibratoria fue construida en un local muy pequeño, por lo que su funcionamiento no fue eficiente. No fueron pocas las dificultades ya explicadas para garantizar la calidad de la conexión a tierra. A todo esto, podrían agregarse las conocidas dificultades con las interrupciones del servicio eléctrico.

Desde que se logró la primera imagen de resolución atómica, el equipo ha sido empleado en la investigación científica y las imágenes adquiridas con él han sido publicadas en diversas revistas científicas [41–52].

En el propio año 2009 nuestro laboratorio en el IMRE recibió la visita del Dr. Chistoph Gerber, uno de los creadores del STM en 1981. Durante su visita elogió la originalidad y calidad de las soluciones propuestas para superar las dificultades y poder poner en funcionamiento el STM y realizó valiosas sugerencias para su mejoramiento (Figura 4).

Figura 5. Visita del Dr. Christoph Gerber al STM del IMRE, noviembre de 2009.

Los comentarios elogiosos del Dr. Gerber fueron de gran estímulo para nosotros, quienes continuamos empeñados en ver, a través de un pequeño túnel, los más pequeños detalles de los materiales en la nanoescala.

IV. CONCLUSION

La obtención de la primera imagen de resolución atómica en Cuba fue el resultado del empeño de un grupo de investigación del IMRE, que en colaboración con un grupo mexicano pudo acometer la labor de construir un STM y ponerlo en funcionamiento. Este resultado demuestra que es posible, en las condiciones de nuestro país construir equipamiento científico de avanzada y lograr con él resultados de impacto.

V. ACKNOWLEDGEMENT

La construcción del STM en Cuba fue el resultado del trabajo de un equipo dirigido por Mayra Paulina Hernández Sánchez, en Cuba y José Valenzuela Benavides en México, e integrado por: Javier Alberto Martínez Pons, Carlos Alberto Canino Ramos, Antón Mesa, y José Orlando Abad Hernández. Otras personas a quienes agradecemos su colaboración para que el microscopio se hiciera realidad son: Yohan Pérez Moret, Manuel Herrera Zaldívar, Carlos Alonso Villasuso, Luis Ponce Cabrera, José Alfredo Herrera Isidrón, Edwin Pedrero González y Ernesto Estévez Rams.

REFERENCIAS

[1] F. Hund, Z. Phys. **40**, 742 (1927).
[2] E. Merzbacher, Phys. Today **55**, 44 (2002).
[3] L. Mandelstam y M. Leontowitsch, Z. Phys. **47**, 131 (1928).
[4] W. Schottky, Phys. Z. **32**, 833 (1931).
[5] L. Nordheim, Z. Phys. **46**, 833 (1927).

[6] J. R. Oppenheimer, Phys. Rev. **31**, 66 (1928).
[7] J. R. Oppenheimer, Proc. Natl. Acad. Sci. USA **14**, 363 (1928).
[8] R. H. Fowler y L. Nordheim, Proc. Roy. Soc. London A **119**, 173 (1928).
[9] G. Binnig y H. Rohrer, Helv. Phys. Acta **55**, 726 (1982).
[10] G. Binnig, H. Rohrer, Ch. Gerber y E. Weibel, Appl. Phys. Lett. **40**, 178 (1982).
[11] G. Binnig [sic.], H. Rohrer, Ch. Gerber y E. Weibel, Phys. Rev. Lett. **49**, 57 (1982).
[12] G. Binnig y H. Rohrer, Rev. Mod. Phys. **59**, 615 (1987).
[13] G. Binnig y H. Rohrer, Angew. Chem. Int. Ed. Engl. **26**, 606 (1987).
[14] R. Wiesendanger, *Scanning Probe Microscopy and Spectroscopy. Methods and Applications* (Cambridge University Press, Cambridge, 1994), pp. 291–580.
[15] Ch. Bai, *Scanning Tunneling Microscopy and its Applications*, 2nd ed. (Shanghai Scientific and Technical Publishers/Springer, Shanghai/Berlin, 1995), pp. 165–344.
[16] K. Oura, V. G. Lifshitz, A. A. Saranin, A. V. Zotov y M. Katayama, *Surface Science. An Introduction* (Springer, Berlin, 2003), pp. 159–164.
[17] S. Chiang, J. Phys. D Appl. Phys. **44**, 464001 (2011).
[18] C. J. Chen, *Introduction to Scanning Tunneling Microscopy*, 3rd ed. (Oxford University Press, Oxford, 2021), pp. 167–272.
[19] D. M. Eigler y E. K. Schweizer, Nature **344**, 524 (1990).
[20] A. I. Oliva, V. Rejón, N. López Salazar, E. Ávila, T. Kantún, J. E. Corona y J. L. Peña, Rev. Mex. Fís. **40**, 106 (1994).
[21] J. Guillén Rodríguez, E. Valaguez-Velázquez, A. Zapata-Navarro, A. Márquez-Herrera, M. Meléndez-Lira y M. Zapata-Torres, Rev. Mex. Fís. **59**, 208 (2013).
[22] I. Biljan, M. Kralj, T. Mišić Radić, V. Svetličić y H. Vančik, J. Phys. Chem. C **115**, 20267 (2011).
[23] A. Crepaldi, S. Pons, E. Frantzeskakis, F. Calleja, M. Etzkorn, A. P. Seitsonen, K. Kern, H. Brune y M. Grioni, Phys. Rev. B **87**, 115138 (2013).
[24] N. V. Fischer, U. Mitra, K.–G. Warnick, V. Dremov, M. Stocker, W. Hieringer, F. W. Heinemann, N. Burzlaff, A. Görling y P. Müller, Chem. Eur. J. **20**, 11863 (2014).
[25] F. Lecadre, F. Maroun, I. Braems, F. Berthier, C. Goyhenex y P. Allongue, Surf. Sci. **607**, 25 (2013).
[26] R. Hammer, A. Sander, S. Förster, M. Kiel, K. Meinel y W. Widdra, Phys. Rev. B **90**, 035446 (2014).
[27] D. Y. Lee, M. M. Jobbins, A. R. Gans y S. A. Kandel, Phys. Chem. Chem. Phys. **15**, 18844 (2015).
[28] H. Li, H.–X. Fu y S. Meng, Chin. Phys. B **24**, 086102 (2015).
[29] A. Martín–Recio, C. Romero–Muñiz, A. J. Martínez–Galera, P. Pou, R. Pérez y J. M. Gómez–Rodríguez, Nanoscale **7**, 11300 (2015).
[30] J. Wang, W. Ge, Y. Hou y Q. Lu, Carbon **84**, 74 (2015).
[31] J. A. Martínez, J. Valenzuela, M. P. Hernández y J. Herrera, Rev. Mex. Fís. **62**, 45 (2016).
[32] M. A. Talley, en *Harris' Shock and Vibration Handbook*, 6ª ed., editado por A. G. Piersol y T. L. Páez (McGraw–Hill, New York, 2010), pp. 38.1–38.39.
[33] K. R. Symon, *Mecánica* (Aguilar, Madrid, 1968), pp. 52–55.
[34] M. Okano, K. Kajimura, S. Wakiyama, F. Sakai, W. Mizutani y M. Ono, J. Vac. Sci. Technol. A **5**, 3313 (1987).
[35] E. Hecht, *Óptica*, 3ª ed. (Addison–Wesley, Madrid, 2000), pp. 407–411.
[36] A. N. Chaika, S. S. Nazin, V. N. Semenov, S. I. Bozhko, O. Lübben, S. A. Krasnikov, K. Radican e I. V. Shvets, Eur. Phys. Lett. **92**, 46003 (2010).
[37] Y. Khan, H. Al–Falih, Y. Zhang, T. K. Ng y B. S. Ooi, Rev. Sci. Instrum. **83**, 063708 (2012).
[38] T. Nishimura, A. M. A. Hassan y M. Tomitori, Appl. Surf. Sci. **284**, 715 (2013).
[39] A. Reyes Valenzuela, *Diseño de un controlador electrónico para la fabricación de puntas metálicas para un microscopio de efecto túnel* (Tesis de Ingeniería, Universidad Autónoma de Baja California, Ensenada, BC, 2003).
[40] J. P. Ibe, P. P. Bey, S. L. Brandow, R. A. Brizzolara, N. A. Burnham, D. P. Di Lella, K. P. Lee, C. R. K. Marrian y R. J. Colton, J. Vac. Sci. Technol. A **8**, 3570 (1990).
[41] J. A. Martínez, J. Valenzuela B., R. Cao Milán, J. Herrera, M. H. Farías y M. P. Hernández, Appl. Surf Sci. **320**, 287 (2014).
[42] J. A. Martínez, J. Valenzuela, C. E. Hernández-Tamargo, R. Cao-Milán, J. A. Herrera, J. A. Díaz, M. H. Farías, H. Mikosch y M. P. Hernández, Appl. Surf Sci. **345**, 394 (2015).
[43] F. Solís-Pomar, O. Nápoles, O. Vázquez Robaina, C. Gutiérrez-Lazos, A. Fundora, A. Colin, E. Pérez-Tijerina y M. F. Meléndrez, Ceram. Int. **42**, 7571 (2016).
[44] R. Barzaga Guzmán, *Estudio computacional de la formación de multicapas de azufre en la superficie Au(100)* (Tesis de Maestría, Universidad de La Habana, La Habana, 2016).
[45] M. P. Hernández, J. A. Martínez, C. E. Hernández-Tamargo, R. Barzaga, J. A. Herrera, M. H. Farías, J. Valenzuela y H. Mikosch, Anales de la Academia de Ciencias de Cuba **7**, 1 (2017).
[46] G. Navarro-Marín, M. P. Hernández, O. Estévez-Hernández, M. H. Farías Sánchez y D. Díaz-Domínguez, Acta Microscopica **26A**, 430 (2017).
[47] R. Barzaga, H. Mikosch, J. A. Martínez y M. P. Hernández, Acta Microscopica **26A**, 436 (2017).
[48] J. A. Martínez Pons, *Caracterización de superficies de oro modificadas con moléculas sulfuradas mediante microscopía de barrido por efecto túnel* (Tesis de Doctorado, Universidad de La Habana, La Habana, 2017).
[49] G. Navarro Marín, *Estudio de la adsorción de derivados de tiourea sobre Au(111)* (Tesis de Maestría, Universidad de La Habana, La Habana, 2018).
[50] R. Barzaga, J. A. Martínez, M. H. Farías y M. P. Hernández, J. Phys. Chem C **123**, 12183 (2019).
[51] R. Barzaga Guzmán, *Computational study of the adsorption of molecules on metal surfaces* (Tesis de Doctorado, Universidad Autónoma de Madrid, Madrid, 2021).

[52] M. P. Hernández Sánchez, R. Barzaga Guzmán, J. A. Martínez Pons, G. Navarro Marín, S. Díaz-Tendero Victoria, O. L. Estévez Hernández, J. A. Herrera Isidrón, M. H. Farías Sánchez y O. Cruzata Montero, Anales de la Academia de Ciencias de Cuba **14**, 1607 (2024).

CONMEMORANDO LA HISTORIA DE LA FÍSICA EN CUBA.

El 2 de abril de 2025 se develó en la facultad de Física de la Universidad de La Habana una placa conmemorativa para inaugurar el aula de postgrado "Dra. Elena Vigil Santos", como homenaje a quien fuera una de las personalidades más importantes en nuestra Física. Su larga trayectoria como impulsora del campo de los materiales semiconductores en Cuba, y su sostenida labor docente –especialmente dentro de las asignaturas asociadas a la Física del Estado Sólido— han dejado un sólido legado dentro de nuestra disciplina. Más temprano dentro de la misma jornada, se había organizado en la Facultad de Física una sesión de debate dirigida a los estudiantes, donde la Dra. María Sánchez-Colina realizó una documentada presentación sobre la Historia de la Física en Cuba profusamente ilustrada, y salpicada con notables pinceladas de humor.A todas estas actividades, además de los jóvenes, se contó con la presencia de profesores de todas las edades –incluyendo a una figura tan legendaria dentro de la docencia cubana como el profesor Medel Pérez-Quintana.

Recordando a Elena. Momento en que se devela la placa que da el nombre de Elena Vigil-Santos a un aula de la Facultad de Física de la Universidad de La Habana, el 2 de abril de 2025. (Foto: E. Altshuler).

Dr. Ernesto Altshuler
Facultad de Física, Universidad de La Habana

EL REGRESO DEL COSMONAUTA.

Del 5 al 6 de junio de 2025, la Facultad de Física de la Universidad de La Habana celebró su XL Jornada Científica Estudiantil, dedicada al 45° aniversario del vuelo espacial conjunto Cuba-URSS (Programa Intercosmos) y a los científicos cubanos involucrados. En la conferencia inaugural, realizada en el anfiteatro *Manuel F. Gran Guilledo* de la Facultad de Física. Participaron el Gen. Brig. Arnaldo Tamayo Méndez (tripulante de la misión Soyuz 38), el Dr. José Altshuler (exdirector del programa) y el Dr. Julio Vidal Larramendi, físico que contribuyó a uno de los experimentos llevados a cabo durante el vuelo. El evento destacó la contribución cubana a la exploración espacial. En el cierre, se llevó a cabo una sesión de preguntas e intercambio con estudiantes y profesores. Durante este intercambio, el profesor Vidal compartió su experiencia dentro del "Experimento Caribe" vinculada al desarrollo del experimento de purificación de germanio en condiciones de mircogravidez, el Dr. Altshuler compartió con los asistentes sus vivencias relacionadas con el proceso previo al vuelo y presentó material gráfico, como libros y revistas de la época, que mostraban las imágenes que dieron la vuelta al mundo en 1980 y el General Tamayo relató el exigente proceso de selección, así como la preparación física que implicaba el viaje, e incluyó detalles sobre algunos de los experimentos realizados a bordo de la nave Soyuz 38. El encuentro no solo celebró este importante aniversario, sino que también destacó el significativo aporte de la comunidad científica cubana en este capítulo de la historia espacial.


El regreso a la facultad de Física. Al centro, el cosmonauta Arnaldo Tamayo-Méndez (con la camisa azul). A su izquierda y derecha, los profesores José Altshuler y Julio Vidal, respectivamente. En la foto se incluyen varios estudiantes de tercer año de licenciatura en Física (Foto: E. Altshuler).

Dra. Yuslín González
Facultad de Física, Universidad de La Habana

LAUROS CUBANOS EN LA OLIMPIADA MESO-AMERICANA DE FÍSICA.

El pasado 16 de junio de 2025 se celebró la 8va Olimpiada Mesoamericana de Física. Participaron en total 60 estudiantes de 8 países. Cuba aportó 4, que han estado entrenándose en la Facultad de Física de la Universidad de La Habana desde el 3 de marzo de 2025, y que participaron vía online desde esa institución. Se obtuvieron magníficos resultados: Cuba se llevó un ORO por intermedio de Sergio D. Santiesteban-Sarmiento y un BRONCE a manos de Rosmary Fernández-Tamayo, además de una mención.

Los cuatro participantes cubanos en acción, mientras participaban (modalidad online) en la 8va Olimpíada Mesoamericana de Física, celebrada el 16 de junio de 2025 (Foto: S. Larramendi)

Dr. Saúl Larramendi
Facultad de Física, Universidad de La Habana

Revista Cubana de Física
ISSN 0253-9268
Online ISSN 2224-7939